Analysis of Three-Dimensional Dynamic Stall

Antonella Ferrecchia

A dissertation submitted for the degree of doctor of Philosophy

Department of Aerospace Engineering

University of Glasgow

September 2002

Abstract

For many years the physical process that triggers the onset of the dynamic stall vortex and the mechanisms responsible for the growth and convection of the vortex have been of interest to many researchers who have attempted to understand these events through experimental tests and numerical computations. Despite the intense interest in the phenomenon, there is still an incomplete understanding of the physics of the dynamic stall process. The work presented in this thesis takes place in this context and attempts to provide a deeper understanding of the physical phenomena associated with the dynamic stall process on finite wing planforms.

After reviewing dynamic stall from a historical perspective, the methodology adopted in the present study is outlined. In particular, the work involves the analysis of data from the Glasgow University unsteady aerodynamics database that has been built up over a number of years through contributions from a range of researchers. Before presenting the analysis, the experimental methods and the test models used to collect the data are described for completeness. Analysis then focuses on two finite wing models; one a rectangular wing of aspect ratio three and the other with the same overall dimensions but with 60^0 swept tips. However, as most research to date has focussed on nominally two-dimensional data, the results are referenced to measurements made on a nominally two-dimensional NACA 0015 aerofoil model. This is appropriate as this aerofoil was used as the wing section of both of the three-

dimensional wing models. Flow visualisation images collected in a previous study also provide valuable information to supplement the pressure analysis.

The analysis highlights many interesting features of the three-dimensional response. In particular, it is shown that, although the flow at the mid span sections of the finite wings exhibit many of the features of the two-dimensional case, there are some significant differences. In particular, the three-dimensional flow is dominated by the downwash from the wing tips. This causes the normal force response during pitching to lag the static normal force curve. This is in complete contrast to the two-dimensional case where the shed vorticity induces the opposite effect. The downwash also influences the incidence of lift stall but it does so in a manner that is dependent on the reduced pitch rate. Despite these effects, it is established that the flow behaviour in the mid-span region is almost two-dimensional prior to vortex inception. This provides an opportunity to examine the relationship between the generation of vorticity, or vorticity flux, in the leading edge region and the origins of the dynamic stall vortex at specific span locations in isolation.

The concept of vorticity flux is then introduced and the restrictions of the two-dimensional assumption discussed. The vorticity flux distributions around the leading edges of the nominally two-dimensional NACA 0015 aerofoil and the two finite wings are then examined for pitching cases. On this basis a link is established between the peak vorticity flux and the dynamic stall vortex formation. This is confirmed by comparison of the vorticity flux measurements with a previous dynamic stall vortex detection method. The two methods are shown to give almost identical results in situations where the flow may be considered nominally two-dimensional. This suggests that monitoring vorticity flux may provide a practical method of dynamic stall vortex detection.

In regions of the finite wings that exhibit strong three-dimensional flow effects, i.e. away from the mid-span, the peak vorticity flux is achieved after the dynamic stall vortex forms. This suggests that vortex formation is triggered by interference from adjacent sections of the wing. To examine this possibility, the vorticity flux is compared to a criterion used to detect the initial instability of the boundary layer at the leading edge. It is shown that the relationship between this criterion and the peak vorticity flux is the same along the span of the wing. This is a significant result as it demonstrates that, although the leading edge response determines the incidence of vortex onset near the mid-span, the formation of the vortex on sections of the wing closer to the tips occurs before the leading edge becomes critical. The implications of this for dynamic stall modelling on three-dimensional wings are significant because methods that involve the coupling of two-dimensional dynamic stall predictors with lifting line formulations will not capture this effect.

Finally, the convection of the vortex over both the aerofoil and finite wings is studied. It is shown that all sections of the finite wings exhibit significant differences from the two-dimensional case. These are explained by consideration of the complex three-dimensional evolution of the vortex structures above the finite wings during the stall process.

Preface

The work reported in this thesis was conducted at the Department of Aerospace Engineering in Glasgow University between October 1997 and December 2000.
All aspects of the work presented herein are original in concept except where otherwise indicated.
No part of this dissertation has been submitted to any other academic establishment.

Antonella Ferrecchia

September 2002

Acknowledgements

I would like to recognize the collaboration of Dr. Coton who offered me valuable guidance during the course of this research. I am grateful to him for all the time and energy he gave in reading this manuscript, making detailed correction and suggestion for improvements. I thank Prof. Galbraith for his constructive comments.

I would like also to record thanks to my flatmates and friends, Marcos, Sabrina, Miguel, Nik who gave me unforgettable moments during the project. To Nial who was kind and patient tolerating me during the rewriting of the manuscript and encouraged me when I was close to abandon. To Silvana whose panting words during ours long runs gave me the strength to complete this work.

It is right that the ultimate acknowledgement be to my parents for their unending love and support.

Finally, my thanks is given to DERA (Defence Evaluation and Research Agency) for awarding me a scholarship to make this research possible.

To all, my warmest thanks

Alla mia dolcissima sorellina

Marisa

Perché gli
aerei cadono?
Ma perché
non dovrebbero?
Su e giú come somari
tra cirri, nembocumuli
e aerei militari
bombardati da missili
imbottiti di plastico
nelle bufere atterrano
vuotano i portacenere
i sacchetti del vomito
e subito ripartono
mentre hostess stupende
rimpinzano di merende
il carrello non scende
il radar non risponde
il check-in non funziona
coi piloti stressati
i sedili firmati
e i motori scassati
gli utili assicurati
li si sente gridare
su nelle stratosfere:
"ci siam rotti le scatole
nere".

Stefano Benni

Contents

Abstract iii

Preface vii

Acknowledgements ix

Contents xiii

List of Tables xvii

List of Figures xix

Nomenclature xxv

1 Introduction 1

1.1 The Concept of Dynamic Stall 1

1.2 A Short History of Stall 4

1.2.1 Experimental Investigations 4

1.2.2 Reconstruction and Prediction of the Stall Process 10

1.3 Objective and Approach of Current Work 12

2 Description of Test Facility 15

2.1 Introduction 15

2.2 Wind Tunnel Tests 16

2.2.1 Two-Dimensional Pitch Drive Mechanism 16
2.2.2 Three-Dimensional Pitch Drive Mechanism 17
2.3 Test Models and Procedure 20
2.3.1 NACA 0015 Aerofoil 20
2.3.2 Rectangular Wing Planform 21
2.3.3 60^0 Swept-Tip Wing Planform 22
2.4 Ramp-up Experiments 25

3 Flow Field around a Pitching Rectangular Wing Planform 29
3.1 Introduction 29
3.2 Description of Flow Behaviour 30
3.3 Two-Dimensional Assumption 34

4 Dynamic Stall Behaviour on the Rectangular Wing Planform 39
4.1 Introduction 39
4.2 Pressure Distribution Analysis 40
4.3 Normal Force Analysis 48

5 Dynamic Stall Behaviour on the 60^0 Swept-Tip Wing Planform 57
5.1 Unsteady Flow over the 60^0 Swept-Tip Wing 57

6 Vorticity and Its Development 65
6.1 Introduction 65
6.2 Vorticity 67
6.2.1 Generation and Spreading of Vorticity 67
6.2.2 Production of Vorticity at Wall 72
6.2.3 Flow Instability and Vortex Formation 75
6.2.4 Vortex Growth and Separation 76
6.3 Vorticity Flux Analysis 79

7 Detection of Dynamic Stall Vortex Inception **87**

7.1 Introduction 87

7.2 Cp-Deviation and Vorticity Flux 89

7.2.1 Cp-Deviation Method 89

7.2.2 Vorticity Flux and Dynamic Stall Onset 92

7.2.3 Cp-Deviation and Vorticity Flux Peak S^+ 94

7.3 Alternative Technique 97

7.3.1 'Evans & Mort' and Cp-Deviation Methods 100

7.4 Discussion on Three-Dimensional Effects 104

8 Vortex Convection **109**

8.1 Vortex Convection 111

8.2 Convection Speed 116

8.3 Discussion of Vortex Convection 121

9 Conclusions and Final Remarks **123**

Appendices **126**

A Ramp-Up Test List and Transducers Coordinates **127**

B Flow Visualization Set Images, Rectangular Wing **137**

C Equations of Motion **147**

C.1 Navier-Stokes Equation 147

C.2 Vorticity Equation 148

D Flow Visualization Set Images, 60^0 Swept-Tip Wing **151**

Bibliography **154**

List of Tables

2.1 Characteristics of the test cases analyzed in this work. 25

2.2 List of ramp-up tests, NACA 0015 aerofoil. 26

2.3 List of ramp-up tests, rectangular wing. 27

2.4 List of ramp-up tests, swept tips wing. 27

3.1 Characteristics of three-dimensional flow visualization experiments, rectangular wing. 30

3.2 Characteristics of nominally two-dimensional flow visualization experiments, NACA 0015 aerofoil. 35

5.1 Characteristics of the rectangular wing with 60^0 swept tips test case relative to the three-dimensional flow visualization experiments. . . . 57

A.1 Complete list of ramp-up tests. Mach number around 0.12 and 0.16 correspond to two- and three-dimensional tests. 128

A.2 Coordinates of the transducers along the chord, NACA 0015 aerofoil . 129

A.3 Coordinates of the transducers at 57%, 68%, 80% of the span on the rectangular wing. The x coordinate along the chord and y coordinate perpendicular to the chord are the same at all span-wise sections. . . 130

A.4 Coordinates of the transducers at 57%, 68%, 80% on the span of the rectangular wing. The x coordinate along the chord and y coordinate perpendicular to the chord are the same at all span-wise sections. . . 131

A.5 Coordinates of the transducers in the region of the wing tip of the rectangular wing. 132
A.6 Coordinates of the transducers at 57%, 68%, 80% on the span of the swept-tip wing. The x coordinate along the chord and y coordinate perpendicular to the chord are the same at all span-wise sections. . . 133
A.7 Coordinates of the transducers in the region of the tip of the swept tip wing, (1^{st} part). 134
A.8 Coordinates of the transducers in the region of the tip of the swept tip wing, (2^{nd} part). 135
A.9 Coordinates of the transducers in the region of the tip of the swept tip wing, (3^{th} part). 136

List of Figures

2.1 Schematic of wind tunnel test set up; two-dimensional tests. (From Galbraith et al. [39]). 18

2.2 Schematic of wind tunnel test set up; three-dimensional tests. (From Jiang et al. [62]). 19

2.3 NACA 0015 aerofoil model. 20

2.4 Test model of the rectangular wing with simple solid of revolution at its tip. (Adapted from Jiang et al. [60]). 22

2.5 Test model of the rectangular wing with 60^0 swept tips. (Adapted from Jiang et al. [62]). 23

3.1 Vortex system on Rectangular Wing 32

3.2 Images of the dynamic stall vortex on a NACA 0015 aerofoil and at the mid-span of a rectangular wing with NACA 0015 cross-sectional profile. (From Laghezza [66]) 36

4.1 Time history of unsteady Cp chordal distribution over nominally two-dimensional NACA 0015 aerofoil at reduced pitch rate 0.022. 42

4.2 Time history of unsteady Cp chordal distribution at 57% of span of the rectangular wing at reduced pitch rate 0.022. 44

4.3 Time history of unsteady Cp chordal distribution at 68% of span of the rectangular wing at reduced pitch rate 0.022. 45

4.4 Time history of unsteady Cp chordal distribution at 80% of span of the rectangular wing at reduced pitch rate 0.022. 46

4.5 Time history of unsteady Cp chordal distribution at 90% of span of the rectangular wing at reduced pitch rate 0.022. 47

4.6 Build-up of normal force coefficient versus incidence during the events of dynamic stall. (Adapted from Carr et al. [10]). 49

4.7 Normal force coefficients versus incidence in the quasi-steady domain at reduced pitch rate 0.003. 52

4.8 Normal force coefficients versus pitch incidences of the nominally two-dimensional NACA 0015 aerofoil and three cross-span sections of the rectangular wing with rounded tips for several reduced pitch rates. . . 55

5.1 Vortex structure on Rectangular Wing and Swept-Tips Wing 59

5.2 Normal force coefficient versus incidence for the nominally two-dimensional NACA 0015 aerofoil, the rectangular and the 60^0 swept-tip wings at reduced pitch rate 0.010. 60

5.3 Normal force coefficient versus incidence for the rectangular and the 60^0 swept-tip wings for a number of reduced pitch rates. 62

5.4 Normal force coeffcient versus pitch-incidence for the nominally two-dimensional NACA 0015 aerofoil, the rectangular and the 60^0 swept-tip wings at reduced pitch rate 0.026. 63

6.1 Angular momentum in the x plane of a spherical particle of fluid. (Adapted from Lighthill [76]). 68

6.2 Streamlines and equivorticity lines around a sphere at three Reynolds number. (Adapted from Jenson [59]). 71

6.3 Vortex lines roll-up because of the instability of the flow. (Adapted from Rosenhead [113]). 76

6.4 Rankine vortex: velocity and pressure distributions. 78

6.5 Vorticity flux over the nominally two-dimensional NACA 0015 aerofoil versus surface coordinate and incidence during ramp-up test at reduced pitch rate 0.027. 81

6.6 Vorticity flux over the nominally two-dimensional NACA 0015 aerofoil versus surface coordinate at selected incidence during ramp-up test at reduced pitch rate 0.027 83

6.7 Vorticity flux over 57% of span of the rectangular wing versus surface coordinate and incidence at reduced pitch rate 0.027. 85

6.8 Vorticity flux over six span locations on the rectangular wing at incidence $alpha = 21^0$ at reduced pitch rate 0.027. 86

7.1 Cp-deviation method for the prediction of dynamic stall vortex onset. The data are relative to the nominally two-dimensional NACA 0015 aerofoil at reduced pitch rate 0.0217. 91

7.2 Peaks S^- and S^+ of vorticity flux at inboard sections of the rectangular wing and nominally two-dimensional NACA 0015 aerofoil at several reduced pitch rates. 93

7.3 Cp-deviation and vorticity flux peak S^+ for several reduced pitch rates. 95

7.4 Correlation between normal lift coefficient and pitch incidence corresponding to the minimum peak value S^+. The data are relative to the nominally two-dimensional NACA 0015 aerofoil for two reduced pitch rates. 96

7.5 Evans & Mort correlation of peak velocity ratio at stall versus $\triangle S$ parameter correlated to the adverse velocity gradient. (Adapted from Evans & Mort [26]). 99

7.6 Sketch of Evans & Mort method. (Adapted from Evans and Mort [26]). 99

7.7 Normal force coefficient curves at two reduced pitch rates showing stall onset locations predicted by the Evans & Mort correlation and vorticity flux. The data are relative to the nominally two-dimensional NACA 0015 aerofoil. 100

7.8 Vorticity flux peak S^+ occurrence on the nominally two-dimensional NACA 0015 aerofoil and Evans & Mort prediction for a range of reduced pitch rates. 102

7.9 Vorticity flux peak S^+ occurrence at inboard sections of the rectangular wing and the Evans & Mort prediction. 103

7.10 Occurrence of vorticity flux peak S^+ on three span locations of the rectangular wing and on the nominally two-dimensional NACA 0015 aerofoil for a range of reduced pitch rates. 104

7.11 Occurrence of peak S^+ of vorticity flux at two span locations of rectangular wing and 60^0 swept-tip wing for a range of reduced pitch rates. 106

8.1 Pitching moment coefficient Cm around 25% of the aerofoil chord versus incidence. 110

8.2 Pressure coefficient contours plotted in space and time at three span locations of the rectangular wing at reduced pitch rate 0.0271. 112

8.3 Chordwise propagation of a pressure wave. 114

8.4 Suction peak associated with the convection of the dynamic stall vortex for the rectangular wing at a reduced pitch rate of 0.097. 117

8.5 Stall vortex position versus time for the two-dimensional NACA 0015 aerofoil and two span locations on the rectangular wing at reduced pitch rate of 0.023. 118

8.6 Vortex Convection speed versus reduced pitch rate for the rectangular wing and the two-dimensional NACA 0015 aerofoil. 119

8.7 Convection speed versus reduced pitch rate for the 60^0 swept tips wing and the nominally two-dimensional NACA 0015 aerofoil. 121

B.1 Pitch incidence variation against the time for reduced pitch rate 0.08. 138

B.2 Images of flow field at 57% of span of the rectangular wing for reduced pitch rate 0.08. (From Moir [100]). 142

B.3 Images of flow field at 75% of span of the rectangular wing for reduced pitch rate 0.08. (From Moir [100]). 143

B.4 Images of flow field at 90% of span of the rectangular wing for reduced pitch rate 0.08. (From Moir [100]). 144

B.5 Images of flow field on rectangular wing, view from above and behind for reduced pitch rate 0.08. (From Moir [100]). 145

B.6 Images of flow field on rectangular wing, view from upstream for reduced pitch rate 0.08. (From Moir [100]). 146

D.1 Pitch incidence variation versus time for reduced pitch rate 0.08. . . . 151

D.2 Images of flow field on 60^0 swept-tip wing for reduced pitch rate 0.08; view from upstream. (From Moir [100]). 152

D.3 Images of flow field on 60^0 swept-tip wing and reduced pitch rate 0.08; view from above and behind. (From Moir [100]). 153

Nomenclature

alpha Flow incidence, *(deg)*

A Wing area, (m^2)

AR Aspect ratio, $\frac{b^2}{A}$

b Wing span, (m^2)

c Chord aerofoil, *(m)*

$\bar{c}$ Mean chord, *(m)*

CM Pitching moment coefficient, $\frac{M}{\frac{1}{2}\rho U^2 \bar{c} A}$

CN Normal force coefficient, $\frac{N}{\frac{1}{2}\rho U^2 A}$

Cp Pressure coefficient, $\frac{p-p_\infty}{\frac{1}{2}\rho U_\infty^2}$

I Sphere's moment of inertia, $\frac{2}{5}mr^2$, (Kgm^2)

m Sphere's mass, *(kg)*

M Pitching moment, *(Nm)*

M_∞ Free stream mach number

N Normal force, *(N)*

p Static pressure at the surface, (N/m^2)

p_∞ Freestream static pressure, (N/m^2)

r Sphere's radius, *(m)*

Re_θ Reynolds number based on momentum thickness, $\frac{U\theta}{\nu}$

Re_c Reynolds number based on chord length, $\frac{cU_\infty\rho}{\mu}$

rpr Reduced pitch rate, $\frac{\dot{\alpha}c}{2U_\infty}$

s Coordinate along the aerofoil surface, *(m)*

S^+ Local source peak of dimensionless vorticity flux

S^- Local sink peak of dimensionless vorticity flux

t Dimensionless time

U Local velocity, *(m/s)*

U_∞ Freestream velocity, *(m/s)*

$\mathbf{n}$ Unit vector normal to the wall

$\mathbf{S_{flux}}$ Vorticity flux vector across a plane, $-\frac{1}{\rho}\frac{\partial p}{\partial s}$

$\mathbf{v}$ Velocity vector

ω Vorticity vector

α Flow incidence, *(deg)*

$\dot{\alpha}$ Pitch rate, *(deg/s)*

θ Boundary layer momentum thickness, *(m)*

μ Dynamic viscosity, $(m^{-1}s^{-1})$

ν Kinematic viscosity, (m^2s^{-1})

ρ Density, (kgm^3)

Chapter 1

Introduction

1.1 The Concept of Dynamic Stall

Dynamic stall is a phenomenon that affects aerodynamic bodies such as aerofoil, wings and rotors and, by definition, is an 'unsteady fluid-flow phenomenon'. The unsteadiness manifests itself when the body in question experiences a rapid change in inflow conditions, such as in the case of a helicopter rotor blade. Indeed, the helicopter has been the main focus for research into the nominally two-dimensional dynamic stalling of aerofoils. Dynamic stall occurs when the helicopter is either in rapid maneuvers or, more likely, at high forward speed when, in order to trim the rotor, the blade incidence must be increased on the retreating side. When dynamic stall does occur, it is a most severe event and, indeed, can increase the magnitude of the pitching moment by over tenfold. It is therefore, in general, an event to be avoided.

When dynamic stall does occur, a vortex is shed from the region of the leading edge of the blade and then moves rearwards over the upper surface and finally leaves the trailing edge. It is the movement of this dynamic-stall vortex that creates a large

negative pitching moment that can indeed twist the blades and impose very high loads on the helicopter control system.

All the detailed early work on dynamic stall pertained to the helicopter's rotor performance. The dynamic effect on a fixed wing aircraft undergoing rapid pitching moments was also appreciated and it was because of these effects that, when assessing the stalling speed of a fixed wing aircraft, the rate at which the pitch was allowed to increase was severely limited. More recently, however dynamic stall has become important when considering the performance of high maneuverability fighter aircraft. This was aptly demonstrated when a pair of SU-27S aircraft performed the spectacular cobra maneuver at the Farnborough Airshow in 1990. While the stalling mechanism on the fighter is different from that on the helicopter rotor, it is the dynamic effects that are important and make the flow highly unsteady. Moreover, in both cases the stall is affected by many factors and the main variables involved may be grouped as follows:

1 Geometry of the blade/wing, aerofoil shapes (thickness, leading edge radius, etc.), wing plan form, wing twist and surface roughness.

2 Reynolds and Mach number.

3 Motion to which the blade/wing is subjected including frequency, maximum amplitude of oscillation and instantaneous incidence.

The overall process of the stall was well described by Young in [131] and more detailed understanding of the specific events described by Young have been aided by researchers such as Galbraith et al. [38, 37, 36, 117], Carta [13, 12], McCroskey [91, 90, 92, 88, 89], Carr [10, 107, 9] and many more.

Until recently all the experiments carried out in the investigation of dynamic stall have considered nominally two-dimensional flow. Accepting, however, that dynamic stall is a three dimensional process, it followed naturally that investigators carried out three-dimensional dynamic stall experiments when the capability became available. To date very few such experiments have being performed and, in the main, these have been by Piziall at NASA Ames [106], Lorber and Carta at UTRC [82], Schreck at the United States Airforce Academy [121], Freymouth at the University of Colorado in Boulder [32] and Galbraith and Coton at the University of Glasgow [17].

The whole basis of the experiments is to be able to describe the associated flow phenomena to, at least, a first order. It was through the understanding of such phenomena in the nominally two-dimensional case that Beddoes [5] was able to produce his first generation dynamic stall model which subsequently became one of the most heavily used semi empirical models worldwide. The complexity of the model is hidden by the simplicity of the computer coding which results in an exceedingly fast assessment of the dynamic stall cycle. For a helicopter rotor, such calculations may be performed thousands of times and so they are essential for this work. The work on three-dimensional dynamic stall is aimed at providing additional information to assist with the upgrade of this model.

Accordingly, the aim of the present work is to take already collected three-dimensional dynamic stall data and attempt to describe associated flow phenomena. Once a consistent description, that has been validated, is developed, then the information can be incorporated into appropriate models.

1.2 A Short History of Stall

1.2.1 Experimental Investigations

The first relevant studies of stall can be dated from the beginning of the nineteen thirties when numerous wind tunnel investigations of the effects of Reynolds number revealed the role of boundary layer separation in the stall process. Initially, the study was focused on aerofoils because the comprehension of the stalling problem on wings could be gained by observing the process of boundary layer separation in a two-dimensional flow field. As a result, the first wind tunnel investigations were conducted to determine both the detailed nature of the static stall phenomenon and the resulting aerodynamic reactions on a two-dimensional lifting surface; among the first researchers we remember Jacobs [57] who speculated that the shape of the lift curve peak was controlled by the position and movement of the point of separation of turbulent flow on the aerofoil surface. Shortly thereafter, Millikan and Klein [99] correlated the type of boundary layer flow and separation with stalling. They suggested, after investigating the effect of turbulence on maximum lift, that the point of transition from laminar to turbulent flow relative to the point of laminar separation was critical in determining maximum lift. They pointed out that if transition moves ahead of the theoretical point of laminar separation, then the laminar stall cannot occur. They concluded that in such circumstances, an increased value of maximum lift might be realized because the turbulent boundary layer resists separation to a much greater extent than does the laminar boundary layer.

During the same time as the work of Jacobs [57] and Millikan [99],Melville [97, 98] investigated the stalling characteristics of several different aerofoil sections experimentally and made the first generalization of stalling characteristics. He classified three types of static stalling: a trailing edge stall, and two types of leading edge

stall. His significant conclusion was that the stall could result from flow separation at the leading edge as well as from the trailing edge of an aerofoil. Unfortunately, his experimental work was confined to force and pressure distributions so that the direct correlation of the types of stall with the boundary layer flow was not possible.

In a subsequent work, Jacobs and Sherman [58] related the type of flow separation to maximum lift characteristics and then to the stall in a discussion of the effects of Reynolds number on the aerodynamic characteristics of aerofoil sections. Moreover, they described the importance of the laminar and turbulent boundary layer in the leading and trailing edge types of stall. Loftin and Bursnall [80] extended the work of Jacobs and Sherman on the basis of experimental data. They pointed out the importance of a localized region of laminar separated flow behind the leading edge on the effects of Reynolds number on the maximum lift of aerofoil sections of various thickness to chord ratios.

Later, at the start of the nineteen fifties, at the Ames Aeronautical Laboratory, an investigation of the boundary layer and stalling characteristics of a wide range of NACA aerofoils illustrated three general types of low speed stalling characteristics similar to those of Melville's classification [42, 93, 94, 95, 96]. The classifications of static stalling were designated as:

Trailing edge stall where the stall is preceded by the movement of the turbulent separation point forward from the trailing edge with increasing angle of attack. This type of stall is characteristic of most thick aerofoil sections with thickness to chord ratios of approximately 15% and greater.

Leading edge stall where the stall is characterized by an abrupt flow separation near the leading edge without subsequent re-attachment. This stall is generally

inherent to most aerofoil sections of moderate thickness with ratios between 9% and 15%.

Thin aerofoil stall where the stall is preceded by flow separation at the leading edge with re-attachment at a point which moves progressively rear-ward with increasing angle of attack. This stall is typical on aerofoils with thickness ratios less than 9%. In the literature this mechanism of nose stall is generally referred to as 'long bubble bursting'.

During the nineteen sixties, research began to focus on dynamic stall and its effects on oscillating aerofoils. Carta [13], Ham [51, 52], and later Liiva et al. [79, 78] and Isogai [56], were among the first to carry out investigations on dynamic stall effects on aerofoils. They conducted a wide range of parametric experiments in order to obtain aerodynamic force and moment coefficients as functions of frequency and angle. From the analysis of the experimental data, they developed the first empirical techniques that attempted to represent the primary effects of dynamic stall on aerofoil lift and pitching moment characteristics.

In the nineteen seventies, a variety of other studies where conducted, whose aim was to improve the level of understanding of the basic aerodynamics of stalling aerofoils. Until then, most of the studies were carried out on aerofoils oscillating sinusoidally. Fukushima and Dadone [33], however, analyzed the significance of pitch versus plunge (vertical translational motion) effects on dynamic stall characteristics. Their study determined that, during the plunge motions, the flow field and airloads are qualitatively equivalent to those due to pitching oscillations but the stall, in terms of delay and strength, is dependent on the type of motion. Further investigations by Carta [12] and Maresca [85] confirmed that the stall onset parameters were dependent on the type of motion.

Later, at the start of the nineteen eighties, McCroskey conducted similar studies and showed the dependence of the normal force and pitching moment on amplitude of oscillation, frequency of oscillation and mean angle of attack [88, 89, 92]. Moreover, McCroskey and his co-workers performed a comprehensive series of studies on dynamic stall [92]. They provided a comparison of the effects of section geometry and once again concluded that dynamic stall onset is dependent on aerofoil shape which determines the nature of the initial boundary layer separation that precedes the vortex development. Subsequently, they analyzed the effects of changing leading edge shape on a NACA 0012 aerofoil undergoing pitching motion for a wide range of frequencies and Reynolds number [91, 92]. The study proved that, although several types of boundary layer separation characterized dynamic stall, three categories were mainly distinguished. These three types of stall are similar to the static stall equivalent. Moreover, the analysis discovered that in all dynamic stall cases a vortex forms at the leading edge which moves down the aerofoil and produces large normal forces and pitching moments. Finally it was observed that aerofoils with better static stall characteristics tended to exhibit better dynamic stall behaviour. For example, aerofoils that stall from the trailing edge in steady flow offer less severe dynamic loads in the dynamic stall environment. Lorber and Covert [83] investigated the development of the boundary layer on fixed aerofoils experiencing rapid changes in angle of attack induced by rotation of an elliptic cylinder below the aerofoil. They found that the unsteady boundary layer that develops under these conditions is strongly dependent on the characteristics of the transition region of the boundary layer on the aerofoil.

Besides the investigations of McCroskey on the aerofoil geometry effects, further studies of the role of the aerodynamic flow characteristics (Reynolds number, Mach number) on dynamic stall onset took place. Indeed, several authors discussed the

influence of Mach number on dynamic stall such as Lee et al. [68] who used holographic laser velocimetry to visualize the compressible flow on an oscillating aerofoil. Because of structural limitations, their results did not include the leading edge of the aerofoil. More information was gained by St. Hillaire and Carta [122] who observed that Mach number effects dominate during the onset of dynamic stall. The effect of Mach number was also documented by Carr [9] on several aerofoils performing different motions and all test conditions proved that when M_∞ increases, the dynamic performance of the two-dimensional models degrades quickly and the dynamic stall occurs earlier. The sensitivity to Mach number implies that the separation process can be due to significantly different physics and underlying processes such as shock and boundary layer interaction. In fact, when the Mach number increases, supersonic flow can develop locally on the aerodynamic surface. McCroskey and al. [92] indicated that near the leading edge at $M_\infty \geq 0.18$ there are local sonic conditions that accompany a strong tendency toward leading edge stall on all aerofoils, regardless of their behaviour at lower Mach number.

Not many authors have investigated the influence of Reynolds number on dynamic stall, since it is difficult to vary the Reynolds number significantly without introducing compressibility effects. However, Carr and his co-workers [10] studying the effects of frequency, amplitude of oscillation and Reynolds number over four aerofoils assessed that the effect of Reynolds number was less dramatic. It seemed that an increasing Reynolds number delays the advent of flow reversal on the rear of the aerofoil, but it did not seem to effect the dynamic stall process on the forward part of the aerofoil. Furthermore, a study of free stream turbulence effects was performed for the design of wind turbines, since the intensity of atmospheric turbulence can reach high levels in the wind boundary layer. Lanville and Vittecoq [67] determined that free stream turbulence intensity can have a significant effect on the develop-

ment of the dynamic stall at low Reynolds numbers but the causes were not clear.

In the early nineteen nineties Galbraith and his co-workers [102, 38, 48] investigated the physics of the stall process through the analysis of pressure data from several two-dimensional aerofoil models performing at constant pitch rates in both ramp-up and ramp-down motion. They discovered that the aerofoil pressure distribution shows signs of the development and convection of structures at the leading edge and trailing edge which indicate what are described as leading and trailing edge mechanisms. Moreover they established that the mechanisms of leading edge stall is predominant when the nature of the boundary layer is altered by placing a transition strip at the leading edge.

Until the second half of the nineteen eighties, almost all dynamic stall experiments considered nominally two-dimensional aerofoils. The first significant studies on three-dimensional stall can be dated from around this time. Flow visualization studies documented the morphology of portions of three-dimensional unsteady flows elicited by pitching wings [1, 3, 32, 35, 111]. These investigations concentrated their attention on the prominent leading edge and wing tip vortices, and successfully constructed physical models based upon vorticity conservation to explain the evolution of the vortex near the wing tips. Fewer experiments employed surface pressure measurements to characterize the three dimensional unsteady flow field development on pitching wings [81, 112]. Galbraith and Coton [17] examined three-dimensional dynamic stall by measuring unsteady pressure distributions on three wing plan-forms during motions of pitching and ramping up. Moir and Coton [100] provided additional information on the structure and behaviour of the unsteady flow field for a straight rectangular wing and a rectangular wing with 60^0 swept tips utilizing flow visualization. In particular, their study concentrated on the evolution of the dy-

namic stall vortex and its interaction with the tip-vortices which could not be fully identified by surface pressure measurements alone. St. Hillaire and Carta [122] investigated the effects of sweep on an oscillating wing model at an angle with respect the free stream. They proposed that sweep geometry can have a first order effect on the development of the stall vortex and the resultant aerodynamic loads. In fact, they found that the sweep geometry delays the onset of the dynamic stall vortex and tends to reduce the rate of change of the lift and pitching moment coefficient as the stall begins.

1.2.2 Reconstruction and Prediction of the Stall Process

In the nineteen seventies, as the experimental investigation on dynamic stall clarified the basic physical aspects of the phenomenon, numerous studies, parallel to the experimental research, began focusing on the development of techniques able to predict or reconstruct the stall behaviour. These methods seek to correlate force and moment data obtained from wind tunnel tests in a formulation that models the effects of the numerous relevant parameters such as aerofoil shape, Mach number, amplitude and frequency of oscillations, type of motion, and velocity distribution, leading edge geometry and adverse pressure. Among these methods one of the most common is the so-called *gamma functions method* developed by Boeing-Vertol [90]. The gamma functions are effectively two functions, one for the lift and one for the moment curve. These functions were generated from a large amount of data generated in transonic wind tunnel tests on various aerofoils oscillating sinusoidally in pitch and at several Mach numbers. The analytical *Lockheed method* provided by Ericsson and Reding [23] is based on static experimental data to predict the separated flow effect on the incompressible unsteady aerodynamics. In the Lockheed method the key parameters in the analytic relationship between the steady and unsteady aerodynamics are the following: (i) the time lag occurring before a

change of conditions can affect the separation-induced aerodynamic loads; (ii) the accelerated flow effect (e.g. the pressure gradient lag relative to the static aerodynamic characteristics); (iii) the moving wall effect (e.g. the effect of the non-steady boundary condition at the body surface). The United Technologies Research Center (UTRC) [41] developed a time domain unsteady aerodynamic model using only three parameters: the instantaneous angle of attack, the non-dimensional pitch rate and the non-dimensional angular acceleration. This techniques is known as the *a, α, B method* and it is, once again, based on oscillating aerofoil tests. A detailed review of some other methods such as the *Time-delay method, MIT method* and *ONERA Method* is given by McCroskey, [88]. The limit of all semi-empirical techniques is that they reproduce well most of the data sets that were used in their development but they can not give an accurate prediction of dynamic stall for an independent set of data. Nevertheless, in the absence of more accurate techniques, these methods are currently in use as part of the main design process by the helicopter industry.

Recently, many physical flow phenomena associated with dynamic stall have been clarified by the numerical simulation of the unsteady flow. This has been possible thanks to the considerable progress that Computational Fluid Dynamics (CFD) has made in simulating complex, unsteady, attached and separated flow using potential flow, boundary layer, viscous-inviscid interaction methods and the Euler and full unsteady Navier-Stokes equations. Detailed accounts of the computational methods can be found in books by Anderson et al. [2], Hirsch [53] and Fletcher [30]. The numerical methods are calibrated and validated against the large database of experimental investigations of aerofoil dynamic stall.

The majority of the numerical work has been directed toward the investigation and prediction of two-dimensional dynamic stall flow fields [29, 108, 114, 127]. Only

recently, unsteady, three-dimensional flow fields [21, 20] have been calculated for pitching [101], oscillating [115, 130] wings and jets [15].

1.3 Objective and Approach of Current Work

It is apparent from the foregoing discussion that in the last seventy years experimental and numerical studies have achieved significant progress in understanding the physics of the dynamic stall process. However, many aspects of this phenomenon are still unclear. These are the behaviour of the flow in the early stages of the evolution of the dynamic stall vortex; the mechanism responsible for this evolution process; the role of the body geometry, fluid dynamic and unsteady factors on the onset of the stall vortex. Moreover, both empirical and numerical methods cannot accurately predict the stall in two-dimensional and certainly not in three-dimensional flow fields. It is in this context that the research presented in this manuscript takes place.

The object of this research is to enhance understanding of the physical process of dynamic stall in the three-dimensional environment, so that it may ultimately be controlled and avoided. In particular, this research focuses on a consideration of the onset of the dynamic stall vortex on finite wings. The study is based on the assumption that the unsteady flow over the inner cross-sectional surfaces of three-dimensional wings has nominally two-dimensional features. This assumption is investigated by a parallel study of the flow behaviour over a nominally two-dimensional aerofoil in order to reveal and highlight the three-dimensional effects. The work described also involves the investigation of the key role of wing tip geometries and angular velocity on the features of three-dimensional dynamic stall. The outcome of the work may provide the basis for a fast and general method for the prediction

of dynamic stall.

To underpin the research, a large database of static pressure data was analyzed with the aim of exploring and understanding the behaviour of the dynamic stall vortical structures present on the wing surfaces. The pressure data are the results of wind tunnel tests carried out by Galbraith and Coton [60, 61, 62, 39]. The particular test cases studied were from tests on two wings (a straight rectangular wing with solid of revolution at its tips and a rectangular wing with 60^0 swept tips) and a nominally two-dimensional NACA 0015 aerofoil, all pitched around the quarter chord over a range of reduced pitch rates. Both wings had a NACA 0015 cross-section.

The present study was initiated with a background study of two- and three-dimensional unsteady flow field behaviour over rectangular wings undergoing pitching motion. The flow visualization tests carried out by Moir and Coton [100] and Laghezza [66] were particularly useful. The flow visualization provided qualitative information on the unsteady flow field generated by the pitching motion of a rectangular wing with solids of revolution at its tips and a rectangular wing with 60^0 swept tips. The flow visualization helped to illustrate the basic behaviour (onset, growth and convection) of the dynamic stall vortical structure that develops along the leading edge of the wings, see Chapter 3.

The behaviour exhibited in the flow visualization provided the key to understanding the changes in the pressure data at each section of the pitching wing. Further investigation of the pressure in terms of normal lift coefficient provided supplementary information on the influence of the reduced pitch rate on the events (in terms of time and severity) of dynamic stall. Furthermore, the correlation of the pressure data recorded over the three-dimensional wing surface and the nominally

two-dimensional NACA 0015 aerofoil highlighted the major differences between two and three-dimensional dynamic stall, see Chapter 4.

Further insight into the origin, evolution and structure of the dynamic stall vortex was gained through analysis of the generation of vorticity on the wing surface, Chapter 5. It is shown that analysis of the vorticity can provide the basis for a practical engineering tool to predict the onset of dynamic stall, see Chapter 7.

The effects of the wing-tip geometry on the dynamic stall process are studied by comparing the qualitative features of the dynamic stall vortex and the quantitative aerodynamic behaviour of a rectangular wing with those of a swept-tip wing with the same cross-section, see Chapter 6.

Finally, the characteristics of vortex convection along the chord of both wings and the aerofoil are examined in Chapter 8. Conclusions and recommendations for future work are discussed in Chapter 9.

Chapter 2

Description of Test Facility

2.1 Introduction

Over the past ten years, the University of Glasgow has developed both nominally two-dimensional and three-dimensional dynamic stall test facilities. These have been used by Galbraith et al., who focused on the understanding of the two-dimensional dynamic stall phenomenon, [37, 36, 47, 49, 46, 72], and later by Coton et al. who carried the investigation on the three-dimensional flows, [100, 28, 17, 18]. In all cases, the test models were subjected to four types of motions: steady, oscillatory (sinusoidal) and constant pitch-rate ramp motions in both positive and negative directions.

The two-dimensional data were acquired on a number of aerofoils that can be considered as belonging to two distinct groups. The first group is a family of cambered aerofoils derived from the NACA 23012 section. These were used to examine the transition from trailing edge to leading edge stall and the mechanism of reattachment on helicopter rotor blade type sections. The second group is a series of symmetric sections for use on large scale vertical axis wind turbines. A detailed summary of

the aerofoil test database and testing procedure is given in reference [38]. The three-dimensional tests were conducted on three different wing planforms in order to study the role of the geometry of the wing in dynamic stall. The planforms considered were a rectangular wing, delta wing and rectangular wing with 60^0 swept tips.

Here an analytical study of part of the above substantial database is presented. The particular data are from ramp-up tests over a broad range of reduced pitch rates on a nominally two-dimensional NACA 0015 aerofoil and on two three-dimensional planforms: a straight rectangular wing with simple solids of revolution at its tips and a rectangular wing with 60^0 swept tips.

2.2 Wind Tunnel Tests

Both the two-dimensional and three-dimensional tests, which provided pressure data for the present work, were carried out in the University of Glasgow 'Handley Page' wind tunnel. The 'Handley Page' low-speed wind tunnel is an atmospheric-pressure closed-return type with a 2.13 x 1.61 meter octagonal working section in which wind speeds of up to 61 m/s can be achieved. In particular, for the test cases presented here the wind speed was set at around 45 m/s which corresponds to a Reynolds number based on aerofoil chord length and free-stream Mach number of around 1.5 million and 0.11 respectively.

2.2.1 Two-Dimensional Pitch Drive Mechanism

In the two-dimensional tests the tunnel spanning aerofoil model was mounted vertically in the wind tunnel and was pivoted about its quarter chord axis on two tubular steel shafts connected to the main support via two self aligning bearings. A single thrust bearing on the top support beam took all the weight of the model. The

aerodynamic loading from the aerofoil was reacted to the tunnel framework by two transversely mounted beams. A schematic of the facility is depicted in Figure 2.1. A more detailed description of this facility is provided in [39].

2.2.2 Three-Dimensional Pitch Drive Mechanism

In the three-dimensional tests the wing models were mounted horizontally and supported on three struts, as shown in Figure 2.2. These were connected to the main support structure and actuation mechanism which was situated below the tunnel. Movement of the model was produced by displacement of the two rear struts which resulted in the model being pivoted about the quarter chord on a tool steel shaft connected to the front support via two self aligning bearings. Further detail on this test facility is available in [60, 61].

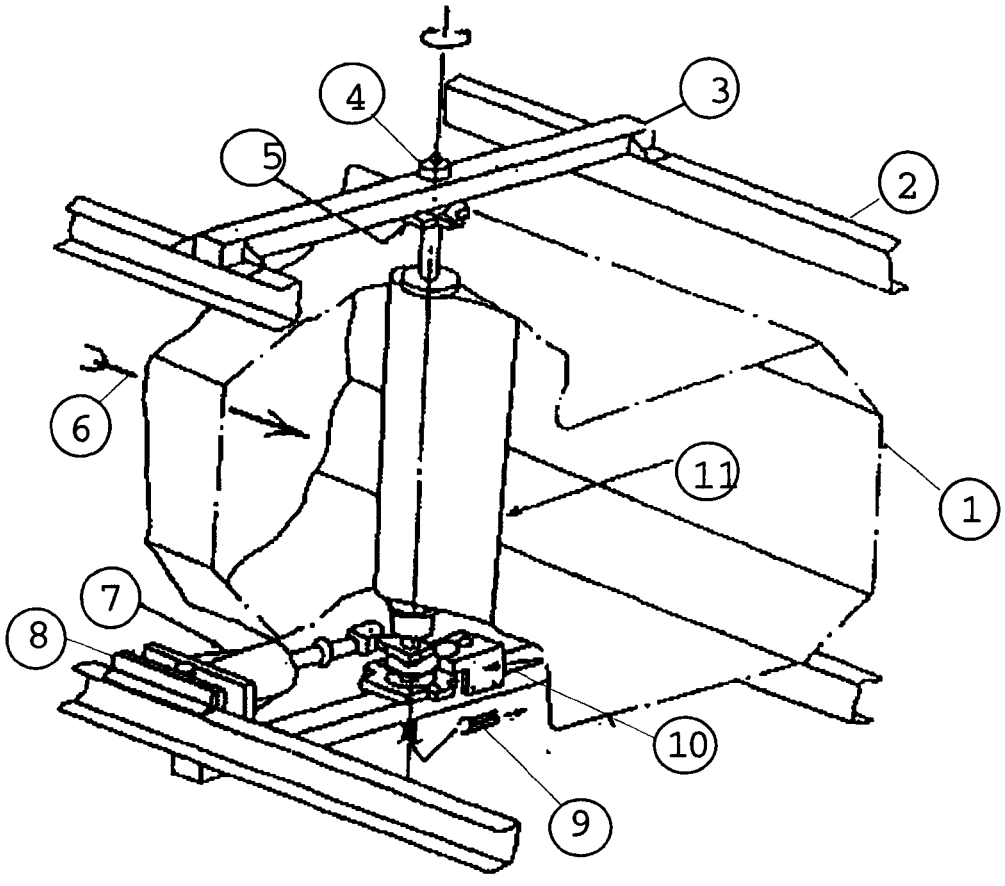

1	Tunnel Working Section	**5**	Support Bearing	**9**	Signal Cables
2	Tunnel Frame	**6**	Wind Direction	**10**	Displacement Transducers
3	Model Support	**7**	Hydralic Actuator	**11**	Wing Model
4	Thrust Bearing	**8**	Hinge		

Figure 2.1: Schematic of wind tunnel test set up; two-dimensional tests. (From Galbraith et al. [39]).

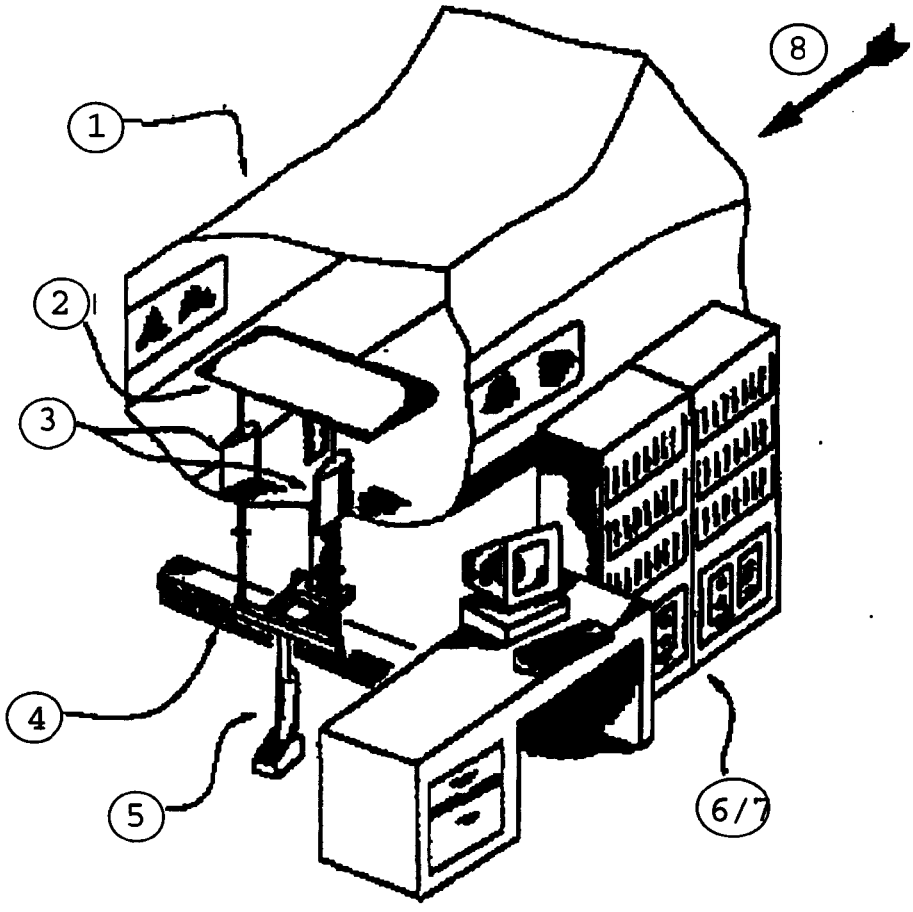

1	Tunnel Working Section	**4**	Main Support	**8**	Wind Direction
2	Wing Model	**5**	Hydralic Actuator		
3	Fairings	**6**	Signal Conditioning		
4	Main Support	**7**	Acquisition System		

Figure 2.2: Schematic of wind tunnel test set up; three-dimensional tests. (From Jiang et al. [62]).

2.3 Test Models and Procedure

2.3.1 NACA 0015 Aerofoil

The two-dimensional data analyzed in the present study were obtained from tests on a NACA 0015 cross-section model of chord length 550 mm and span 1610 mm that was equal to the full tunnel height. It was constructed from fibre glass mounted on an aluminum spar and filled with an epoxy resin foam.

To provide the chord-wise pressure distribution at the mid-span, thirty KULITE XCS-093-5 PSI G ultra-miniature pressure transducers were installed just below the surface of the model. The transducers were of vented gauge type with one side of the pressure sensitive diaphragm open to ambient pressure outside the wind tunnel. Each transducer was fitted with a temperature compensation module, which minimized the change in zero-offset and sensitivity to temperature. The locations of the pressure transducers along the chord of the model are illustrated in Figure 2.3 and detailed in Table A.2 of Appendix A.

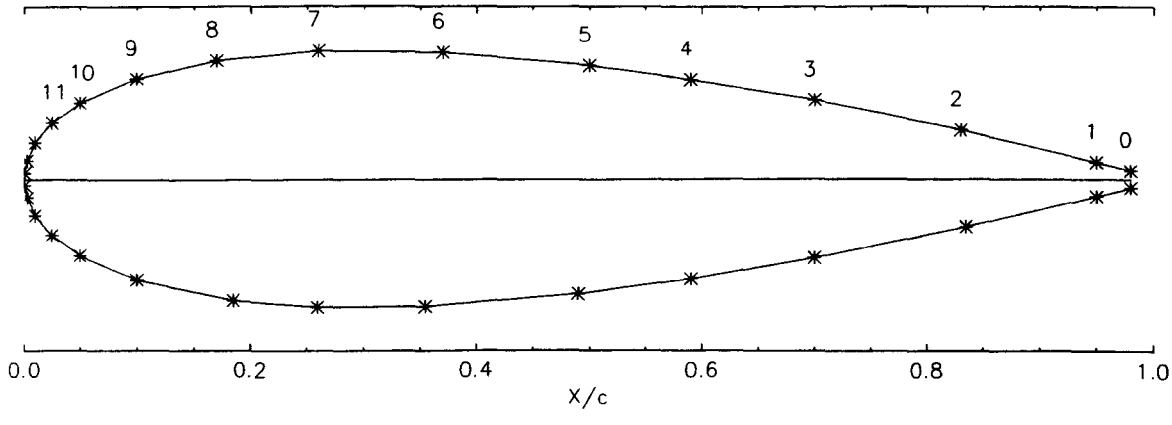

Figure 2.3: NACA 0015 aerofoil model.

2.3.2 Rectangular Wing Planform

The rectangular wing model had a NACA 0015 cross-section and simple solids of revolution at its tips, Figure 2.4. Because the lift behaviour at low aspect-ratios (AR) is quite different from that at high aspect ratios, particularly when AR is less than 2.0, the AR of this model was chosen as 3.0 to avoid strong three-dimensional effects at the mid span in steady flow. The model was sized in order to diminish the effect of up-wash from the wind tunnel walls near the wing tips of the model and to avoid significant blockage. The final overall dimensions were 1260 mm x 420 mm which resulted in a variation of model blockage from a minimum of 2.6% to a maximum of 11.35% model span to tunnel width ratio of 0.592. According to previous studies of the blockage effect in two-dimensional dynamic stall testing, these dimensions were considered acceptable [60, 61]. The model was constructed with an aluminum framework of ribs and stringers and an outer epoxy glass-fiber skin.

To log the data, 192 pressure transducers were placed within the model predominantly to the starboard side. There were six chordal distributions at various span-wise locations, each of which had 30 transducers. In the region of the tip, additional transducers were placed between the above mentioned sections to provide a better assessment of the tip vortex movement and structure. Moreover, to check on the overall symmetry of the flow, two transducers were placed on the left side of the wing in corresponding positions to their counterparts on the starboard side. The Tables A.3 - A.5 of Appendix A provide the locations of the transducers along the chord at each span-wise location of the wing. All pressure transducers were of KULITE differential type CJQH-187 with one side of the pressure diaphragm open to the ambient pressure outside the wind tunnel via tubing.

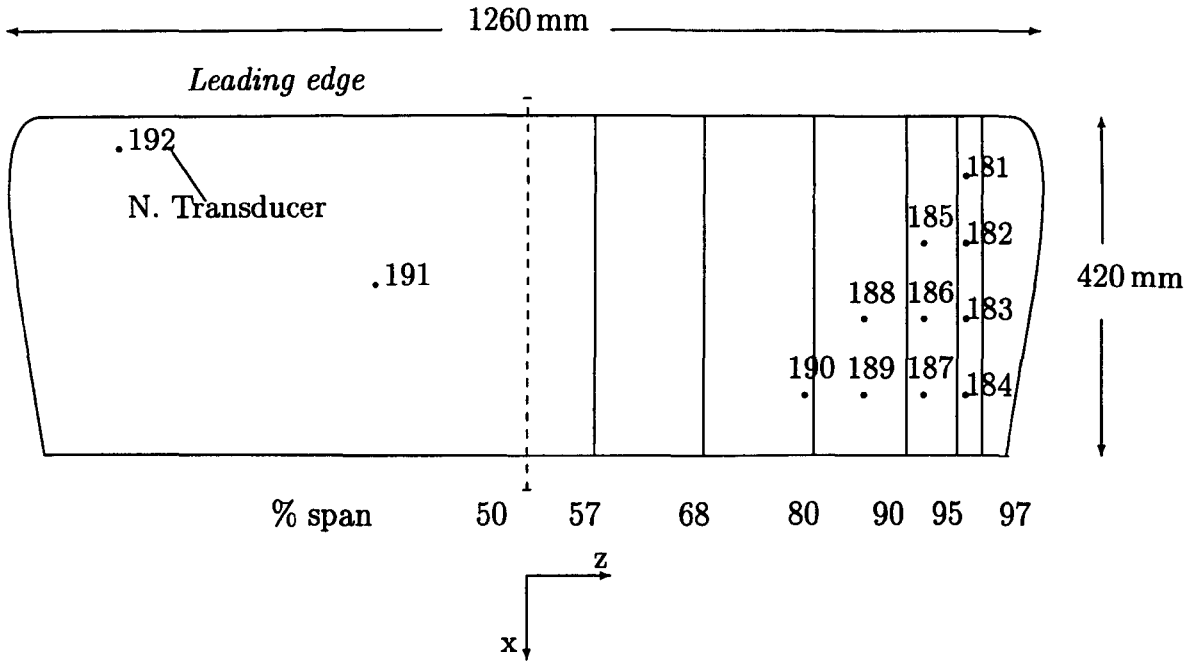

Section	Transducers	Section	Transducers	Section	Transducers
57% span	1-30	80% span	61-90	95% span	122-150
68% span	31-60	90% span	91-121	97% span	151-180

Figure 2.4: Test model of the rectangular wing with simple solid of revolution at its tip. (Adapted from Jiang et al. [60]).

2.3.3 60^0 Swept-Tip Wing Planform

The rectangular wing with 60^0 swept tips wing model also had a NACA 0015 cross-section. At the wing tips, the aerofoil profile shape was retained over approximately the first 15% of the chord and the intersection between the swept edge and the leading edge was rounded. On aft portions of the swept tips, the cross-sectional shape was tapered down to produce sharp tip edges. The planform of the wing is shown in Figure 2.5. The overall dimensions of the model were 1260 mm x 420 mm.

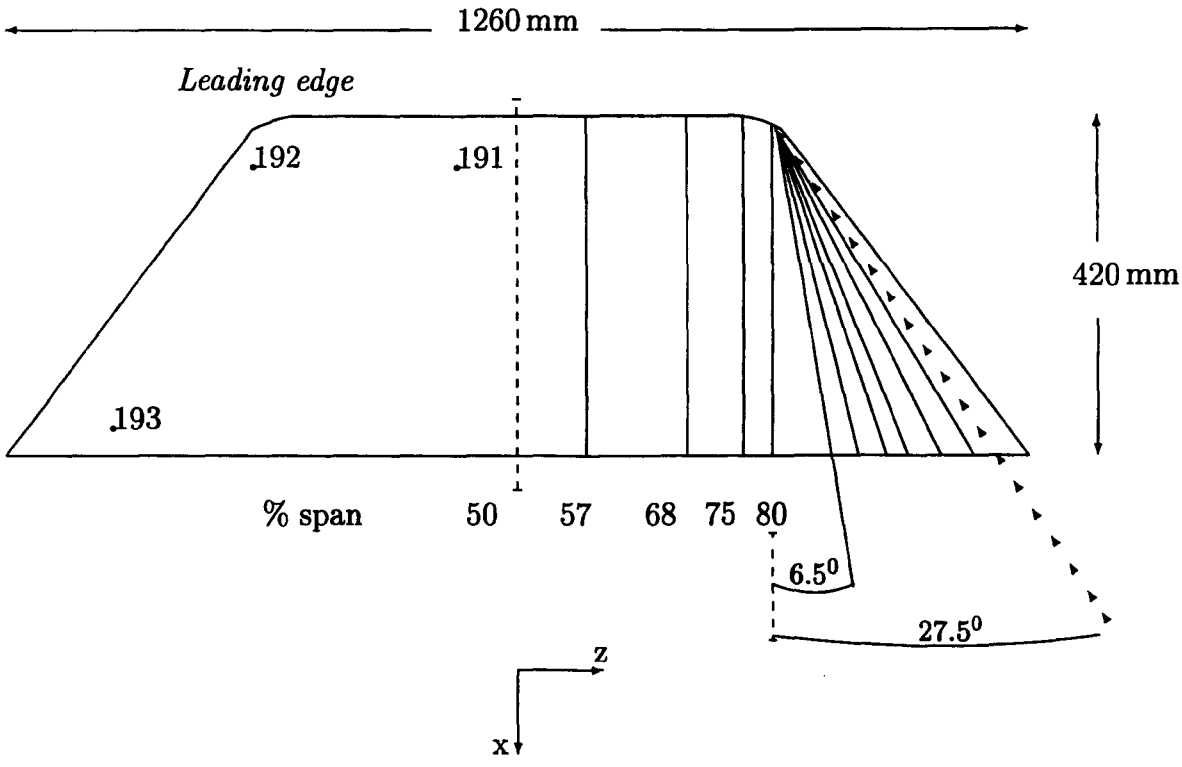

Section	Transducers	Section	Transducers	Section	Transducers
57% span	1-29	6.5 deg	110-123	22 deg	170-175
68% span	30-58	11.5 deg	124-139	25 deg	176-182
75% span	59-877	15 deg	140-156	27.5 deg	183-190
80% span	88-109	19 deg	157-169		

Figure 2.5: Test model of the rectangular wing with 60^0 swept tips. (Adapted from Jiang et al. [62]).

Altogether, 193 pressure transducers were placed within the model predominantly on the starboard side. There were four chordal distributions at inboard span-wise locations, each of which had 29 transducers. In the region of the tip, transducers were arranged in angular lines emanating from the leading edge corner to capture the pressure footprint of the tip vortex. In order to check on the overall symmetry of the flow, two transducers were placed on the left side of the wing in corresponding

positions to their counterparts on the starboard side. Additionally, three accelerometers were embedded in the wing, two of which were at the rear tip locations and a final one mounted centrally. The Tables A.6 - A.9 in Appendix A provide the location of the transducers along the chord at each span-wise section of the wing. All pressure transducers were of KULITE differential type CJQH-187 with one side of the pressure diaphragm open to the ambient pressure outside the wind tunnel via tubing.

Table 2.1 presents a résumé of the aerodynamic and geometric characteristics of the test cases introduced in this chapter. The pressure data recorded on these models during ramp-up are tests are the focus for the research presented in the following chapters. The analytical study of these data will be supported by flow visualization analysis, carried out by Moir & Coton [100] and Laghezza [66] on geometrically similar models and similar free-stream conditions as indicated in Tables 3.1, 3.2, 5.1. Finally, in the following dissertation the terms *'rectangular wing'* and *'swept-tip wing'* will be refer to the rectangular wing with simple solids of revolution at its tips and the rectangular wing with 60^0 swept tips respectively.

	NACA 0015 Aerofoil	Rectangular Wing	Swept Tips Wing
Re_c	$1.5 \cdot 10^6$	$1.5 \cdot 10^6$	$1.5 \cdot 10^6$
M_∞	0.12	0.16	0.16
AR	2.9	3	3.7
Chord, mm	550	420	420
Span, mm	1610	1260	1260
No Sections	1	6	11
No Transducers	30	192	193

Table 2.1: Characteristics of the test cases analyzed in this work.

2.4 Ramp-up Experiments

During ramp-up tests, the models were rotated about the quarter chord over a pre-set arc at a constant pitch rate. Between each ramp, the model sat at the finishing angle for five seconds, moved smoothly back to the starting angle in five seconds and sat at this position for five seconds longer. Five cycles of 256 samples per transducer were recorded during each two-dimensional experiment and 4 cycles of 8000 samples for each transducer were recorded during the three-dimensional tests. The data examined in this work are the average of those consecutive cycles. In fact, previous experience [118] has shown that there exist minor random differences in data from cycle to cycle for dynamic tests and that the salient features are highlighted by the averaging process. In this work are presented only few of the several hundred test

cases recorded. Tables 2.2, 2.3, 2.4 give the specifications of the tests presented in the following analysis. A complete list of the test cases studied during this work is recorded in AppendixA, Table A.1. A FORTRAN code was used to produce the integrated force and vorticity flux. All graphical presentations were made using the MATLAB software suite.

Aerofoil	*chord, mm*	*span, mm*	*AR*
NACA 0015	550	1610	2.9

$\dot{\alpha}$	*rpr*	$10^6 Re_c$	M_∞
29.681	0.0034	1.47	0.12
44.173	0.0051	1.47	0.12
59.461	0.0068	1.47	0.12
74.985	0.0086	1.47	0.12
90.423	0.0104	1.47	0.12
129.539	0.0152	1.48	0.12
173.022	0.0203	1.47	0.12
225.111	0.0264	1.46	0.12
234.455	0.0274	1.47	0.12
245.874	0.0287	1.46	0.12

Table 2.2: List of ramp-up tests, NACA 0015 aerofoil.

Wing	*chord, mm*	*span, mm*	*AR*
Rectangular	420	1260	3

$\dot{\alpha}$	*rpr*	$10^6 Re_c$	M_∞
45.202	0.0029	1.49	0.16
91.155	0.0059	1.47	0.16
117.472	0.0080	1.47	0.16
142.638	0.0096	1.48	0.16
160.243	0.0108	1.48	0.16
248.981	0.0165	1.48	0.16
366.563	0.0245	1.48	0.16
404.442	0.0266	1.47	0.16
414.286	0.0273	1.47	0.16
416.944	0.0271	1.47	0.16

Table 2.3: List of ramp-up tests, rectangular wing.

Wing	*chord, mm*	*span, mm*	*AR*
Swept Tips	420	1260	3.7

$\dot{\alpha}$	*rpr*	$10^6 Re_c$	M_∞
44.902	0.0029	1.50	0.16
88.909	0.0057	1.52	0.16
116.322	0.0075	1.52	0.16
139.936	0.0091	1.51	0.16
157.540	0.0105	1.51	0.16
234.355	0.0156	1.51	0.16
387.356	0.0248	1.51	0.16
404.252	0.0259	1.50	0.16
419.047	0.0269	1.51	0.16
437.394	0.0279	1.51	0.16

Table 2.4: List of ramp-up tests, swept tips wing.

Chapter 3

Flow Field around a Pitching Rectangular Wing Planform

3.1 Introduction

As already mentioned in section 1.3, the aim of this research is to provide the basis for a semi-empirical technique for the prediction of the dynamic stall through the analysis of unsteady pressure data. Before going into this analysis, however, the acquisition of a preliminary knowledge of the general flow behaviour over test models undergoing pitching motion is required. Previous flow visualization tests carried out in the University of Glasgow provided a valuable source of information. In particular, the available images show the general unsteady flow field behaviour over the test model described in Chapter 2 and contribute to a basic understanding of the events associated with the dynamic stall process. A discussion of these flow visualization images is given in this chapter to set the scene for the subsequent data analysis.

The following discussion is based on the flow topology analysis presented by Moir

and Coton in [100] on a pitching rectangular wing model with simple solids of revolution at its tips, NACA 0015 cross sectional profile and aspect ratio equal to three, Table 3.1. The rectangular wing was studied in laminar flow conditions at a chord Reynolds number of approximately 13,000 during ramp-up tests. During the test the model was pitched around the quarter-chord line from 0^0 to 40^0, at a reduced pitch rate of 0.08 and then held stationary until the flow developed and convected from the trailing edge. The specifics of the unsteady flow behaviour can be read in Appendix B where the images and the observations of Moir and Coton are presented. Detailed information regarding the technical aspects of the experiment may be found in the internal Glasgow University report quoted in reference [100]. What follows in the next section is a simplified description of the three-dimensional flow field response on the aforementioned rectangular wing during a ramp-up test. The description of the flow behaviour focuses specifically on the flow aspects associated with the dynamic stall process.

Rectangular Wing	Section	Re_c	Chord, mm	Span, mm	AR
tip:solid of revolution	NACA 0015	13000	200	600	3

Table 3.1: Characteristics of three-dimensional flow visualization experiments, rectangular wing.

3.2 Description of Flow Behaviour

The flow visualization images in Appendix B highlight the dominant features of the unsteady flow field around the pitching rectangular wing with rounded tips and, in particular, show how complicated the three-dimensional flow behaviour is during the dynamic stall process. The flow field is characterized by a fascinating evolution of inter-connected regions of vorticity where two main vortical structures are

identified: the dynamic stall vortex emanating from the leading edge region and the vortices arising from the wing tips. There is also a third vortical structure behind the dynamic stall vortex near the mid-chord. This vortex is termed the shear layer vortex, which is a collection of vorticity originating in flow reversal near the trailing edge. The manner in which all three of these vortices influence and interact with one other is quite complex. An attempt to represent the physics of the dynamic stall process is made in Figure 3.1. The graphical sketch in Figure 3.1 is a very simplified representation of this network of connectivity and points out only the behaviour of the dynamic stall vortex and its interaction with the tip vortices. The shear layer vortex has not been identified in the sketch because, from the flow visualization, it appears to merge with the dynamic stall vortex and to have negligible influence on the events of dynamic stall. The evolution of the vortex structures sketched in Figure 3.1 is described below. It should be noted that the flow field behaviour described below is common to any ramp-up test at moderate ($O(10^2)$) pitch rates and the timing of the events is a function of the reduced pitch rate. For this reason, the events identified are not associated with specific incidences.

Soon after the wing starts pitching, the viscous flow along the leading edge of the wing rolls-up around the axial direction parallel to the wing-span. This flow then evolves in a three-dimensional vortical structure termed the dynamic stall vortex that arises near the quarter chord of the wing. The dynamic stall vortex initially grows almost uniformly along the span, sketch 3.1.a. The uniformity of the vortex growth is, however, short-lived and the vortex system starts to exhibit strong three-dimensional features very soon after it is formed. In particular, flow at the wing-tips spirals along the dynamic stall vortex towards the mid-span. There the angular momentum of the flow in the vortex appears to be higher. This suggests that the segments of the dynamic stall vortex structures in this region are stronger

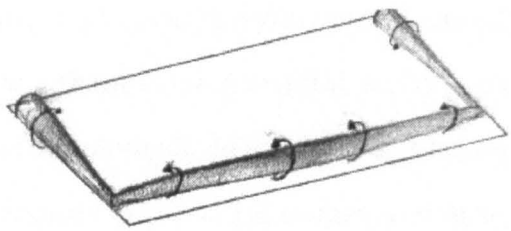

(a) Uniform Vortex Inception

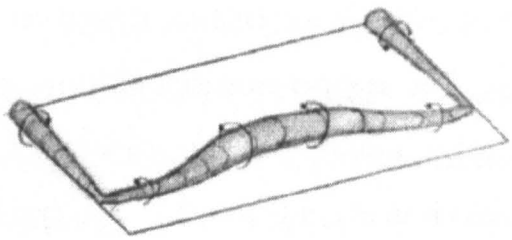

(b) Initial Vortex Movement

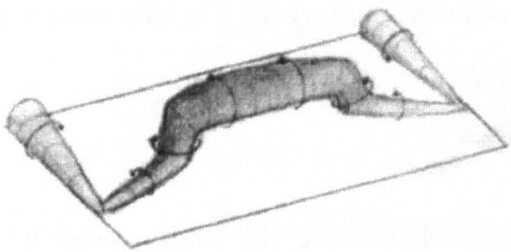

(c) Omega Structure

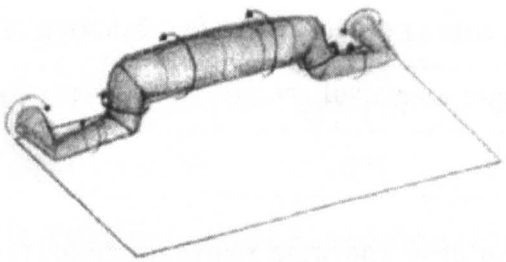

(d) Near the Trailing Edge

Figure 3.1: Vortex system on Rectangular Wing

than those on outboard sections. Eventually at an incidence that varies with the reduced pitch rate, the vortex system starts to convect down the chord, sketch 3.1.b, moving faster at the mid-span than on outboard locations. At the beginning of the ramp-up, the flow around the wing tips turns into a vortex-structure whose direction of rotation is from the lower- to the upper-surface of the wing, sketch 3.1.a,b. The vortices at the wing tips interact with the weaker segments of the dynamic stall vortex close to the wing tips and the result is that these segments of the dynamic stall vortex are held close to the wing surface. Meanwhile, the dynamic stall vortex at the mid-span grows in size and tends to lift from the surface, thus forming the so-called 'Omega' structure, sketch 3.1.c. The subsequent downstream convection of the dynamic stall vortex system is very complex with differential convection rates across the span, Chapter 8. Ultimately, however, the vortex system passes the trailing edge almost uniformly, sketch 3.1.d.

The above description does not take into account the reversed flow originating at the trailing edge and moving upstream along the chord. Although the flow visualization analysis has identified the presence of this layer of reversed flow, the arrival of the flow reversal at the leading edge region and the formation of the dynamic stall vortex appear to be essentially separate flow phenomena. In fact, in Figure B.2, first column and second row, it emerges that the formation of the dynamic stall vortex structure has already started when the trailing-edge separation has reached 60% of the chord. This implies that the dynamic stall vortex is not the result of the interaction between vorticity collected at the leading-edge region and reverse flow coming from the trailing-edge. Consequently, the trailing-edge flow does not appear to have a direct impact on the onset of the dynamic stall vortex. In fact, Shih [119] came to the same conclusion through a simple time/space development calculation. In addition, it may be anticipated that the reversed flow will not dominate the flow

field at the trailing edge at high reduced pitch rate (rpr > 0.03) because at high values of reduced pitch rate the flow stays attached to the surface (see Chapter4) whilst the vortex still forms at the leading edge. This suggests that the initiation of the dynamic stall vortex is a consequence of events near the leading edge and is not triggered by the arrival of reversed flow originating at the trailing edge.

3.3 Two-Dimensional Assumption

Numerous research studies have investigated the physical mechanism of dynamic stall in the nominally two-dimensional case and have shown how the features of this phenomenon are affected by geometric, aerodynamic and unsteady parameters like the shape and thickness of the aerofoil [90], [129], Reynolds [129] and Mach numbers [77], [34] and motion of the model [85], [33], [12]. In this work the attention is focussed on unsteady three-dimensional flows, but it is useful first to highlight the behaviour of two- and three-dimensional flows. For this reason, a discussion of the unsteady flow behaviour around a nominally two-dimensional NACA 0015 aerofoil now follows. This discussion is based on the observations of Laghezza [66] made during his flow visualization study on a two-dimensional NACA 0015 aerofoil, Table 3.2. The aerofoil was pitched around the quarter-chord line from 0^0 to 40^0 at a number of reduced pitch rates and then held stationary until the flow developed and convected from the trailing edge. The unsteady flow development over the test model was studied in laminar flow conditions at a chord Reynolds number of approximately 15,000. Detailed information on the technical aspects of these experiments, may found in reference [66].

Rectangular Wing	Section	Re_c	Chord, mm	Span, mm	AR
sharp tips	NACA 0015	15000	230	1380	6

Table 3.2: Characteristics of nominally two-dimensional flow visualization experiments, NACA 0015 aerofoil.

The work of Laghezza revealed that the unsteady flow response at all pitch rates is qualitatively characterized by the same primary features although the timing of specific events and strength of the vortical flow features depends on the reduced pitch rate. The flow visualization images identified two main flow field structures whose growth and interaction dominate the flow at moderate pitch rates. The development and evolution of these features is described below.

At zero incidence the viscous flow around the nominally two-dimensional NACA 0015 aerofoil is symmetric. During ramp-up motion, as the angle of attack increases beyond the static stall angle, the viscous flow around the aerofoil stays thin and the global flow field is essentially inviscid in nature. Eventually, however, the boundary layer on the surface of the aerofoil shows symptoms of flow reversal that spreads from the trailing edge toward the leading edge as the angle of attack continues to increase. By virtue of the reversed flow, that has spread over half of the length of the chord, a noticeable shear layer begins to form near the mid-chord of the aerofoil. At an incidence, which changes with the reduced pitch rate and depends on many parameters (Reynolds and Mach numbers, reduced pitch rate, aerofoil curvature etc.), the viscous flow in the leading edge region no longer remains thin and attached and a very strong vortical flow develops: the dynamic stall vortex. As the aerofoil pitches-up, the dynamic stall vortex grows in size and the shear layer behind it evolves into a shear layer vortex. Suddenly, the dynamic stall vortex stops ex-

panding and then moves down the aerofoil merging with the shear layer vortex. The resulting large vortical structure then convects downstream along the aerofoil chord.

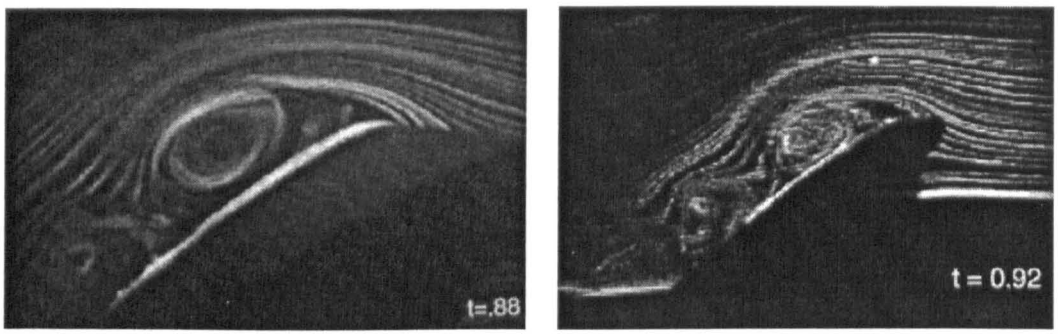

(a) Aerofoil NACA 0015 (b) Rectangular Wing, 57% span

Figure 3.2: Images of the dynamic stall vortex on a NACA 0015 aerofoil and at the mid-span of a rectangular wing with NACA 0015 cross-sectional profile. (From Laghezza [66])

This description suggests that the vortex initiation and development on the finite wing exhibits similarities with the two-dimensional case; albeit the three-dimensional flow over the wings is significantly more complicated than the two-dimensional flow over the aerofoil. Moreover, the flow visualization images 3.2.a and 3.2.b show that even after stall initiation, the general qualitative features of the stall process are common to both two- and three-dimensional flows. Lastly, the strong three-dimensional effects on the wing, especially near the mid-span of the wing, begin only after the onset of the vortex and an initial uniform growth along the wing span. All this suggests that a two-dimensional analysis at each span location would be sufficient to detect vortex inception. This hypothesis is assumed in the following analysis.

It is accepted that this approximation may be inappropriate at span sections closer (eg. 97% span) to the wing-tip where the presence of the tip-vortex could affect the onset of the dynamic stall vortex. Since there are no known studies of this in the literature a two-dimensional assumption will be used to examine vortex initiation across the span in this study. The limitations arising from this hypothesis will be highlighted along the way.

Chapter 4

Dynamic Stall Behaviour on the Rectangular Wing Planform

4.1 Introduction

The flow visualization tests on a nominally two-dimensional NACA 0015 aerofoil, Figure 2.3, whose geometrical characteristics are outlined in Table 3.2, showed that the onset of the vortex near the leading edge and its initial growth is qualitatively similar to the behaviour of the vortex at the mid-span, Figure 2.4, of the finite rectangular wing, Table 3.1. An exhaustive analysis of the chordal pressure distribution at defined span cross-sections can provide more details on the manner in which the flow behaves during dynamic stall. Moreover, a comparative study of the sectional normal force coefficient on the rectangular wing with the normal force coefficient of the NACA 0015 aerofoil will highlight further information in terms of severity of the stall.

4.2 Pressure Distribution Analysis

The development of the chordwise pressure distribution on the upper surface of the nominally two-dimensional NACA 0015 aerofoil during ramp-up motion at a reduced pitch rate of 0.022 is shown in Figure 4.1 together with the corresponding variation of geometric incidence with time. Although the following description refers to this specific test case, it is applicable to any ramp-up test for moderate pitch rates. This is because it has become apparent through the present study that the pitch rate mainly affects the timing of the events and not the general features of the flow field behaviour.

In Figure 4.1 a strong leading edge suction peak appears, due to the presence of the accelerating fluid stream flowing over the nose from the stagnation point on the pressure side to the suction side of the aerofoil surface. The suction peak is followed by a strong adverse pressure gradient. From the flow visualization [66], [100] and Appendix B, it is known that eventually a reversing flow develops downstream of the nose in the leading edge region. Under the influence of the adverse pressure gradient, the local reversing flow is accelerated rapidly towards the aerofoil nose. Thus, the reversing particles quickly approach and interact with the flow particles coming from the pressure side of the aerofoil surface. The collision leads to an enhancement in the local vorticity and the emergence of the dynamic stall vortex (see Chapter 6, section 6.2.3). Once formed, the dynamic stall vortex continues to grow giving rise to an increase in suction near the leading edge. When the dynamic stall vortex begins to move down the chord towards the trailing edge the suction peak does not collapse immediately but, rather, it continues to rise for a short time before dropping. The movement of the dynamic stall vortex causes a local distortion of the temporal chordwise pressure distribution. In fact, its movement creates a suction

wave that moves from the leading edge region towards the trailing edge.

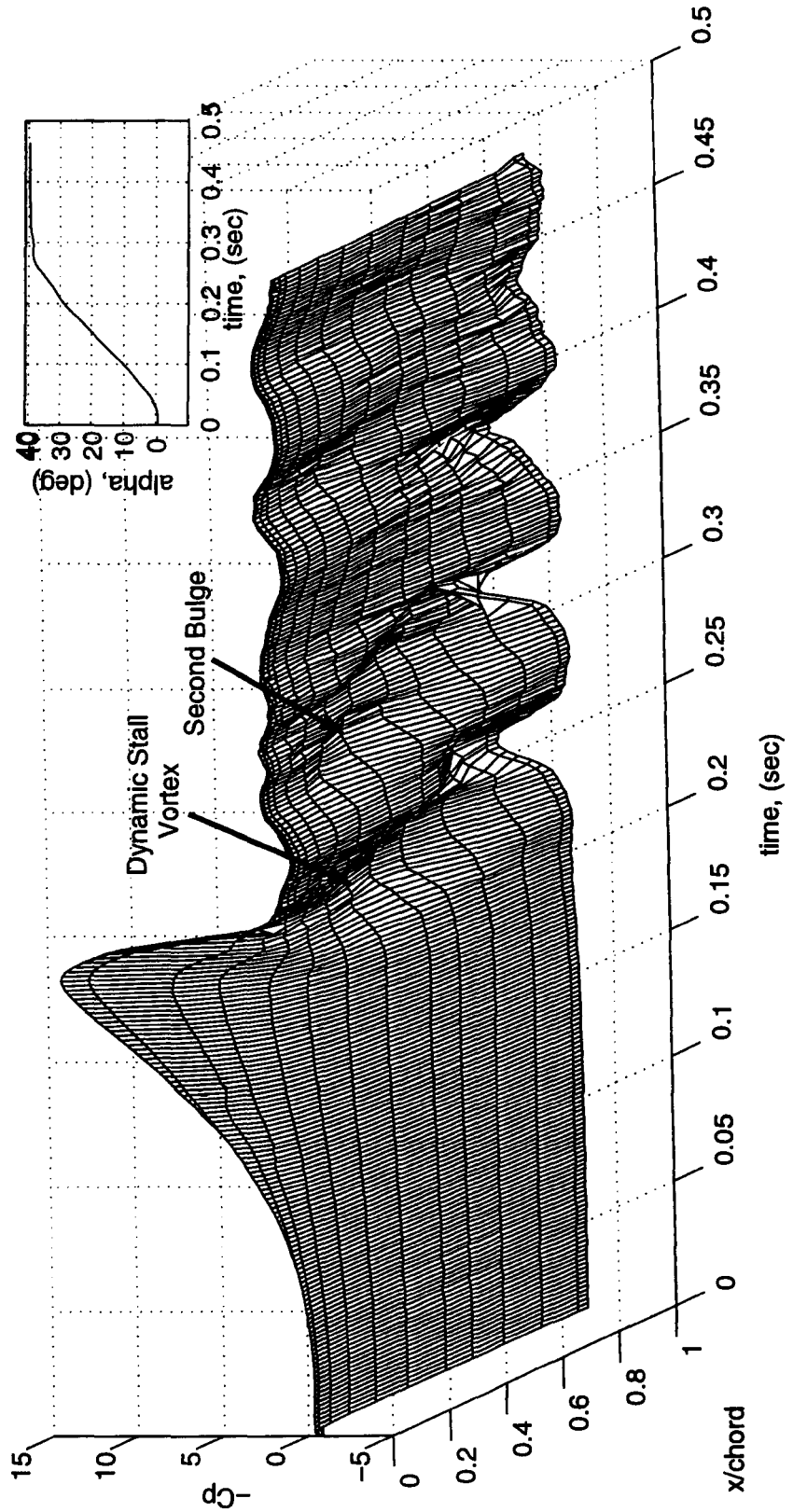

Figure 4.1: Time history of unsteady Cp chordal distribution over nominally two-dimensional NACA 0015 aerofoil at reduced pitch rate 0.022.

The corresponding graph of the chordwise pressure distribution at the 57% of span location on the finite rectangular wing is shown in Figure 4.2. As for the case of the nominally two-dimensional NACA 0015 aerofoil, the pressure distribution is characterized by the rise of leading edge suction as the incidence increases. The characteristic suction bulge associated with the dynamic stall vortex first appears closer to the leading edge than in the previous case of the nominally two-dimensional NACA 0015 aerofoil. Moreover, shortly after the dynamic stall vortex passes the trailing edge, a second bulge appears near the half chord. At 57%, 68%, Figures 4.2 4.3 and, less visible, at 80% of the span, Figure 4.4, this second bulge occurs at about the same time, 0.2 seconds. A similar bulge appears also on the nominally two-dimensional NACA 0015 aerofoil pressure plot Figure 4.1 and it rises at about 0.27 seconds. It is interesting to note that at these times, after the end of the ramp motion, there is a sudden drop in the incidence. Finally, this pressure bulge moves down the chord.

The behaviour of the chordal pressure distributions at span positions nearer to the wing-tip, 80% and 90% of span (Figures 4.4 and 4.5) is characterized by the same features as at the more inboard 57% of span cross-section. In particular, the local bulge associated with the dynamic stall vortex appears again but this time at approximately one third of the chord rather than at the leading edge. It is also less discernible at 90% of span. From the flow visualization (see section 3.2) it is known that the dynamic stall vortex at outboard sections is weaker than at the mid-span. This would correspond to a smaller disturbance in the chordwise pressure distribution.

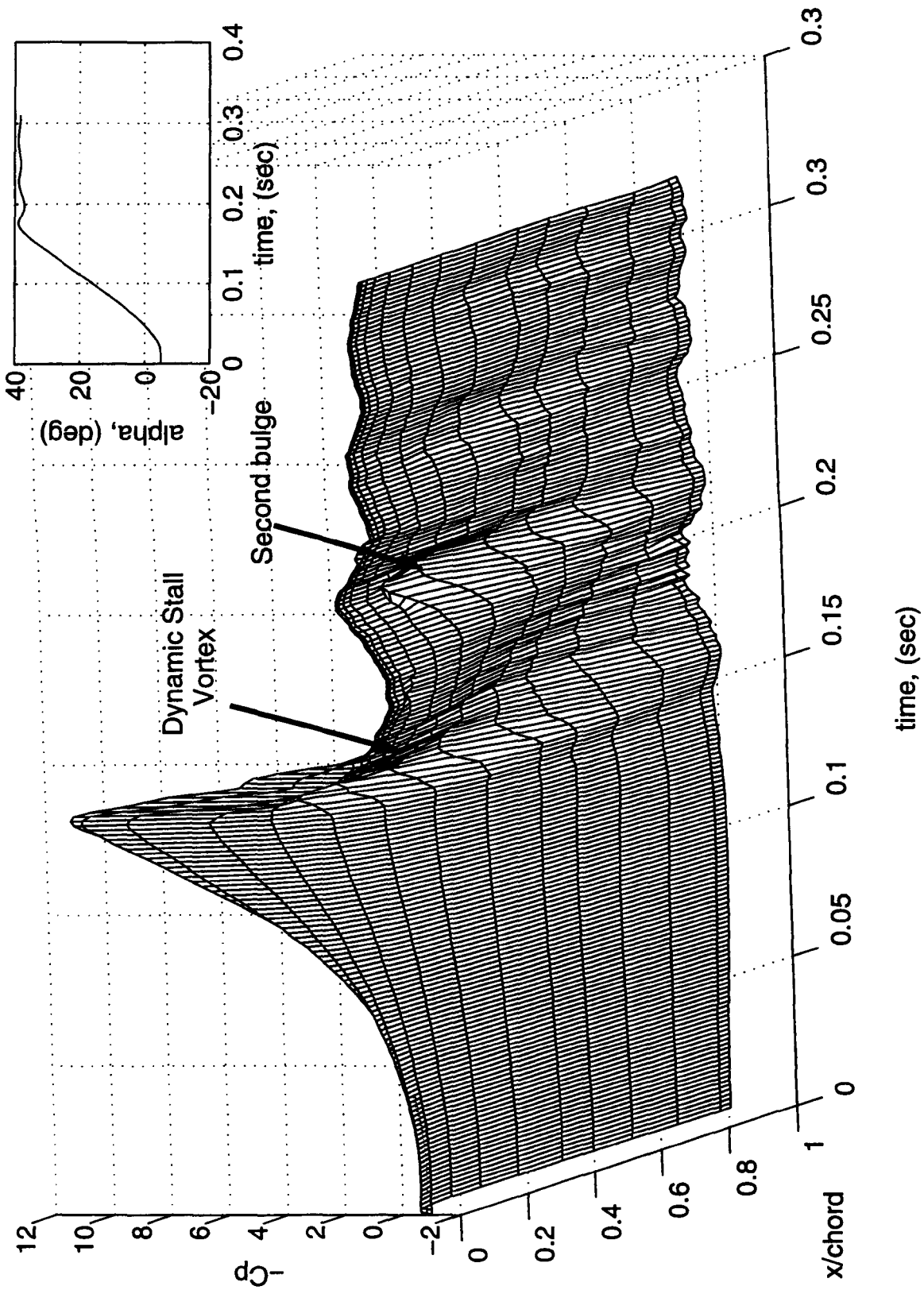

Figure 4.2: Time history of unsteady Cp chordal distribution at 57% of span of the rectangular wing at reduced pitch rate 0.022.

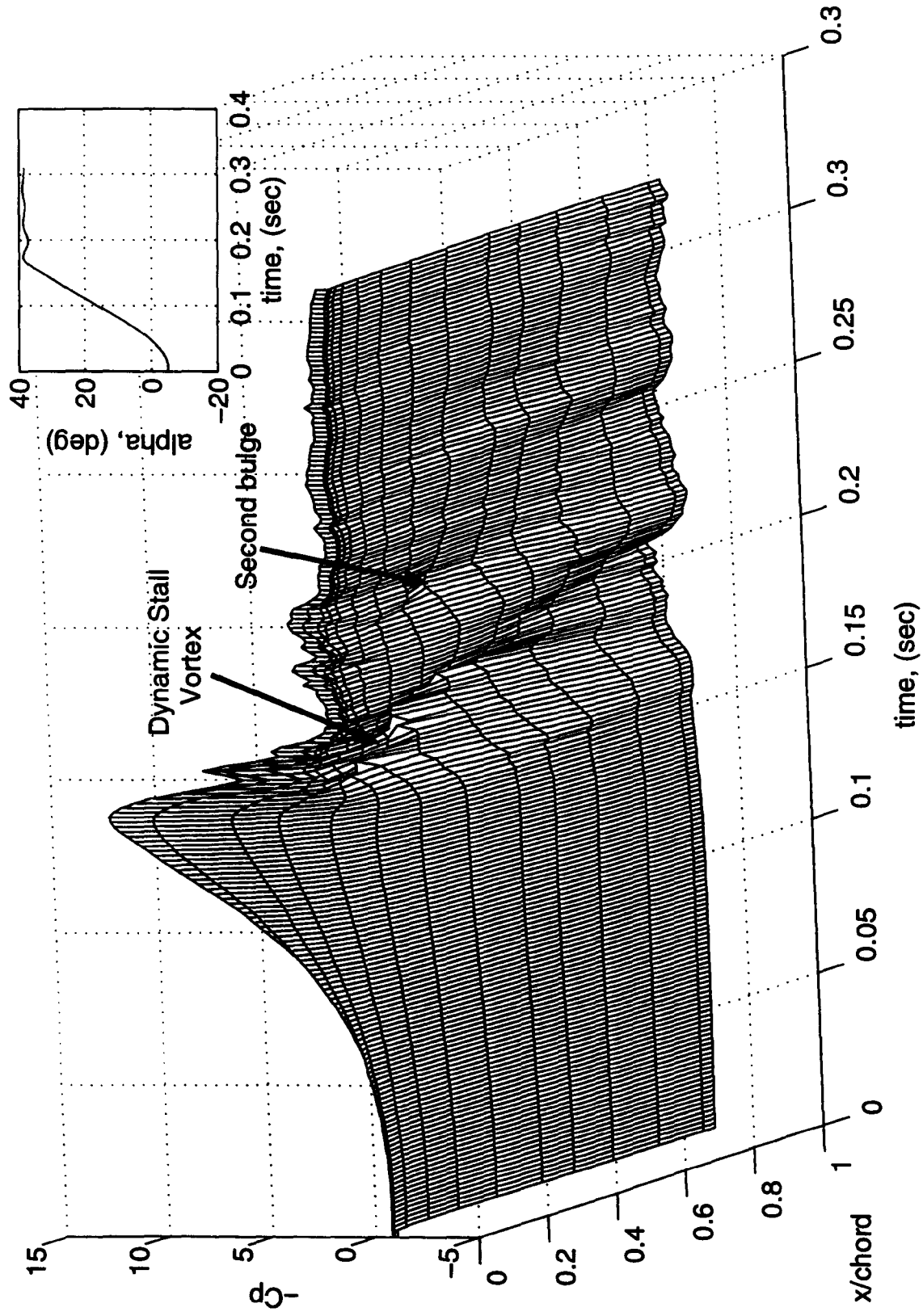

Figure 4.3: Time history of unsteady Cp chordal distribution at 68% of span of the rectangular wing at reduced pitch rate 0.022.

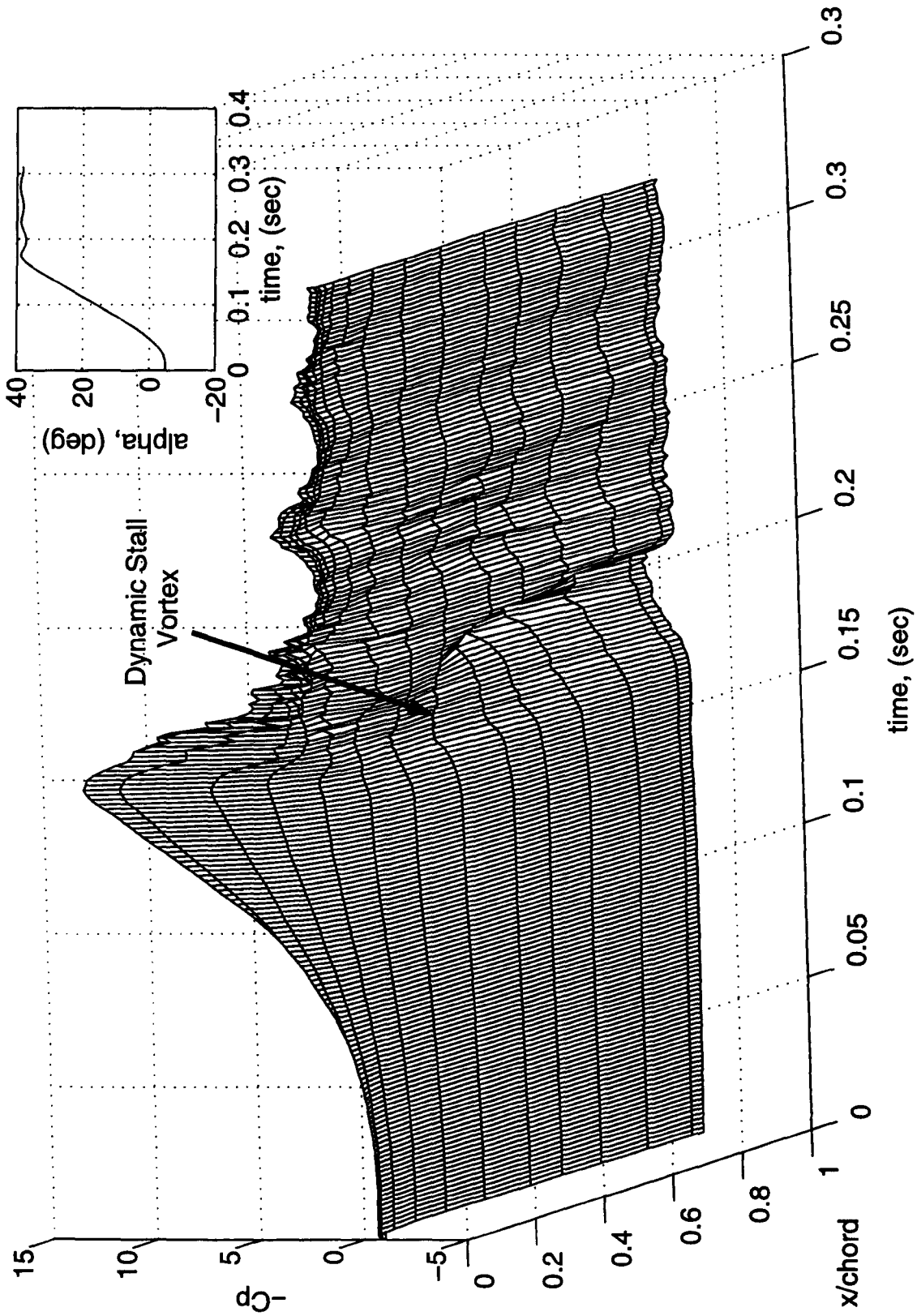

Figure 4.4: Time history of unsteady Cp chordal distribution at 80% of span of the rectangular wing at reduced pitch rate 0.022.

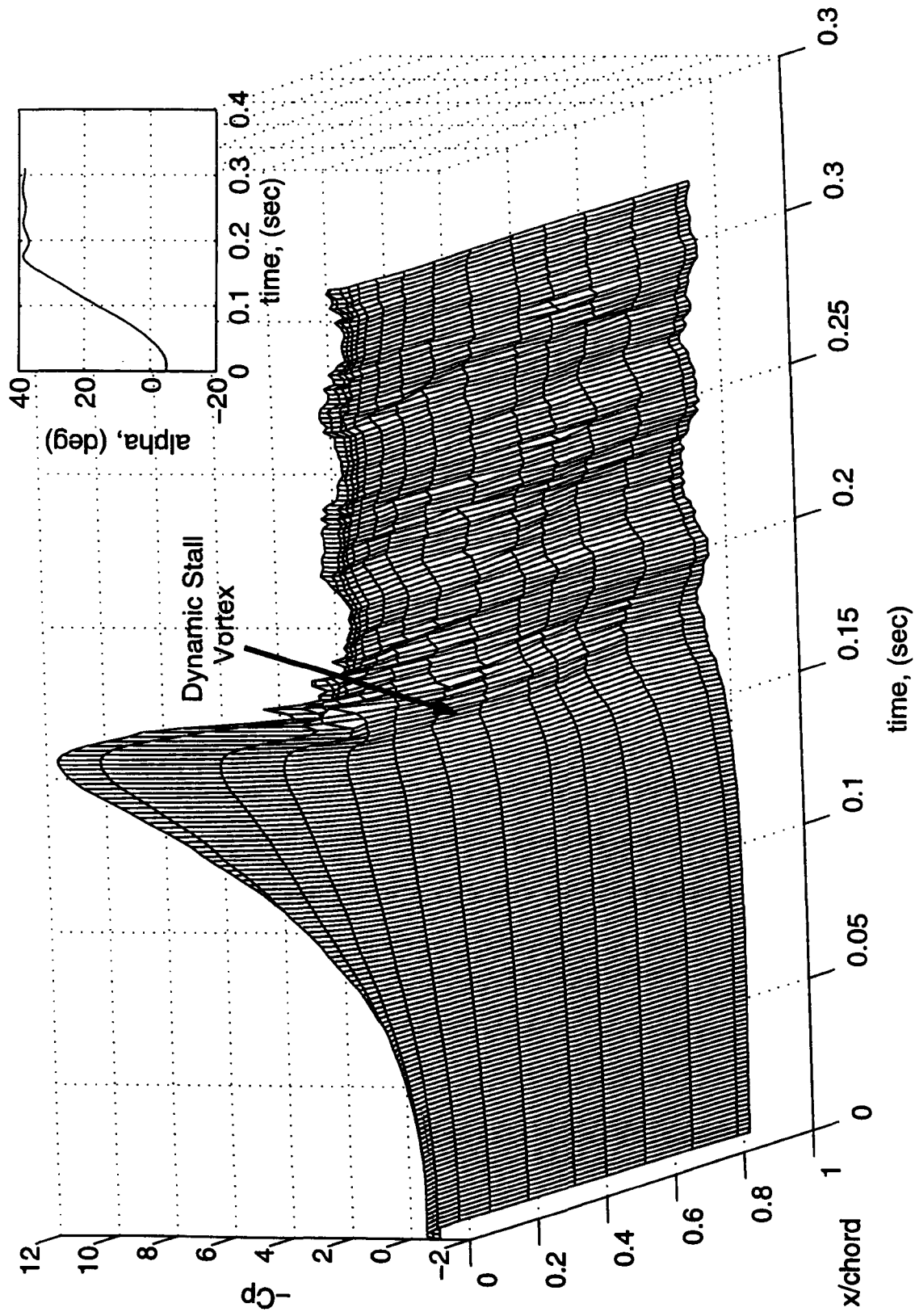

Figure 4.5: Time history of unsteady Cp chordal distribution at 90% of span of the rectangular wing at reduced pitch rate 0.022.

From Figures 4.1, 4.2, 4.3, 4.4 and 4.5 it is evident that the suction bulge associated with the dynamic stall vortex appears on the finite wing at a higher incidence than on the aerofoil. This effect is presumably due to the influence of the wing tip vortices. Indeed, the tip vortices downstream of the wing induce a downward component of air velocity in the neighborhood of the wing. This downward component is commonly known as *downwash*. The downwash has two important effects on the finite wing. It creates induced drag and reduces the angle of attack that each section along the wing span effectively sees. In more detail, the effective incidence seen at a span section close to the wing tip where the downwash is stronger, is smaller than at the mid-span. Further, on wings with the same geometry the extent of the wing subject to strong downwash will depend mainly on the aspect ratio of the wing. For wings with low aspect ratio, such as the current test model, almost the entire wing surface exhibits signs of the downwash effect.

From the above analysis of the temporal chordwise pressure distribution at each of the span sections of the rectangular wing, it would be seen that analysis of vortex onset near the mid-span of the wing may reveal strong similarity with the nominally two-dimensional case. It is also likely, however, that there may be some significant differences.

4.3 Normal Force Analysis

Carr et al. in 'Analysis of the Development of the Dynamic Stall Based on Oscillation Airfoil Experiments' [10] showed that the normal force coefficient curve exhibits signs of the events associated with the dynamic stall phenomenon. Carr and his co-workers related the form of the curve of the normal force coefficient, CN versus angle of attack 'alpha' to the corresponding boundary layer behaviour for a dynamically stalling

aerofoil. In particular, Carr used the nominally two-dimensional NACA 0012 aerofoil oscillating in pitch as an example but his observation on the stall development can be extended to any aerofoil experiencing dynamic stall. Following his description, a generic example of the chronology of dynamic stall events in terms of CN versus α is shown in Figure 4.6.

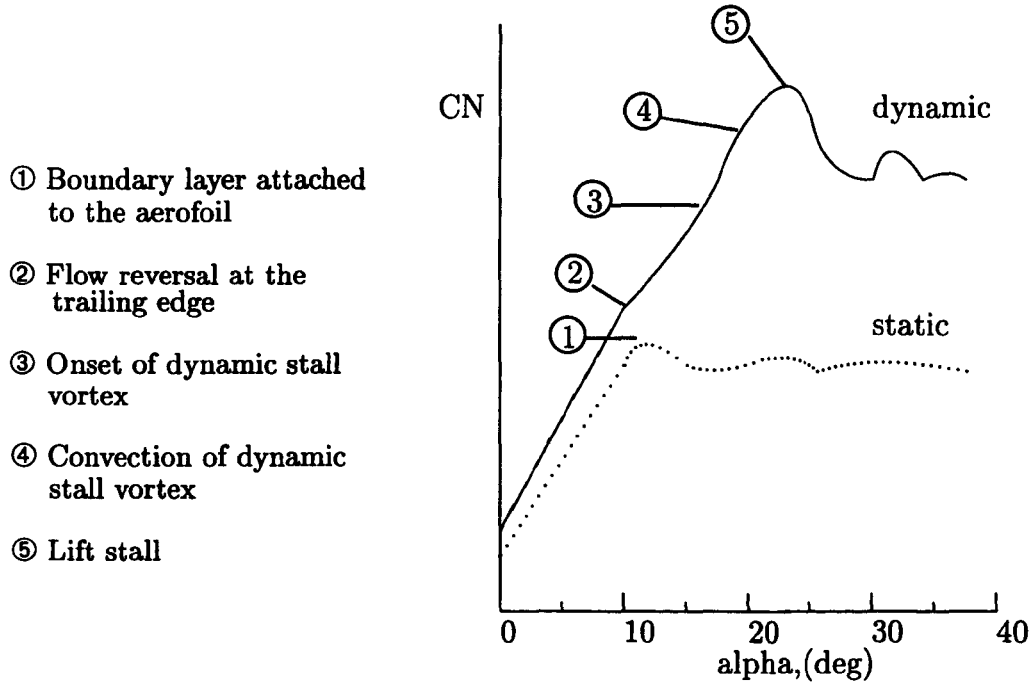

Figure 4.6: Build-up of normal force coefficient versus incidence during the events of dynamic stall. (Adapted from Carr et al. [10]).

The linear portion of the normal force coefficient curve is extended beyond the static stall angle, point ①. This behaviour corresponds to a boundary layer that stays thin and attached to the aerofoil surface. As the angle of attack increases, the first symptoms of flow reversal at the trailing edge of the aerofoil appear and the curve's linearity breaks, point ②. At the same time that the reversed flow moves up the aerofoil chord, the viscous flow at the leading edge region develops into a vortical

flow termed the dynamic stall vortex, at an angle that depends on many parameters, including aerofoil shape, pitch rate, frequency, Reynolds number and Mach number, as well as three-dimensional effects. This angle is approximately indicated by point ③. The dynamic stall vortex grows in size and intensity near the leading edge and is, in turn, responsible for the increase in the CN-alpha curve gradient. When the dynamic stall vortex moves down the aerofoil chord, it induces a further increase in the gradient of the curve, point ④. Finally, as the vortex progress downstream, CN suddenly drops producing the phenomenon known as 'lift stall', point ⑤.

This brief description illustrates the increase in peak CN versus alpha, due to the stall vortex developing above the aerofoil surface, and the delay in the stall with respect to the static case, as a result of the pitching motion. Therefore, the rate at which the model is pitched is a major factor in dynamic stall vortex formation and in the associated lift increment. Thus, it is to be expected that at very low reduced pitch rates the CN-alpha curve will be similar to the static case and the flow will exhibit the hallmarks of steady flow. This is confirmed by flow visualization tests at very low reduced pitch rates [66] that exhibit a flow with almost identical features to the static case. Under these conditions, it is said that the flow behaves quasi-statically. In the quasi-static regime, there is little evidence of dynamic stall vortex formation and a delay in the movement of trailing edge separation is the only observable factor which distinguishes the flow from the static case. For nominally two-dimensional flow, the upper limit of quasi-steady behaviour on the NACA 0015 aerofoil occurs at a reduced pitch rate of approximately 0.004, [66], [117]. This would place the lowest pitch rate case studied in the present work firmly in the quasi-steady domain. Following the above discussion, it may be expected that the CN-alpha curves will behave differently in fully dynamic cases. This observation is reinforced by Figure 4.7 which shows the normal force coefficient versus angle of

attack at two reduced pitch rates; one of which is below the quasi-steady boundary, reduced pitch rate 0.003, and one of which is well above the boundary, reduced pitch rate 0.027.

Further, it may be observed that in Figure 4.7a, the static response of the normal force coefficient of the nominally two-dimensional NACA 0015 aerofoil is higher than the dynamic response for a given angle of attack 'alpha' in the linear segment of the CN-alpha curve. Conversely, it happens that at the three span locations on the rectangular wing, the dynamic response in CN leads the static data. The explanation for this lies in the downwash caused by the shed vorticity and the vorticity associated with the tip vortices. These effects may explained as follows.

When an aerodynamic surface is subject to pitching motion the circulation about the surface changes during the pitching and, at the same time, a vortex, whose strength is equal in magnitude and opposite direction to that around the surface, is released from the edge of the surface in the downstream direction. The released vorticity is termed 'shed vorticity'. The shed vorticity acts to reduce the effective incidence experienced by the aerodynamic surface (downwash effect). In case of dynamic pitching, the circulation around the surface at a given geometric incidence 'alpha' is function of 'alpha' itself and also an induced incidence from the vortices shed at previous incidences and convected downstream with the local velocity without changing their strength. In case of static pitching, the downwash at a given incidence 'alpha' is negligible as any vorticity previously shed is assumed to have travelled infinitely far downstream. This would explain the lower values of the normal force coefficient CN in the linear segment of the dynamic curve, Figure 4.7a.

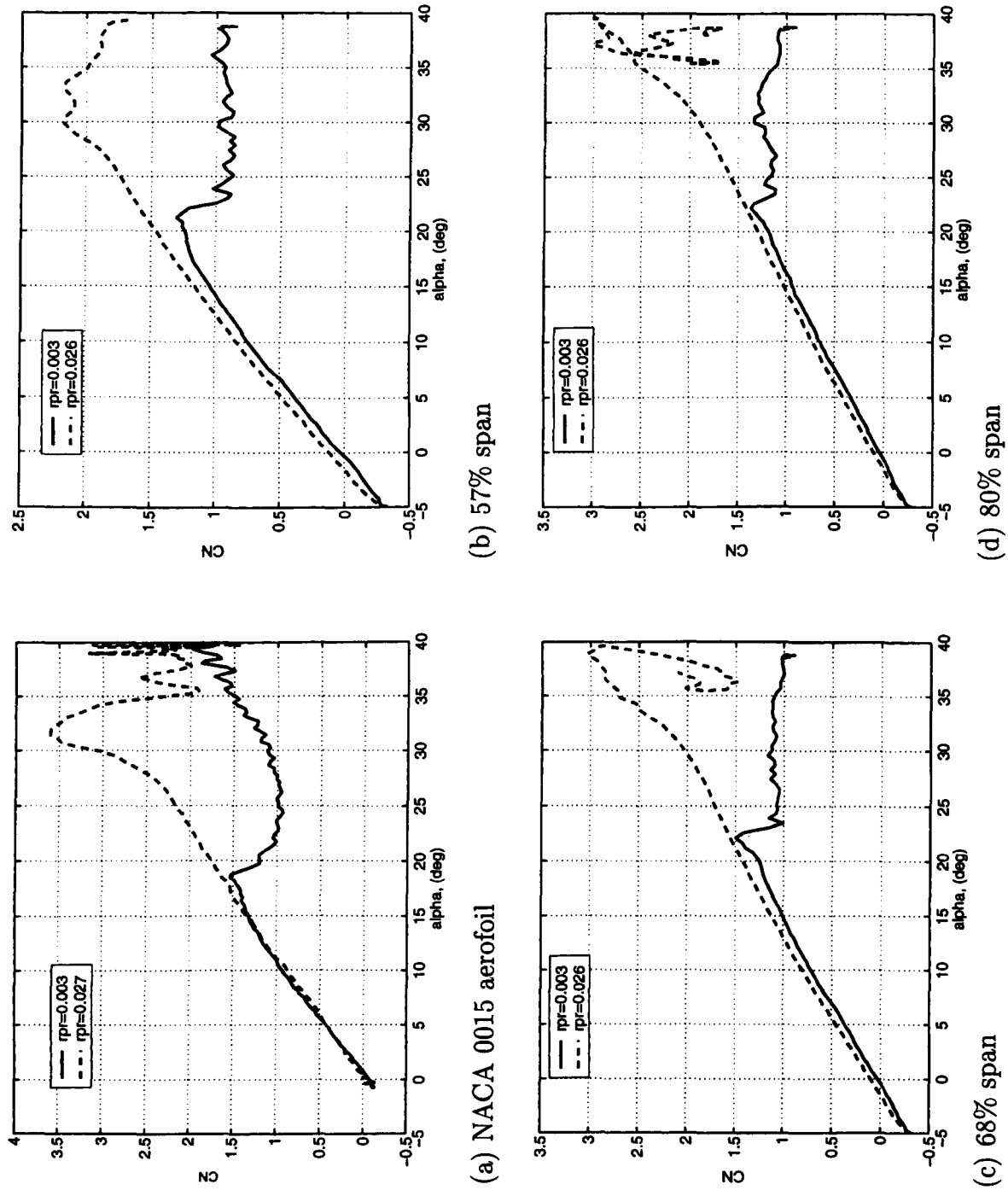

Figure 4.7: Normal force coefficients versus incidence in the quasi-steady domain at reduced pitch rate 0.003.

It would be expected that the shed-vorticity from the rectangular wing would produce the same effect on the dynamic normal force coefficient. The experimental data, however, give a different response, Figures 4.7b, c, d and c. This is because additional vorticity contributes to the downwash over the three-dimensional surface. This is the vorticity associated with the tip-vortices. As the wing pitches-up, vortices are trailed from the wing tips. These vortices join those liberated at earlier incidences to form the tip vortices of the wing. Thus, at a given geometric incidence during pitch-up, downstream segments of the tip vortex structure are weaker than those close to the wing. In the static case, the strength of the tip-vortices is constant in the streamwise direction and is determined purely by the geometric incidence. Thus, at a given geometric incidence, the integrated downwash will be weaker in the pitching case than in the static case. It would, therefore, be expected that in the dynamic case the effective incidence experienced by the wing would be higher than that in the static case at a given geometric incidence. This would explain why the dynamic CN response leads the static CN response in Figures 4.7 b, c, d.

In Figure 4.8 curves of normal force coefficient for the nominally two-dimensional NACA 0015 aerofoil are compared with corresponding curves for three span cross-sections of the rectangular wing over a range of reduced pitch rates. These curves reveal the three-dimensional nature of the normal force behaviour across the wing span. The progressive increases in the gradient of the linear portion of the curves, the higher CN peaks and the delay in lift stall associated with increased reduced pitch rate are, however, common to both two- and three-dimensional cases. Nevertheless, in the two-dimensional case, beyond the linear portion of the normal force coefficient curves, there is a sharp increase in gradient prior to stall, whereas this effect is much reduced in the rectangular wing curves. The diverse behaviour of the curves relative to the rectangular wing illustrates that the three-dimensional effects of the wing

span have an impact on the growth and convection of the dynamic stall vortex. In particular, the gradient of the CN-alpha curves and the severity of the stall is reduced on the rectangular wing. Conversely the incidence of lift stall is increased. Also, at a given reduced pitch rate, the gradients of the curves differ at each of the three span sections and the stall does not occur at the same time. It is, therefore, clear that the stall process is not uniform along the wing span.

It can been concluded that an increase in the reduced pitch rate generally produces a higher peak CN and a delayed stall. It is interesting to note, however, that this increase is not monotonic. Indeed, in Figure 4.8 the CN peak values and their corresponding incidences are almost identical at the two highest reduced pitch rates.

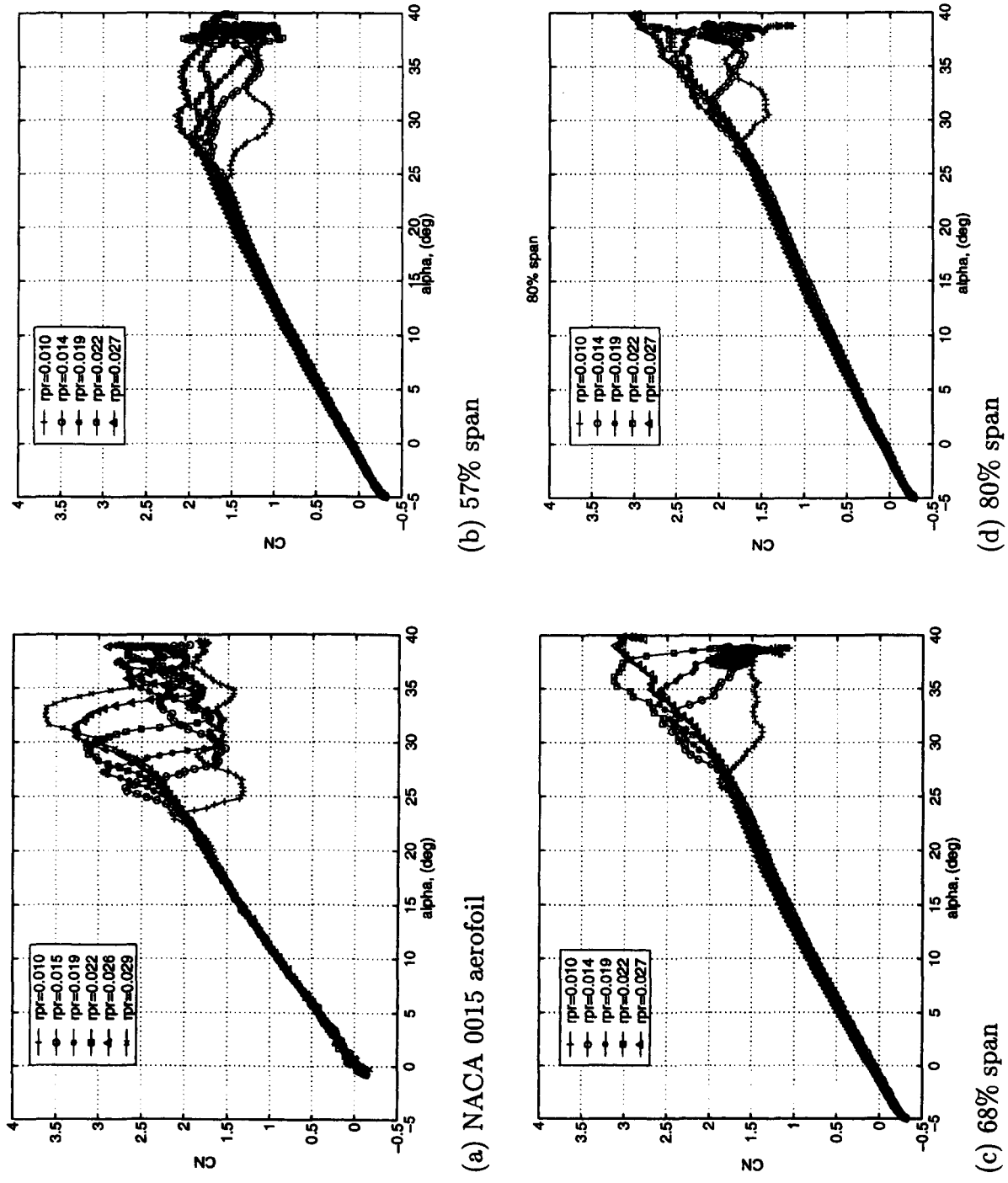

Figure 4.8: Normal force coefficients versus pitch incidences of the nominally two-dimensional NACA 0015 aerofoil and three cross-span sections of the rectangular wing with rounded tips for several reduced pitch rates.

Chapter 5

Dynamic Stall Behaviour on the 60^0 Swept-Tip Wing Planform

5.1 Unsteady Flow over the 60^0 Swept-Tip Wing

Information on the structure and behaviour of the unsteady flow field over the swept tip wing undergoing pitching motion has been provided by the flow visualization analysis. In particular, Moir and Coton [100] presented data for a pitching rectangular wing with 60^0 swept tips which was a scaled replica of the one used in the pressure measurement test described in Chapter 2. The relevant parameters for the test of Moir and Coton are given in Table 5.1.

Rectangular Wing	Section	Re_c	Chord, mm	Span, mm	AR
tip: 60^0 swept-tips	NACA 0015	13000	200	600	3.7

Table 5.1: Characteristics of the rectangular wing with 60^0 swept tips test case relative to the three-dimensional flow visualization experiments.

The 'swept-tip' wing was examined in laminar flow conditions at a chord Reynolds

number of approximately 13,000 during a ramp-up test at a reduced pitch rate of 0.08. As for the rectangular wing, the model was pitched around the quarter chord line from 0^0 to 40^0, and then held stationary until the flow developed and convected from the trailing edge. Flow visualization images from above and in front of the model are reported in Appendix D because they may benefit the reader to visualize the behaviour of the flow over the wing surface. An exhaustive flow topology analysis containing complete information regarding the technical aspects of the flow visualization can be found in reference [100].

The study of Moir and Coton showed that many of the features observed on the rectangular wing are present on the swept-tip wing. In particular, the unsteady flow field which evolves over the swept-tip wing undergoing ramp-up motion at a constant pitch rate, appears to be mainly governed by vortical structures similar to those observed on the rectangular wing, namely: dynamic stall vortex, shear layer vortex and wing tip-vortices. The formation and evolution of these vortices are characterized by the same sequence of events observed in section 3.2 for the rectangular wing undergoing ramp-up motion at constant pitch rate. The main characteristics of the flow behaviour can be outlined as follows.

The wing leading edge is dominated by the dynamic stall vortex that once formed, grows almost uniformly along the span. Because of the interaction with the wing tip-vortices, the dynamic stall vortex structure loses uniformity and turns into a vortex structure with the characteristic 'Omega' shape. The dynamic stall vortex moves downstream along the wing chord, reaches the trailing edge and leaves the wing surface.

One of the main features that emerged from comparison of the flow visualizations for the rectangular and swept-tip wings is the behaviour of the wing tip vortices in

the two cases. The tip-vortices on the swept-tip wing appear stronger and wider in extension [100], as shown in sketch Figure 5.1 or the flow visualization images in Figures D.2, D.3. It is, therefore,to be expected that the tip-vortices will affect the flow field on the swept-tip wing in a different manner than that tip-vortices on the rectangular wing.

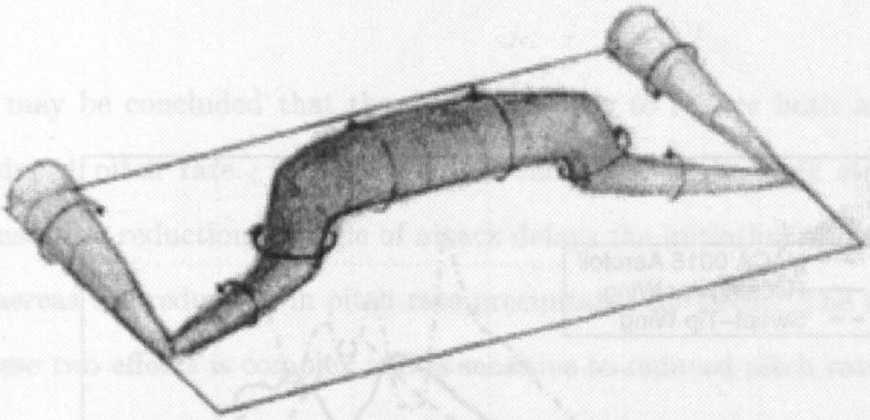

(a) Rectangular Wing

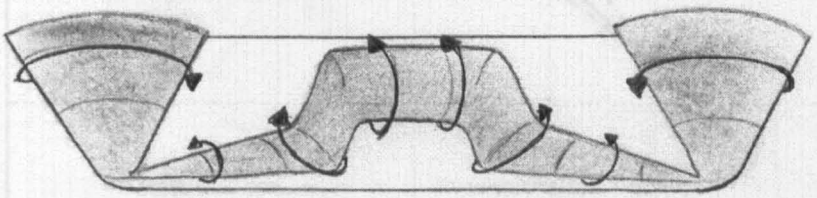

(b) Swept-Tips Wing

Figure 5.1: Vortex structure on Rectangular Wing and Swept-Tips Wing

This observation suggests that the downwash across the swept-tip wing is more pronounced and leads to effective flow incidences along the span lower than those on the rectangular wing at corresponding span-sections. The immediate consequence

of this is that the normal force of the swept-tip wing during the pitch at a given reduced pitch rate has lower values than that of the rectangular wing and the lift stall is delayed. This is well illustrated in Figure 5.2 where the gradient of the normal force coefficient curve of the swept-tip wing is lower than that of the rectangular wing and the CN-alpha curve reaches its maximum value at higher incidence before stalling.

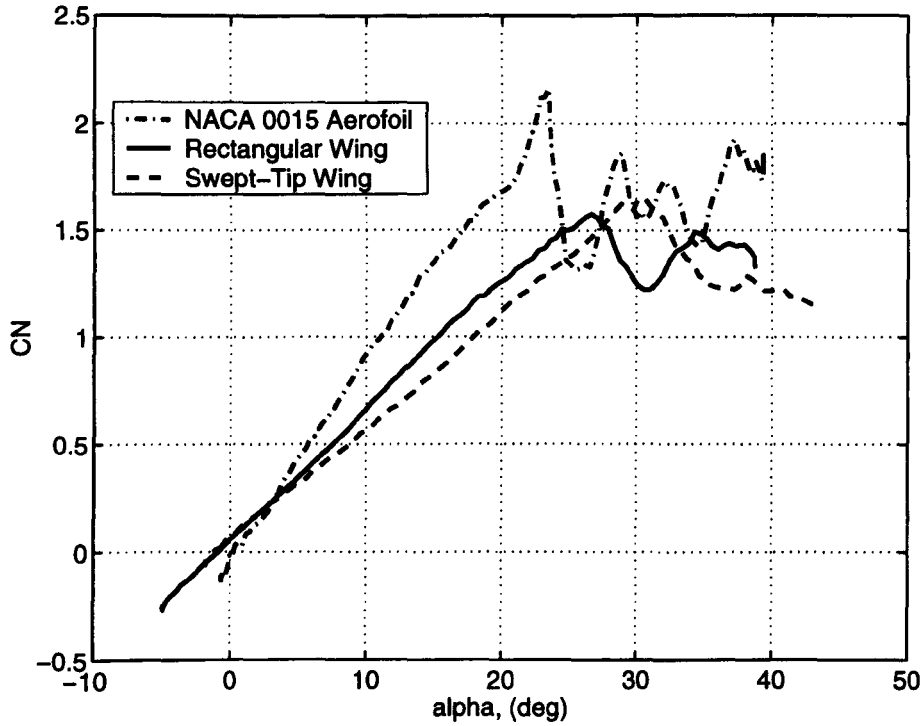

Figure 5.2: Normal force coefficient versus incidence for the nominally two-dimensional NACA 0015 aerofoil, the rectangular and the 60^0 swept-tip wings at reduced pitch rate 0.010.

The downwash will also affect the reduced pitch rate that is a function of the angle of attack (rpr $= \dot{\alpha}c/2U_\infty$). The implication of this is that a given geometric reduced

pitch rate corresponds an effective reduced pitch rate that is different on each wing and, in particular, is lower on the swept-tip wing. Dynamic stall events are sensitive to the pitch rate (see Chapter 4), and in particular the inception of dynamic stall events is delayed at high pitch rates, Figure 5.3. This is not the case in Figure 5.3 but, does occur at the higher reduced pitch rate of 0.026 as shown in Figure 5.4. In this case the normal force coefficient curves for both wings have almost the same gradient but the rectangular wing stall later.

It may be concluded that the downwash acts to reduce both angle of attack and reduced pitch rate. These affect the inception of dynamic stall in the opposite sense: the reduction in angle of attack delays the initiation of dynamic stall events, whereas the reduction in pitch rate precipitates the event. The combined action of these two effects is complex and is sensitive to reduced pitch rate.

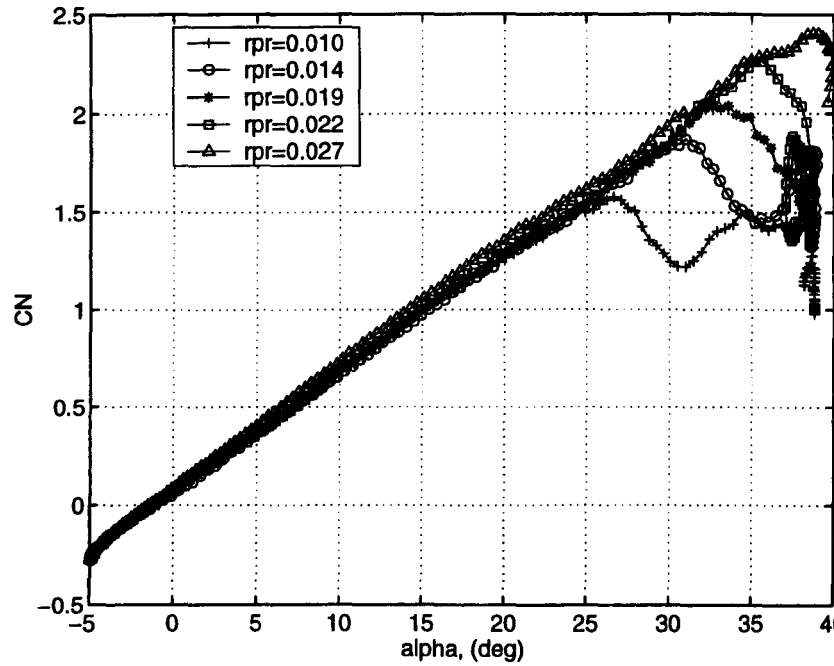

(a) rectangular wing

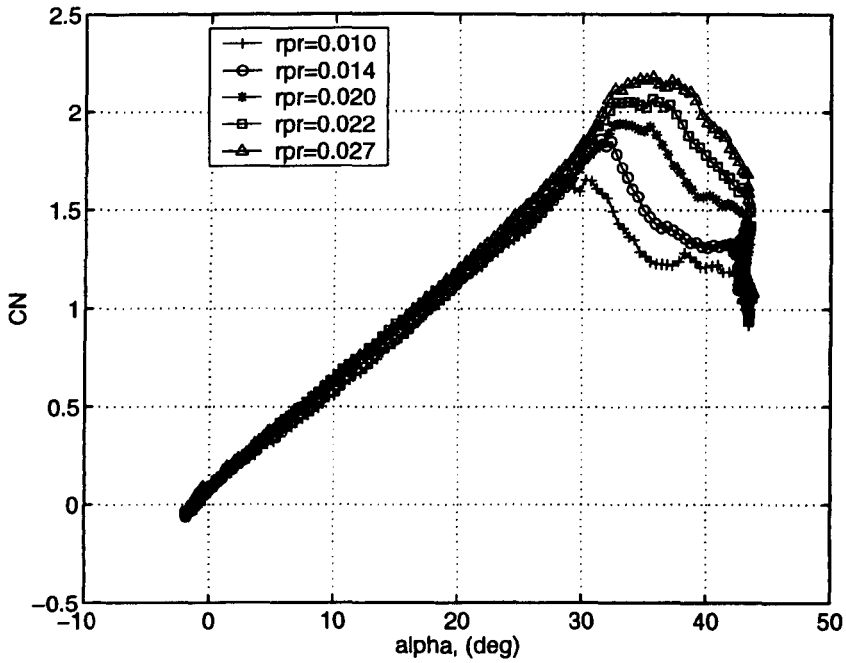

(b) swept-tip wing

Figure 5.3: Normal force coefficient versus incidence for the rectangular and the 60^0 swept-tip wings for a number of reduced pitch rates.

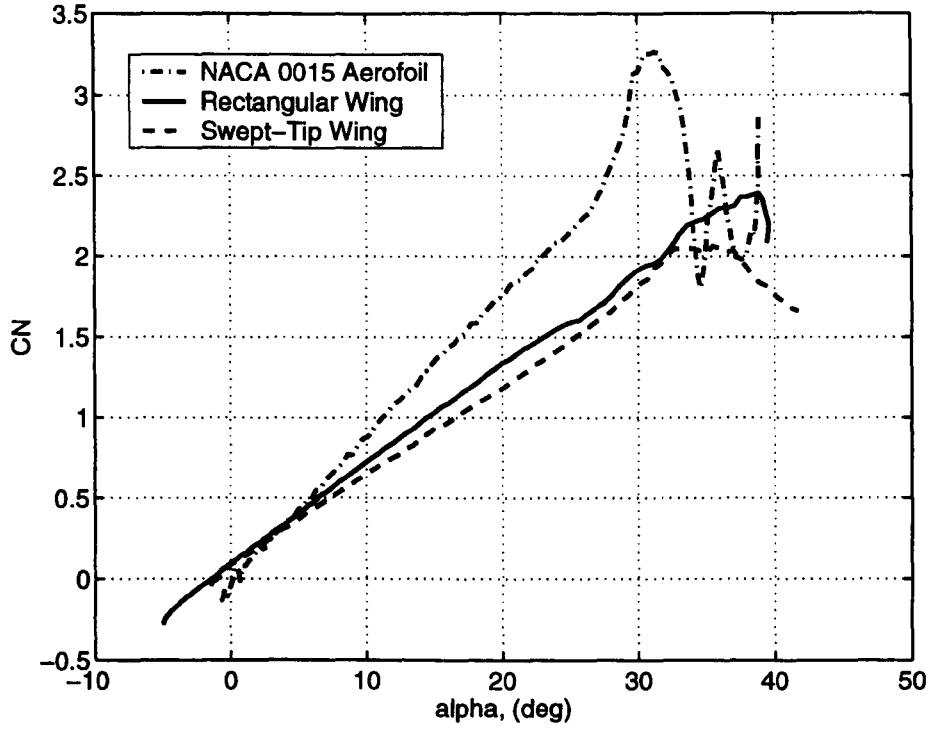

Figure 5.4: Normal force coeffcient versus pitch-incidence for the nominally two-dimensional NACA 0015 aerofoil, the rectangular and the 60^0 swept-tip wings at reduced pitch rate 0.026.

Chapter 6

Vorticity and Its Development

6.1 Introduction

Flow visualization, pressure distributions and normal force coefficient analysis have provided information on the general flow behaviour and have provided insight into the entire dynamic stall process. In particular, flow visualization demonstrated the behaviour of the three-dimensional dynamic stall vortex over the pitching wing. The chordwise pressure distributions and the corresponding normal force coefficients provided further information on the vortex behaviour at local span sections and on the intensity of the dynamic stall process as a function of the reduced pitch rate. Unfortunately, however, these methods do not provide a complete description of the physical mechanisms responsible for the initiation, development, growth, movement and detachment of the dynamic stall vortex. For many years the physical process that triggers the onset of the dynamic stall vortex and the mechanisms responsible for the growth and convection of the vortex have been of interest to many researchers who have attempted to understand these events through experimental tests and numerical computations. The results of these studies have been described in a number of review articles such as the publications of Shih et al. [120] and Ghia et al. [44],

[43] who carried out numerical simulations of the flow produced around a pitching aerofoil for moderate Reynolds number ($O(10^3)$). The most documented case is relative to the computation of the flow by pitching aerofoils for higher Reynolds number ($O(10^4)$). In fact, a number of works are provided by Visbal and Shang [126], Osswald et al. [103], Knight and Ghosh [65]. Despite this intense interest in the phenomenon, there is still an incomplete understanding of the physics of the dynamic stall process.

The aim of the following work is to develop a deeper understanding of the physical phenomenon that leads to the formation of the dynamic stall vortex. The approach adopted is to examine the evolution of the vorticity on the wing surface, because, as suggested by Elliot et al. [22], and later by Cowley et al. [19], the formation of a vortex is anticipated by a local concentration of the vorticity field which stimulates the flow to roll-up into a vortex formation. This idea, in conjunction with the idea of Lighthill [76] that a solid boundary wall can be seen as a distribution of sources and sinks of vorticity, suggests that the whole dynamic stall process and the related sequence of events are effected by the vorticity generated by the sources spread along the wall. In the following study the onset of the dynamic stall vortex is investigated by examining the vorticity leaving the surface of the wing by the diffusion mechanism and the process by which the local concentration of vorticity at the leading edge is channelled into the dynamic-stall vortex.

At this stage, it is useful to review briefly the classical theory of vorticity. The first part of this chapter provides basic theoretical notions of vorticity and its variation that will help in the subsequent investigation and understanding of the influence of vorticity in dynamic stall events. This is followed by an analysis of the evolution of the vorticity over the rectangular wing and the nominally two-dimensional

NACA 0015 aerofoil during pitching motion.

6.2 Vorticity

6.2.1 Generation and Spreading of Vorticity

The classical definition of Cauchy and Stokes defines 'vorticity' as the angular velocity of a fluid at a point in the flow. This is represented mathematically by the curl of the velocity:

$$\boldsymbol{\omega} = curl\boldsymbol{v} = \left(\frac{\partial v_z}{\partial y} - \frac{\partial v_y}{\partial z}, \frac{\partial v_x}{\partial z} - \frac{\partial v_z}{\partial x}, \frac{\partial v_y}{\partial x} - \frac{\partial v_x}{\partial y}\right) \tag{6.1}$$

This expression says that if $\boldsymbol{v}$ is the velocity of a spherical particle of fluid, the vorticity at any point in a fluid flow is proportional to the instantaneous angular momentum of the particle centered on the point, [76]. The meaning of the components of (6.1) are illustrated in Figure 6.1 which shows that the term $\frac{\partial v_z}{\partial y}$ produces an angular momentum $\frac{1}{2}I\frac{\partial v_z}{\partial y}$ about the x-axis, where I is the sphere's moment of inertia.

Before speaking about the properties of vorticity, it is useful to introduce first a few definitions.

Many of the concepts associated with the velocity field may be applied in the vorticity field. Indeed, the equivalent idea of a streamline in the vorticity field is the vorticity line defined as a line everywhere tangent to the vorticity vectors. Similarly, just as a stream-tube is a tubular region within the fluid bounded by streamlines, a bundle of vorticity lines is called vortex tube.

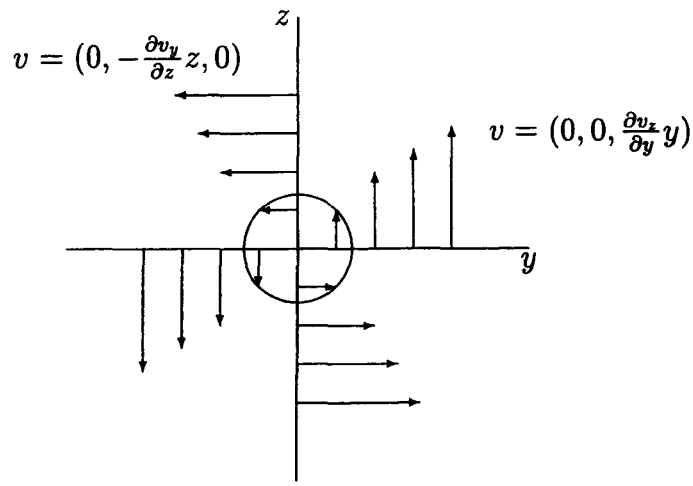

Figure 6.1: Angular momentum in the x plane of a spherical particle of fluid. (Adapted from Lighthill [76]).

As shown in Equation. (6.1) the vorticity vector is the curl of the velocity and, from this, it follows that the divergence of the vorticity vector is zero, Equation. (6.2). This condition is well known as the solenoidality condition whose physical implication is that the magnitude of the vorticity varies along any vortex tube inversely as the cross-sectional area. The consequences of the solenoidality condition are quite important and they will be discussed shortly.

$$\nabla \cdot \boldsymbol{\omega} = \frac{\partial \omega_x}{\partial x} + \frac{\partial \omega_y}{\partial y} + \frac{\partial \omega_z}{\partial z} = 0 \tag{6.2}$$

From the no-slip condition ($U_{wall} \times \boldsymbol{n} = U_{fluid} \times \boldsymbol{n}$) that imposes zero relative tangential velocity between a rigid wall and the fluid immediately next to it, it follows that the vorticity components at any point on a flat wall that lies in the xz plane, with y as the normal direction, characterize themselves as follows.

$$\begin{aligned} \omega_x &= \frac{\partial v_z}{\partial y} - \frac{\partial v_y}{\partial z} = \frac{\partial v_z}{\partial y} \\ \omega_y &= \frac{\partial v_x}{\partial z} - \frac{\partial v_z}{\partial x} = 0 \\ \omega_z &= \frac{\partial v_y}{\partial x} - \frac{\partial v_x}{\partial y} = -\frac{\partial v_x}{\partial y} \end{aligned} \tag{6.3}$$

Equation (6.3) says that the vorticity component perpendicular to the wall is zero. Moreover, it can be easily shown that the wall vortex lines are perpendicular to the wall streamlines. Therefore, it may be concluded that the vorticity vector is perpendicular to the stream-wise direction and parallel to the wall, (Panton [105]). The wall is assumed flat for simplicity, but this result is also valid for curved surfaces.

The Equation governing the vorticity field over a surface moving with an arbitrary velocity is derived from the Navier-Stokes Equations. The vorticity Equation provides a key to understand the evolution of the vorticity field. Indeed, from the vorticity Equation it emerges that the vorticity field evolves under three dynamic actions: convection, diffusion and deformation of vortex lines, (see Appendix C.2). The processes of convection and diffusion interplay in the spread of vorticity through the flow field by 'transporting' the angular momentum of the fluid particles through two different mechanisms. The *convection* process transports the momentum of the fluid particles by moving the fluid itself. Because the convection of vorticity has the property that vorticity is preserved on a particle path, the *diffusion* process takes care of transferring the vorticity to neighboring paths through an exchange of momentum among the fluid particles.

The transport of vorticity in the manner explained above is analogous to that of heat flow. On comparing the transfer of momentum with that of heat it may be pointed out that, in a flow along the wall, the temperature changes in accordance with the same law of the velocity (momentum) propagation. On the other hand,

the propagation of temperature through the flow corresponds to the propagation of vorticity in the flow.

Turning to diffusion and convection of vorticity, the forces that cause these two processes are the viscous and inertial forces and the ratio of inertial force to viscous force is called the Reynolds number. It may be said that the Reynolds number provides an index of how the diffusion and the convection process interplay their roles in the mechanism of transporting the vorticity through the flow. For example, in the limiting case of the Reynolds number equal to zero (viscosity forces dominate) the vorticity spreads only through diffusion. At very high Reynolds numbers, the inertial forces mainly take care of carrying the vorticity downstream through the flow field. A picture of how the inertial and viscous forces act to spread the vorticity is given by the traditional example of the flow around a sphere, Figure 6.2a. When the viscosity forces dominate, the equivorticity lines are symmetric about a vertical plane perpendicular to the flow through the sphere, Figure 6.2b. With increasing Reynolds number, diffusion and convection interplay in such a way that, as a result, the equivorticity lines exhibit an asymmetric pattern, Figure 6.2c. At higher Reynolds number, a wake would form behind the sphere because of a new phenomenon: the flow instability. Flow instability will be dealt with separately in a later section.

In addition to the two mechanisms of diffusion and convection there is also the mechanism of deformation of an uniform vortex tube. The stretching of a uniform vortex tube increases the 'magnitude' of the vorticity whereas contraction of the tube has the opposite effect. On the other hand, the deformation due to any turning or angular deformation of an uniform vortex tube does not affect the magnitude of the vorticity, (Panton [105]). It should be noted, at this point, that a change in the *magnitude* of the vorticity does not require a change in the *strength* of the uniform vortex tube. This concept may be easily understood by the analogy with the flow

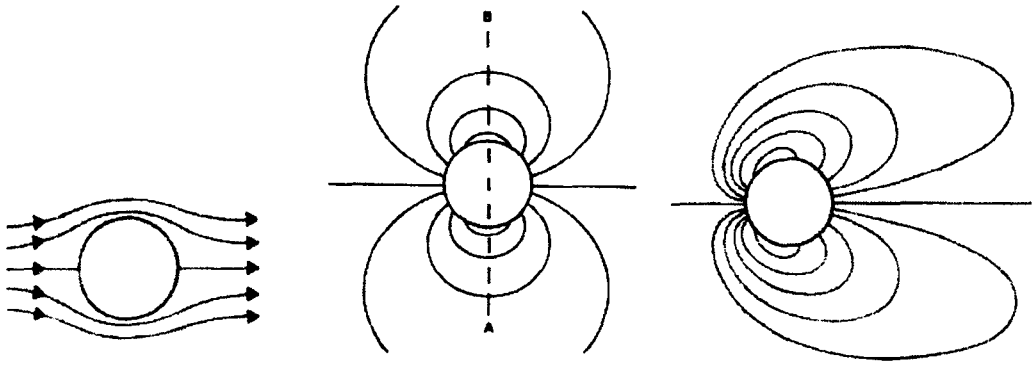

(a) Stream-lines (b) Equivorticity-lines $Re = \frac{DV}{\nu} = 0.$ (c) Equivorticity-lines $Re = \frac{DV}{\nu} = 5.$

Figure 6.2: Streamlines and equivorticity lines around a sphere at three Reynolds number. (Adapted from Jenson [59]).

of water passing through a pipeline. If the cross-section of the pipe diminishes, the velocity of water must increase, since the mass flow rate through all cross-sections of the pipe must be the same according to the conservation law. With respect to the solenoidality condition, vorticity behaves in the same way. If the vortex tube narrows, the vorticity must increase. This concept is expressed by Helmholtz in his first theorem that asserts that in a real flow the strength of vorticity in an uniform vortex tube is the same at all cross-sections.

Helmholtz also formulated a second theorem which states that vorticity in a flow can neither be generated nor destroyed. This theorem was formulated for ideal flow or rather for a flow where viscous effects are neglected. The immediate consequence of this theorem is that fluid particles carry vorticity without either losing or acquiring new vorticity. In a real flow this assumption no longer holds since the diffusion mechanism can transfer vorticity from one particle to another. Moreover, since

diffusion cannot create vorticity, then it raises the question as to how a body moving through an undisturbed real flow is responsible for development of the vorticity around it. The answer is given by Lighthill [76] who suggested that any wall can be seen as a distribution of sources and sinks of vorticity in a manner analogous to the simulation of a solid boundary as a distributed source of heat in heat transfer theory.

6.2.2 Production of Vorticity at Wall

It may be asserted that the mechanism that generates the vorticity on the wall is due to unbalanced viscous forces that rotate the fluid particles. The relationship between the viscous forces and vorticity was expressed by Panton [105] as follows:

$$F_{viscous} = \boldsymbol{n} \cdot \boldsymbol{\tau} = -\mu \boldsymbol{n} \times \boldsymbol{\omega} \tag{6.4}$$

The wall vorticity is directly proportional to the wall shear stress; when the wall shear is high, the vorticity is large. Equation (6.4) expresses the production of vorticity as a function of the viscous force but does not indicate how much vorticity is entering the flow. Once again, however, the heat transfer theory analogy may be used such that the vorticity entering the flow is given by the flux of vorticity across a plane normal to the vorticity vector on the wall. Following Fourier's heat conduction law, this is mathematically defined by Panton as:

$$\boldsymbol{S_{flux}} = -\nu \boldsymbol{n} \cdot \bigtriangledown \boldsymbol{\omega} \tag{6.5}$$

The vector $\boldsymbol{S_{flux}}$ is the flux of vorticity across a plane with unit normal vector $\boldsymbol{n}$ toward the fluid. Lyman [84] pointed out that the analogy to Fourier's law, used to develop Equation(6.5) may not be exact in three dimensional flows. As a consequence, the use of Equation (6.5) to estimate the flux of vorticity may incur

some errors. Lyman proposed the following alternative definition

$$\boldsymbol{S} = \nu \boldsymbol{n} \times (\nabla \times \boldsymbol{\omega}) \tag{6.6}$$

Equations (6.5) and (6.6) express the rate of vorticity production per unit area of surface. Although both give the same result when integrated over a closed control surface as shown by Lyman and Panton [84], [105] they are not equivalent. This is easily seen by examining their components at a solid surface. However, Equation(6.6) should be considered when it is of interest to examine the local components of the vorticity flux across a three-dimensional surface.

Neither Equations (6.5) and (6.6) provide any information on the relation between the flux of the vorticity and other flow variables such as pressure, temperature etc. Because of this, Panton, using the momentum Equation evaluated on a stationary wall, showed that the components of the vorticity flux are directly related to the pressure gradient from the wall into the fluid:

$$-\mu \frac{\partial \omega_z}{\partial y} = \frac{\partial p}{\partial x} \tag{6.7}$$

$$\mu \frac{\partial \omega_x}{\partial y} = \frac{\partial p}{\partial z} \tag{6.8}$$

These relations quantify the flux of vorticity from the wall. The third flux of vorticity across the wall is provided by the solenoidality condition at the wall. In fact, although ω_y is zero at the wall, there may be a flux of vorticity due to this component of vorticity, [105]:

$$-\frac{\partial \omega_y}{\partial y} = \frac{\partial \omega_x}{\partial x} + \frac{\partial \omega_z}{\partial z} \tag{6.9}$$

Equations (6.7)-(6.9) do not include the effects of the acceleration of a wall in motion. This raises the question as to whether the acceleration of the wall influences

the vorticity going into the flow. It could be expected that the component of the acceleration vector perpendicular to the wall would contribute to the normal wall pressure gradient and, in turn, to the vorticity that leaves the wall surface. In the same way, the component along the wall, would contribute to the pressure gradient along the wall. Considering this, Panton concluded: "*acceleration of the wall in the normal direction does not directly contribute to the vorticity flux*". He qualified this by saying: *However, the motion may set up a true pressure gradient along the wall, which does contribute.*

The vorticity flux may be expressed as a function of the pressure gradient and motion of a solid body using the the momentum Equation (see Appendix C.1):

$$\frac{\partial \boldsymbol{v}}{\partial t} - \boldsymbol{v} \times \boldsymbol{\omega} = -grad\left(\frac{p}{\rho} + \frac{1}{2}v^2\right) - \nu curl\, \boldsymbol{\omega} \tag{6.10}$$

On the basis of Equation (6.10) Reynolds and Carr [107] formulated an expression for the vorticity flux along a rigid surface in a Cartesian system with x as the direction along the surface and y normal to the surface:

$$-\nu\frac{\partial \omega_z}{\partial y} = -\frac{\partial U_s}{\partial t} - \frac{1}{\rho}\frac{\partial p}{\partial x} - V\omega_z \tag{6.11}$$

From left to right the individual terms in this Equation are the 'Vorticity Flux' (S), 'Surface Acceleration', 'Pressure Gradient' and 'Transpiration' respectively.

The 'Vorticity Flux' term represents the flow of total vorticity out from the solid surface per unit area per unit time.

The 'Surface Acceleration' term represents the generation of vorticity at the body wall due to acceleration of the body in a fluid at rest.

The 'Pressure Gradient' term is the main source of vorticity in boundary layers. It is the source of vorticity generated on a surface at rest when the fluid above it is accelerated.

The 'Transpiration' term is a source of vorticity on moving surface.
On a curved surface Equation (6.11) is not exact, but for high Reynolds numbers it is still a good approximation as shown by Reynolds and Carr [107].

6.2.3 Flow Instability and Vortex Formation

As indicated above, unbalanced viscous forces may generate vorticity at a wall and the pressure gradient along the wall is directly related to the flux of vorticity from the wall into the flow. Pressure forces also help to determine the velocity field which in turn convects the vortex lines and stretches them. The presence of vorticity in a flow field does not, however, imply the presence of an identifiable vortex although such a vortex cannot exist without vorticity. This statement is easily explained if the concept of shear flow is introduced. The shear flow or shear layer is a region of the flow in which the velocity of the layer changes priincipally in a direction at a right angle to the flow direction and in which vorticity is highly concentrated. Thus, a parallel shear flow has vorticity but is not a vortex. The question then arises as to when and why a shear layer transforms into a vortex. The answer lies in the instability of the flow. Instability is a mechanism by which a fluid changes itself in response to strong forces and usually results in new flow patterns being created.

In a flow field, the occurrence of instability is strongly dependent on the Reynolds number as this determines the onset of the instability due to inertial forces prevailing over viscous forces. In simple terms, it can be said that below a critical Reynolds number the flow is stable and above it, the flow is unstable. If the flow is field is stable, and a small disturbance occurs, the disturbance will vanish with time. If, however, the flow field is unstable, the disturbances may amplify and often completely change the original flow. In particular, if the flow field around a body surface is unstable, the vorticity field within the boundary layer will be stimulated

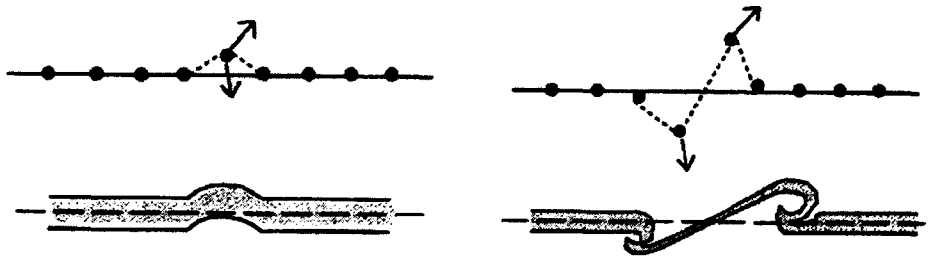

(a) Initial Perturbation (b) Later Perturbation

Figure 6.3: Vortex lines roll-up because of the instability of the flow. (Adapted from Rosenhead [113]).

by the body surface itself to roll-up into a structure within which the vorticity is highly concentrated and whose shape depends upon the cause of the instability. If, for example, the instability is due to velocity shear between layers of flow (Kelvin-Helmotz's instability) the flow rolls-up through a process that has been illustrated by Rosenhead [113] in Figure 6.3. This Figure shows that when a vortex line is displaced, the influence of its close neighbors aggravates the disturbance and the vorticity tends to concentrate into two large clusters in an irreversible process. Several other kinds of flow instability have been classified and all of them are the subject of ongoing research because of their complexity.

6.2.4 Vortex Growth and Separation

For the instability described in the previous section, once formed, the two clusters of vorticity act on each other. In fact, the velocity field of the first cluster determines the velocity of the center of the second cluster, and the velocity field of the second determines the motion of the first. Roberts and Christiansen [109], investigating

two clusters of vorticity through a numerical simulation, found that when the two clusters are sufficiently far away from each other, they rotate around each other. On the other hand, when the two clusters are very close, they merge. Somewhere, between these two situations a critical distance exists, at which the vortex clusters exchange vorticity. This situation is similar to the concept of 'dipole-charge' in the theory of electricity. In vorticity theory the 'dipole-charge' is replaced by a source and sink where the source generates vorticity that is sucked into the sink. Eventually the vorticity accumulated develops into a vortex. Once the vortex is formed, it may be considered to consist of an inner vortex core and an outer vortex flow. In the vortex-core, diffusion dominates over convection and the core rotates like a solid body through viscous diffusion. Adjacent to the core there is a region of vorticity where diffusion and convection are both significant. This region of vortex-flow is connected to the source of vorticity that feeds the vortex. This description is similar to the fluid system known as the 'Rankine vortex'. The velocity and pressure field of this vortex structure is qualitatively similar to that of the flow field of the Rankine-vortex as displayed in Figure 6.4.

After the vortex is formed, it remains attached to the body allowing the source of vorticity to keep its connection with the vortex. When this connection breaks, the source stops feeding the vortex and the vortex reaches an extreme value of vorticity and detaches from the body surface. This process can be also explained in terms of flow instability. Specifically, the vortex remains attached to the body only for small Reynolds numbers and as the Reynolds number increases beyond some critical value the vortex is shed from the body because the inertial forces overcome the viscous forces. As this happens, the fluid particles of the vortex lose their adherence to the body surface and the vortex moves into the external flow field.

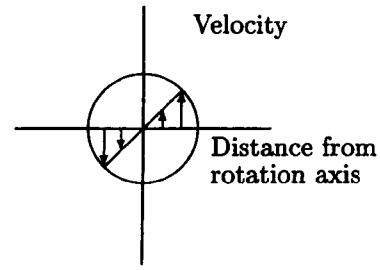

(a) Vortex-Core: velocity.

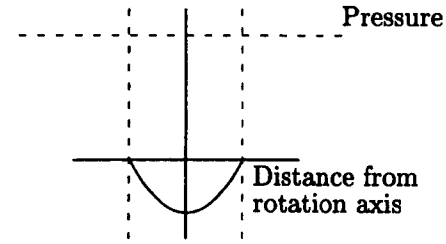

(b) Vortex-Core: pressure.

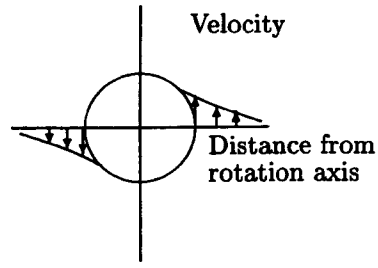

(a) Vortex-flow: velocity.

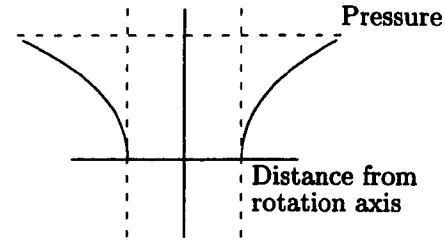

(b) Vortex-flow: pressure.

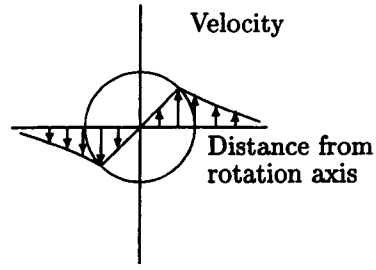

(a) Rankine Vortex: velocity.

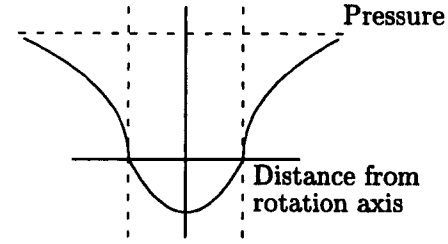

(b) Rankine Vortex: pressure.

Figure 6.4: Rankine vortex: velocity and pressure distributions.

6.3 Vorticity Flux Analysis

An investigation of the unsteady flow over the nominally two-dimensional NACA 0015 aerofoil during ramp-up motion at constant reduced pitch rate now follows. Assuming that the flow is two-dimensional, and retaining the coordinate system where y is the normal direction to the aerofoil surface and x is in the direction of the aerofoil chord, from Equation (6.3) it follows that the vorticity vector ω_z is always perpendicular to the velocity on the aerofoil surface. Furthermore, because of the large value of the Reynolds number (it is of the order $O(10^6)$, see Chapter 2), the vorticity diffusion is primarily normal to the wall. So, in the absence of transpiration, the expression for vorticity flux from the curved surface, Equation (6.11), reduces to:

$$S_{flux} = -\frac{1}{\rho}\frac{\partial p}{\partial s} \tag{6.12}$$

where s is the coordinate along the aerofoil surface. The coordinate s may be used to replace x without incurring a significant error if $\triangle x$ is assumed very small. In the present work the above definition of vorticity flux, in Equation (6.12), is used from now on for the vorticity flux in unsteady two-dimensional flow. Equation (6.12) does not take into account the contribution coming from the rotation of the aerofoil. Because the aerofoil is rotated around the quarter chord it can be assumed that the contribution coming from the body motion may be negligible. Certainly this assumption may result in some degree of error if the object of this work was to compute, in a precise manner, the location and timing of the onset of dynamic stall vortex. However, because the object of this study is to understand the key physical phenomena present during dynamic stall onset and, if possible to exploit the information gathered to develop the basis for an engineering prediction method, the omission of the surface acceleration term is unlikely to affect significantly the outcome of this study.

Before presenting the vorticity flux analysis, it is relevant to point out that the two-dimensional assumption has an important implication. The vorticity flux is considered only in the direction of aerofoil chord and it is linked to the ω_z vorticity component, Equation (6.7). It is not taken into account the flux in the spanwise direction linked to the ω_x component, Equation (6.8). The omission of this vorticity flux component will affect in some way the following analysis and in particular at span cross-sections closer to the wing tips where the flow can no longer be considered two-dimensional. It is also neglected the flux normal to the surface, Equation (6.9). The latter contribution depends upon the distribution of ω_z and ω_x on the wall itself and it is expected to be small and neglegible.

The flux of the vorticity from the nominally two-dimensional NACA 0015 aerofoil surface into the flow may be obtained as a function of time by measuring the instantaneous pressure at the wall during the ramp-up motion and calculating its gradient. The result of this calculation is shown in Figure 6.5 for a ramp-up test at reduced pitch rate 0.027. The three-dimensional plot in Figure 6.5 illustrates the variation of the vorticity flux along the nominally two-dimensional NACA 0015 aerofoil surface during the pitching motion. In the figure, the value of the surface coordinate is zero at the upper surface trailing edge and increases with distance along the surface, reaching a maximum at the lower surface trailing edge.

The following observations are relevant to all the test cases considered in this work (see Chapter 2). In fact, test cases covering a wide range of reduced pitch rate were examined in this study and it was established that the behaviour of the vorticity flux over the aerofoil surface is not qualitatively influenced by the reduced pitch rate. The reduced pitch rate does, however, influence the amount of vorticity entering the flow and the incidence at which the peak values are achieved.

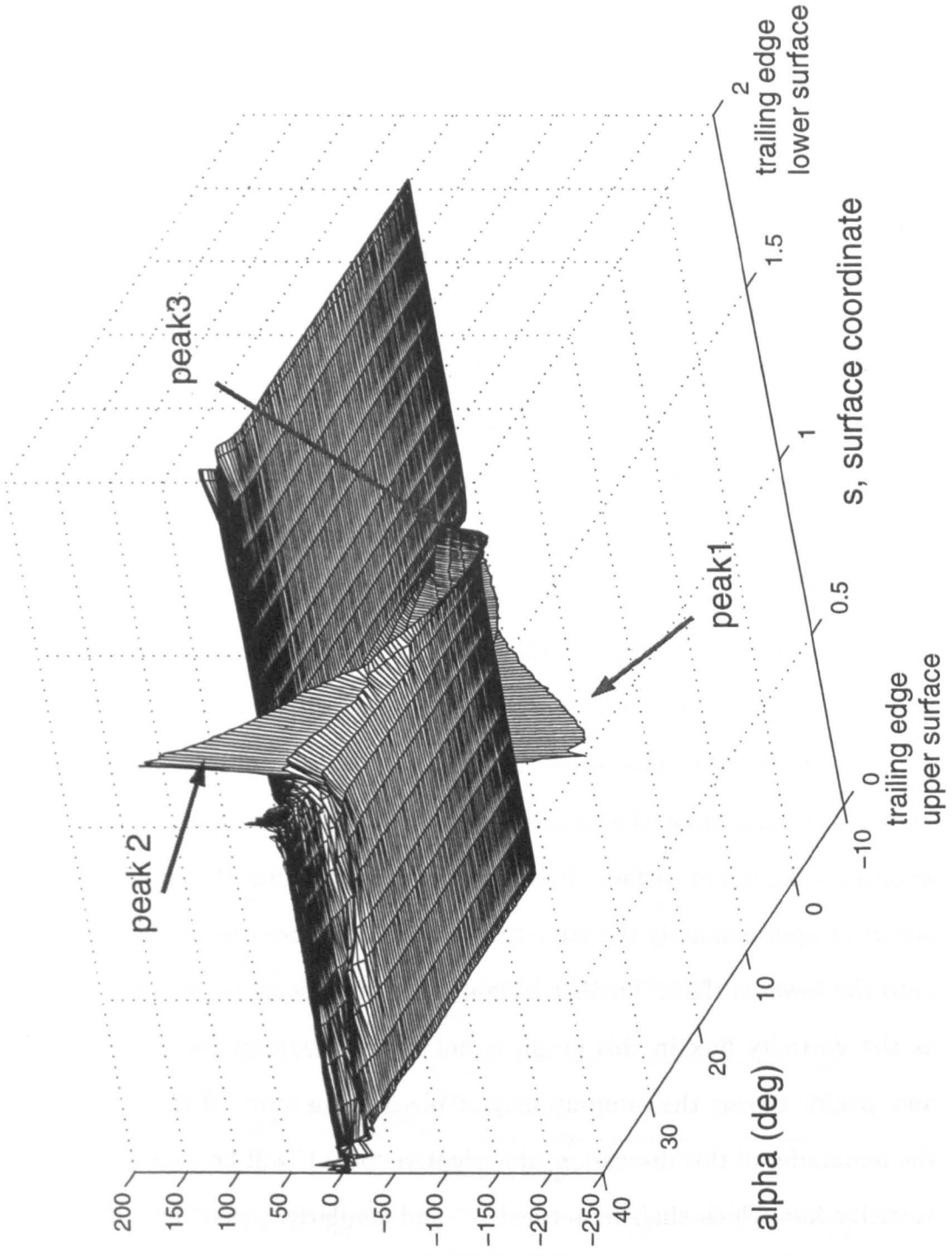

Figure 6.5: Vorticity flux over the nominally two-dimensional NACA 0015 aerofoil versus surface coordinate and incidence during ramp-up test at reduced pitch rate 0.027.

In Figure 6.5, three main peaks of vorticity flux are identified in the neighborhood of the leading edge within the first 3% of the chord. The changes in magnitude and location of these peaks during the pitching motion can be identified more clearly by focusing on the leading edge region. In Figure 6.6 the vorticity flux, normalized with respect to the local peak value, is plotted for the first 15% of chord at selected incidences during the ramp-up. Also, on each curve the position of the stagnation point is identified by an asterisk. In the early stages of the motion, Figure 6.6a, two main peaks of vorticity flux are apparent in the leading edge region. The positive peak, labelled 'peak3', is located on the right hand side of the stagnation point. Soon after the start of the ramp motion its magnitude diminishes to the extent that it can no longer be seen after about 5^0 of incidence. The negative peak, 'peak1', is initially located on the upper surface of the aerofoil close to the leading edge. As the aerofoil pitches up, the ridge moves in the same direction as the stagnation point and gets closer to the nose of the aerofoil. As 'peak1' moves, it grows in magnitude and, at the same time, the ridge of positive vorticity flux labelled 'peak2' begins to appear on the upper surface. It is interesting to note that the appearance of 'peak2' occurs at approximately the same time as 'peak1' crosses the leading edge and moves onto the lower surface. Further insight into this process is provided by Figure 6.5, as the vorticity flux in this graph is not normalized and the evolution of 'peak1' and 'peak2' during the ramp-up may be observed in terms of their magnitudes. For the remainder of this discussion, the negative 'peak1' will be considered as source of vorticity flux which shall be termed S^+ and similarly 'peak2' as a sink of vorticity S^-.

As the incidence increases further, the magnitude of S^+ increases. This suggests that the amount of vorticity leaving the aerofoil surface increases during the ramp-up motion. When the vorticity going into the flow reaches its highest value, the

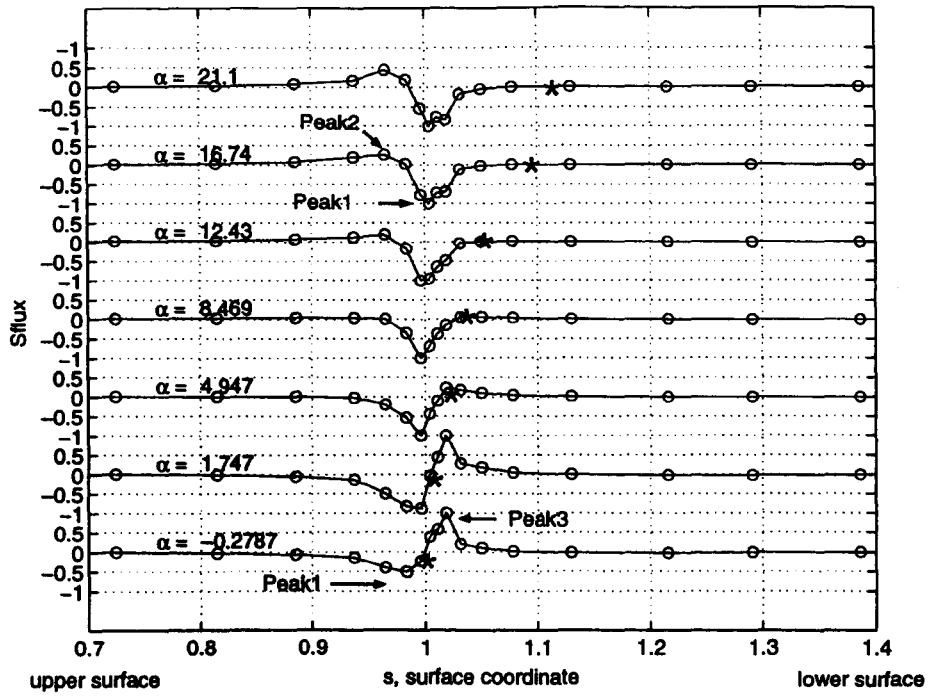

(a) pitch incidence: $\alpha = [-0.27, ..., 21.1]$

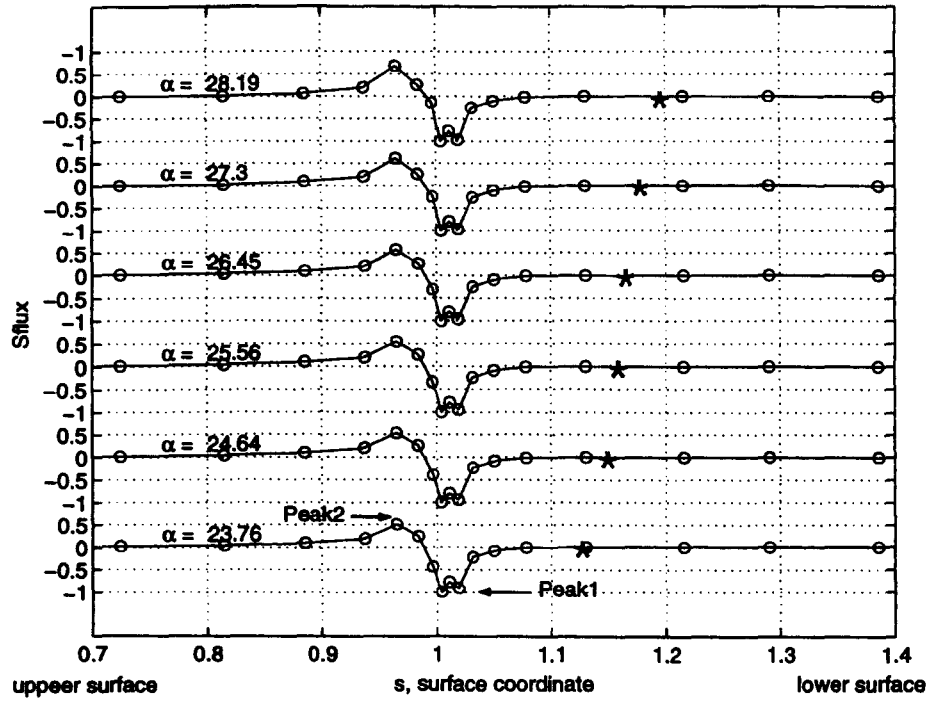

(b) pitch incidence: $\alpha = [23.76, ..., 28.19]$

Figure 6.6: Vorticity flux over the nominally two-dimensional NACA 0015 aerofoil versus surface coordinate at selected incidence during ramp-up test at reduced pitch rate 0.027

dynamic stall vortex begins to form (see Chapter 7). Soon after the source S^+ reaches its maximum, it rapidly decays. Meanwhile, the peak S^- keeps rising and reaches a maximum value much later. Consequently, the vorticity sink S^- appears to be responsible for most of the vorticity channelled into the dynamic stall vortex.

Assuming that the simplification of treating the flow as two-dimensional at inboard span sections of a wing is correct (see Chapter2), the vorticity flux over the rectangular wing during the ramp-up may be calculated by the instantaneous pressure gradient at the surface of the span sections using Equation (6.12). Following this assumption, Figure 6.7 presents the instantaneous vorticity flux distribution at 57% of span of the rectangular wing span versus chordal position for ramp-up motion at a reduced pitch rate 0.027. As in the previous case, diffusion of the vorticity appears to be mainly concentrated at the nose in two bipolar peaks: S^+ and S^-. Moreover, Figure 6.8 shows, for an incidence of 21^0 degrees, that the basic form of the vorticity distribution is the same regardless of the spanwise location on the rectangular wing. It may be also observed that the vorticity flux distribution over the NACA 0015 aerofoil, at the same incidence, is very similar to the distributions at 57% and 68% of span on the finite wing. This suggests that, at inboard sections at least, the two-dimensional assumption may be appropriate for the finite wing. It is accepted, however, that Equation (6.12) will not hold in the neighborhood of the wing tips.

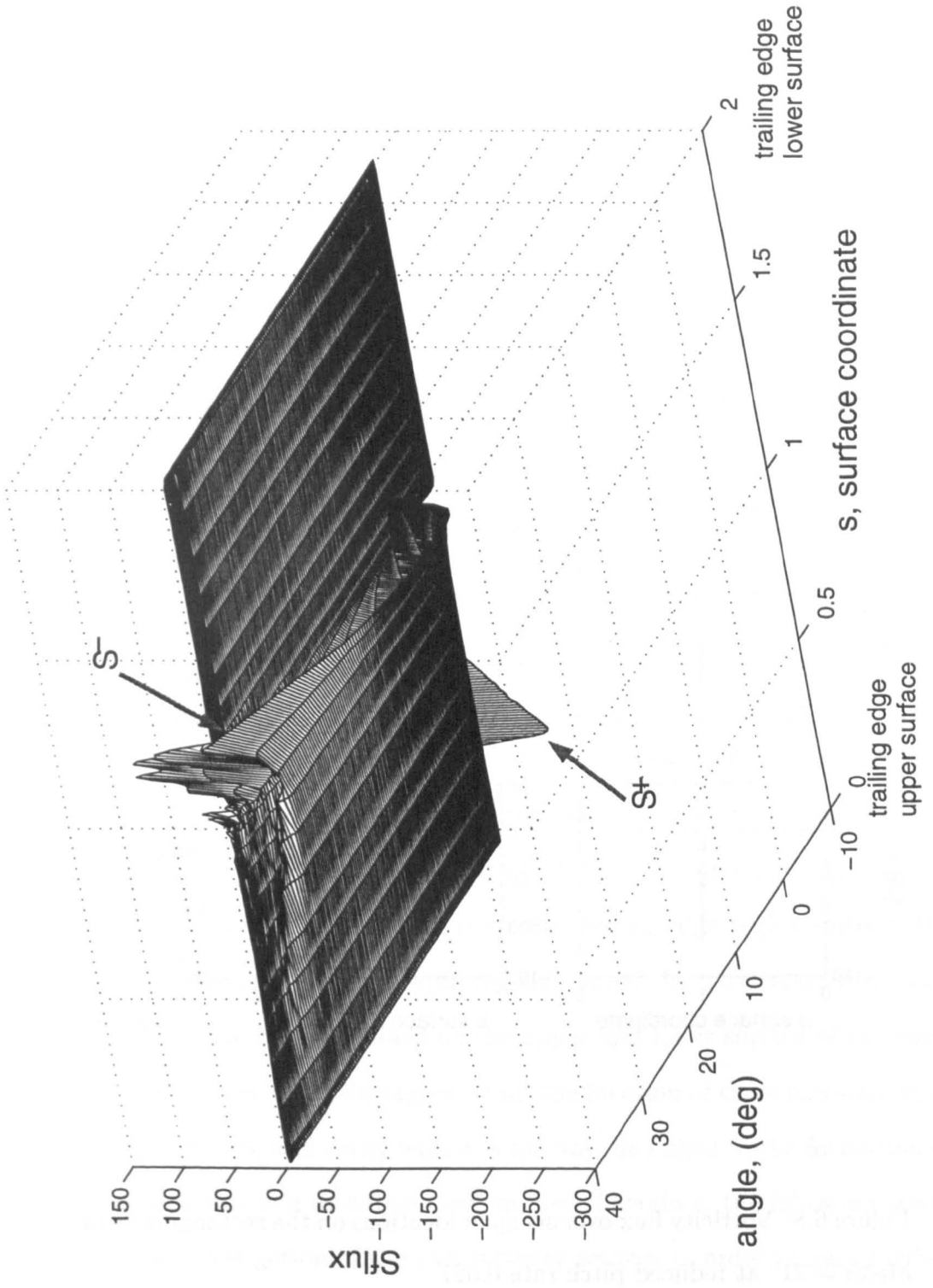

Figure 6.7: Vorticity flux over 57% of span of the rectangular wing versus surface coordinate and incidence at reduced pitch rate 0.027.

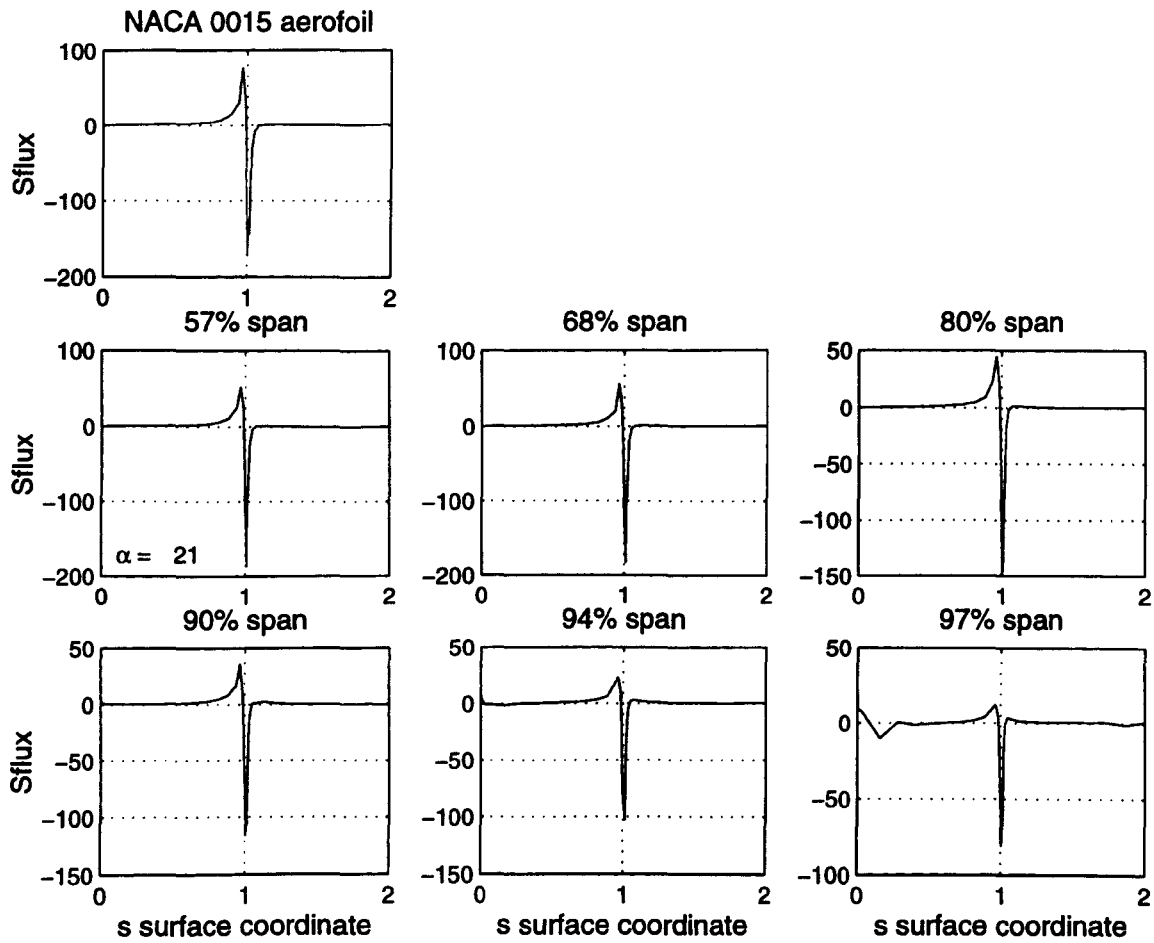

Figure 6.8: Vorticity flux over six span locations on the rectangular wing at incidence $alpha = 21^0$ at reduced pitch rate 0.027.

Chapter 7

Detection of Dynamic Stall Vortex Inception

7.1 Introduction

The flow visualization tests [100] and the temporal chordwise vorticity analysis (see Chapter 6) have shown that the distinguishing feature of dynamic stall is the shedding of significant concentrated vorticity from the leading edge region in both the nominally two-dimensional and three-dimensional cases. In particular, two main sources of vorticity have been identified on the upper and lower surface of the leading edge region. Previous work [28] suggests that the location of these two sources of vorticity and their growth and decay will, in some way, be linked to the formation of the dynamic stall vortex and its subsequent motion. Therefore, the following study focuses on a local investigation of the two vorticity sources in order to gain further insight into the process by which this vorticity is channeled into the dynamic stall vortex and to use this information to determine the onset of dynamic stall itself. In this context, it is appropriate to examine the relationship between methods used to model dynamic stall and the behaviour of the vorticity flux.

Several methods have been suggested to model dynamic stall and they can be classified into those based on knowledge of experimental two-dimensional dynamic stall data (semi-empirical methods) and those based on computed fluid flow behaviour (Navier-Stokes calculation techniques). Among the semi-empirical methods the most commonly used in industry are variants [6], [8], [71], [73], [75] of the Leishman-Beddoes model [74], the Onera scheme [16] and the Boeing [63] and MIT Stall methods [51]. These methods predict dynamic stall air-loads through semi-empirical equations that take into account the geometric features of the aerofoil and the aerodynamic response of the aerofoil estimated from experimental tests. For example, the Boeing method calculates the lift, pitching-moment and drag coefficients using static aerofoil data obtained experimentally for the appropriate angle of attack and Mach number range. These results are then corrected using dynamic stall information obtained from oscillating aerofoils. Methods following the Leishman-Beddoes approach [74] utilize an indicial function written in terms of Mach number and velocity field computed from two-dimensional experiments. The function formulated for the two-dimensional field can be also used to estimate three-dimensional dynamic loads if the induced flow field is also considered. A crucial aspect of dynamic stall models is the determination of stall onset incidence since it is the most difficult aspect of dynamic stall to predict accurately. Beddoes [4] suggested that each dynamic stall event is governed by a distinct non-dimensional time constant, regardless of the time history of the motion. In particular, Beddoes suggested that a time constant exists between reaching the static stall incidence and the maximum lift incidence of an aerofoil undergoing pitching motion. The static stall incidence was defined by Beddoes as the angle of attack at which there is an abrupt drop in the pitching moment curve. Wilby [128] examined aerofoils undergoing oscillatory motion during which the mean angle was steadily increased whilst the amplitude and reduced frequency were fixed. Wilby concluded that the incidence at which the

formation of the dynamic stall vortex begins can be estimated through the analysis of the pitching moment coefficient. In particular, for each cycle, Wilby calculated the difference between the minimum value of the pitching moment coefficient and its unstalled value. These differences were plotted against the maximum incidence achieved during the cycle and the intersection of the plotted curve with the x-axis provided the incidence of dynamic stall vortex initiation. Alternatively, Scruggs et al. [116] defined dynamic stall onset as occurring at the incidence where there is a sudden deviation of the gradient of the normal force coefficient curve. Galbraith et al. [46], [45] suggested a method based on pressure measurements that involved the examination of individual pressure traces at a given chordal location to determine any sudden changes in the temporal pressure gradient associated with the vortex formation.

Because the method proposed by Galbraith et al. is possibly the mostly straight forward to implement when analyzing pressure data, the relationship between this Cp-deviation and the behaviour of the vorticity flux sources will now be examined. The Cp-deviation technique provides a fast approach to the prediction of dynamic stall onset but, on the other hand, can be subjective as will be discussed in the next section. Because of this, after initially examining the relationship between vorticity flux and Cp-deviation, another method for predicting the stall, proposed by Evans and Mort [26], is introduced and is re-evaluated in light of the vorticity flux analysis.

7.2 Cp-Deviation and Vorticity Flux

7.2.1 Cp-Deviation Method

The method formulated by Galbraith et al. [46], [45] for the prediction of dynamic stall vortex onset is based on the analysis of experimental pressure data. Galbraith

et al. analyzed a set of experimental pressure data recorded on a number of aerofoils undergoing ramp-up motion and found that the first sign of the dynamic stall vortex could be identified in the temporal pressure coefficient distribution. The method involves the examination of individual pressure traces on the upper surface of the aerofoil at a given chordal location during ramp-up to determine any sudden changes in the temporal pressure gradient, Figure 7.1a. The first indication that the dynamic stall vortex has been initiated is when an abrupt deviation in the gradient of the pressure coefficient trace is observed: *Cp-deviation*, Figure 7.1. Cp-deviation occurs first in the region of the leading edge between about 10% and 17% of the chord and then progresses to adjacent chordwise locations as indicated in Figure 7.1a by the label 'Cp deviation area'. The chordal location at which Cp-deviation occurs first determines the incidence of the onset of dynamic stall. This incidence is defined as the intersection between two straight lines, which are determined by extrapolation of the experimental pressure data before and after the deviation of the pressure gradient coefficient as shown in Figure 7.1b. The limitation of this approach is that the dynamic stall onset incidence can only be determined accurately if measurements are made at the chordal location where the vortex first forms. This introduces an element of subjectivity into the method. Nevertheless, it has been established that the Cp-deviation is generally a reliable indicator of dynamic stall vortex formation despite this subjectivity. The way in which the vorticity flux behaviour relates to Cp-deviation is now considered.

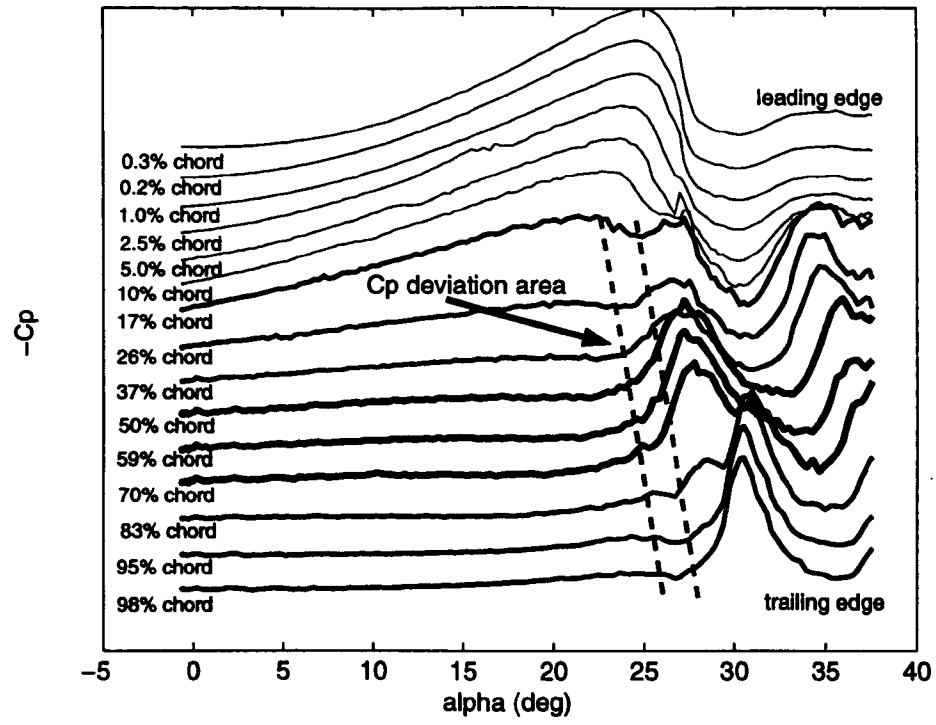

(a) Cp vs. alpha at 15 chord locations on the aerofoil upper surface.

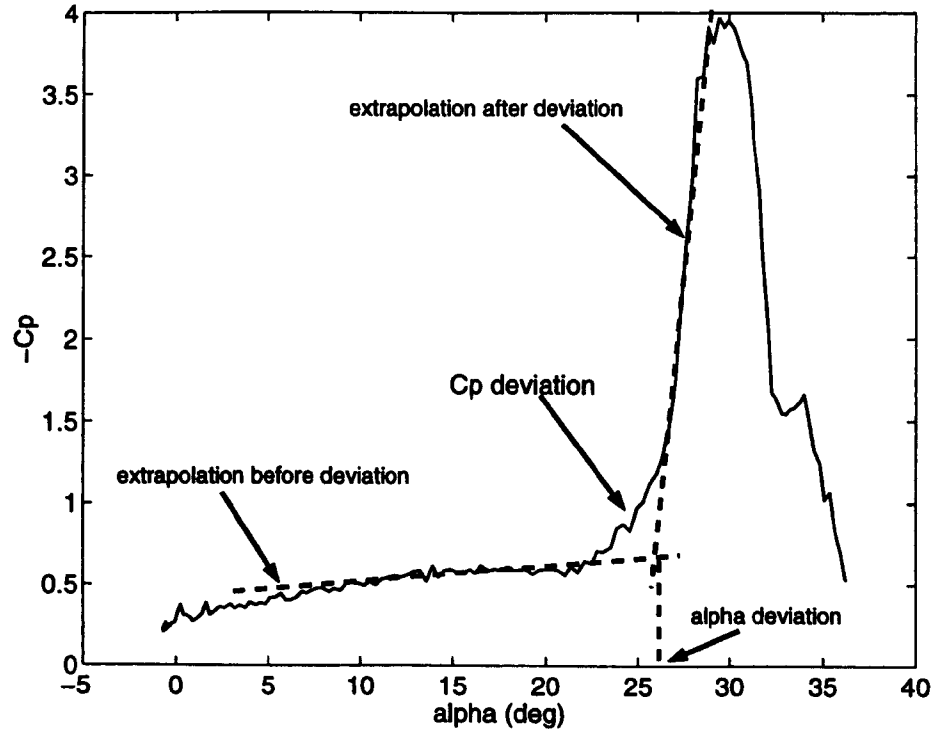

(b) Cp vs. alpha at 17% of the chord of the aerofoil upper surface.

Figure 7.1: Cp-deviation method for the prediction of dynamic stall vortex onset. The data are relative to the nominally two-dimensional NACA 0015 aerofoil at reduced pitch rate 0.0217.

7.2.2 Vorticity Flux and Dynamic Stall Onset

The previous analysis of the temporal evolution of the vorticity flux during a pitching motion (see section 6.3) has shown the behaviour of the two vorticity sources located on the lower and upper surface of the aerofoil leading edge. A detailed investigation of the peaks S^+ and S^- associated with the highest vorticity values may provide a means of identification of the dynamic stall vortex mechanism. This is now examined.

Figure 7.2 shows the angle of attack versus reduced pitch rate at which the vorticity flux reaches both minimum and maximum values (peaks labeled as S^- and S^+ in Figure 6.7), at three span locations on the rectangular wing and on the nominally two-dimensional NACA 0015 aerofoil. It may be observed that the vorticity flux on the upper surface of the leading edge always reaches its maximum value slightly later than the minimum is achieved on the lower surface. Moreover, the gap increases at higher reduced pitch rates at the 57% and 68% of span positions on the rectangular wing. This observation and the temporal evolution of the vorticity flux during pitching motion observed in section 6.3 suggests the following explanation. At the beginning of the motion, flow instabilities cause a concentration of vorticity in two clusters on the upper and lower sides of the aerofoil (see section 6.2.3). At the start of the ramp-up, the fluid accelerating around the leading edge energizes the vorticity cluster on the lower side of the nose which remains closely connected to the vorticity cluster on the upper surface. During this period, the magnitude of the vorticity flux is increasing as the chordwise vorticity flux distribution shows in Figure 6.7. After some time, possibly when the stagnation point has moved some distance aft (refer to Figure 6.6), the accelerating flow particles can no longer energize the lower surface vorticity source, the vorticity flux on the lower surface of the aerofoil decreases and soon after the vorticity flux on the upper surface of the aerofoil reaches its peak

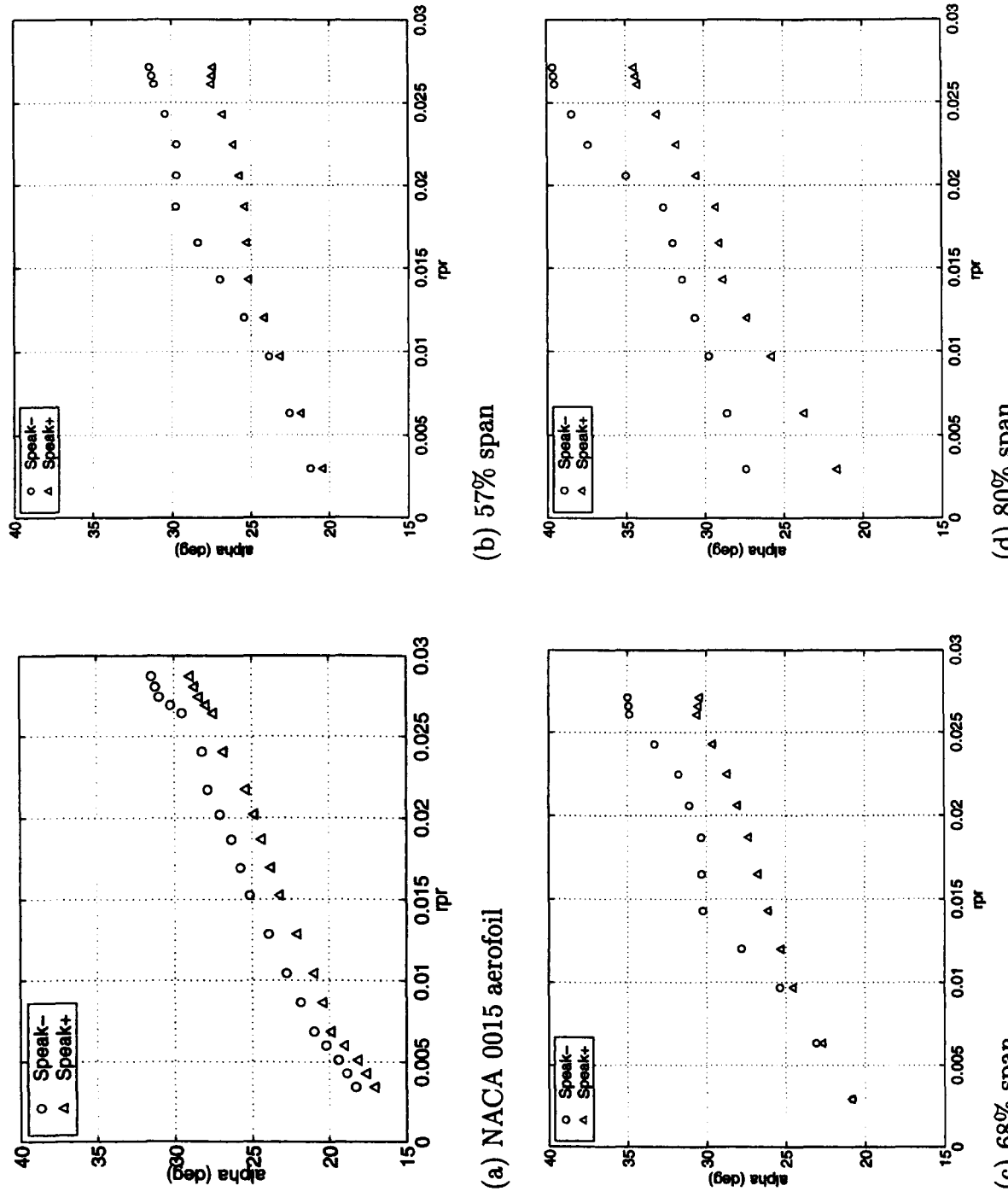

Figure 7.2: Peaks S^- and S^+ of vorticity flux at inboard sections of the rectangular wing and nominally two-dimensional NACA 0015 aerofoil at several reduced pitch rates.

(peak S^-). At this point, all the vorticity collected on the upper surface is released and appears as the dynamic stall vortex. The vortex builds up thanks to the vorticity that is gradually liberated. As the dynamic stall vortex grows in size and strength secondary effects in the process cause the convection of the vortex itself.

7.2.3 Cp-Deviation and Vorticity Flux Peak S^+

The way in which the vorticity flux behaviour relates to Cp-deviation is now considered. Figures 7.3 a, b, c, d show the Cp-deviation incidence as function of reduced pitch rate on the nominally two-dimensional NACA 0015 aerofoil and at three span stations on the rectangular wing. In each case, the chordal position at which the first sign of Cp-deviation has been traced is at 17% of the aerofoil chord. Also shown in figure is the corresponding variation of the incidence at which the minimum value of the vorticity flux (peak S^+) occurs. At the most inboard span positions, Figure 7.3b and 7.3c, the level of agreement between the two events is very good. The same comparison for the nominally two-dimensional NACA 0015 aerofoil, Figure 7.3a, shows that the incidence of Cp-deviation corresponds well to that of the S^+ peak across the range of reduced pitch rate although there is some divergence at higher reduced pitch rates; possibly due to the subjectivity in determining the Cp-deviation. The affinity of the two curves in Figures 7.3a, b, c suggests that the behaviour of the S^+ peak may be an indicator of vortex inception. At 80% of span the level of agreement between the two methods deteriorates with the minimum flux value lagging Cp-deviation. The anomalous result at 80% of the span, may suggest that the stall initiation process at this location is strongly affected by three-dimensional effects that alter the response of the vorticity flux and render the two-dimensional assumption invalid.

It is interesting to observe that the incidence at which the S^+ peak occurs is located

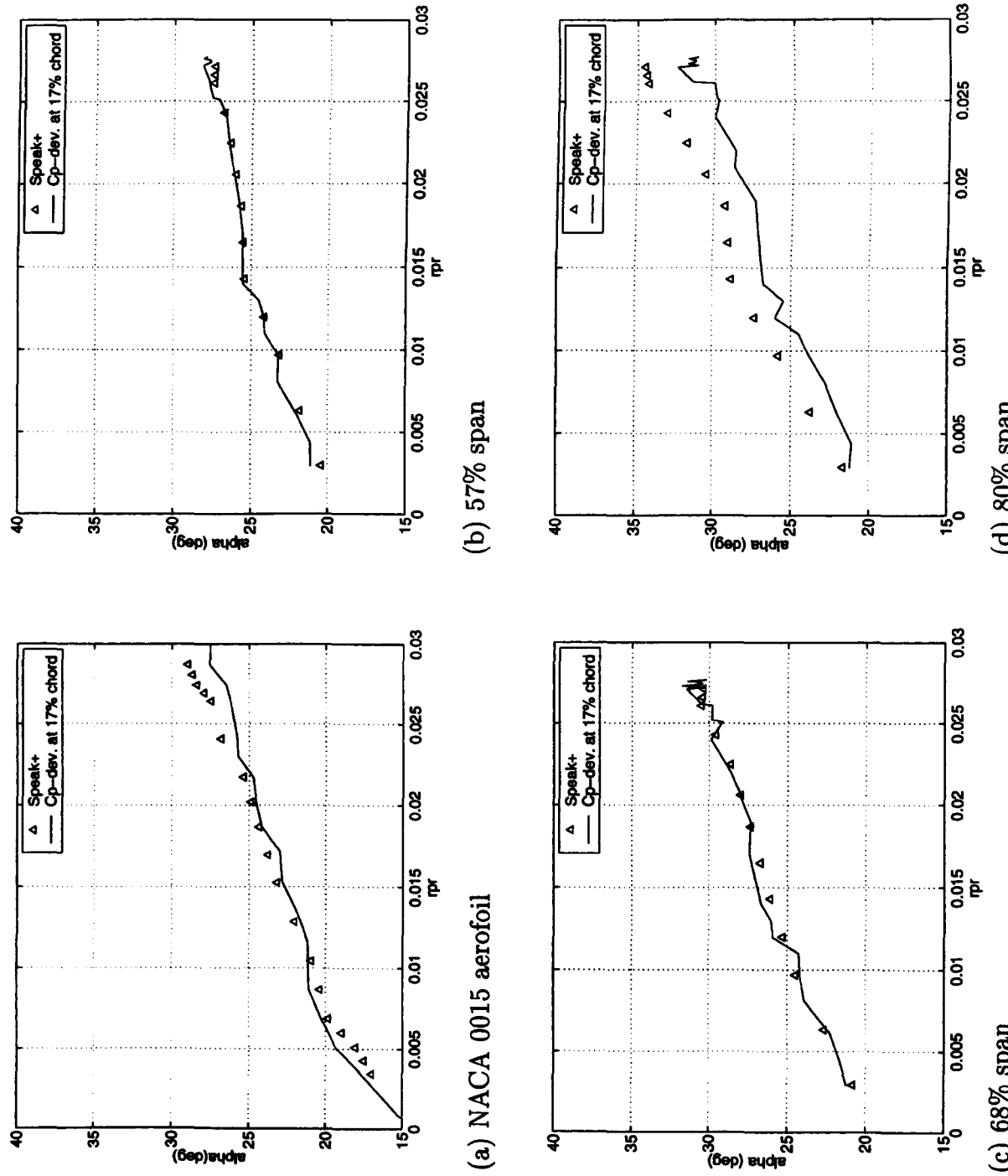

Figure 7.3: Cp-deviation and vorticity flux peak S^+ for several reduced pitch rates.

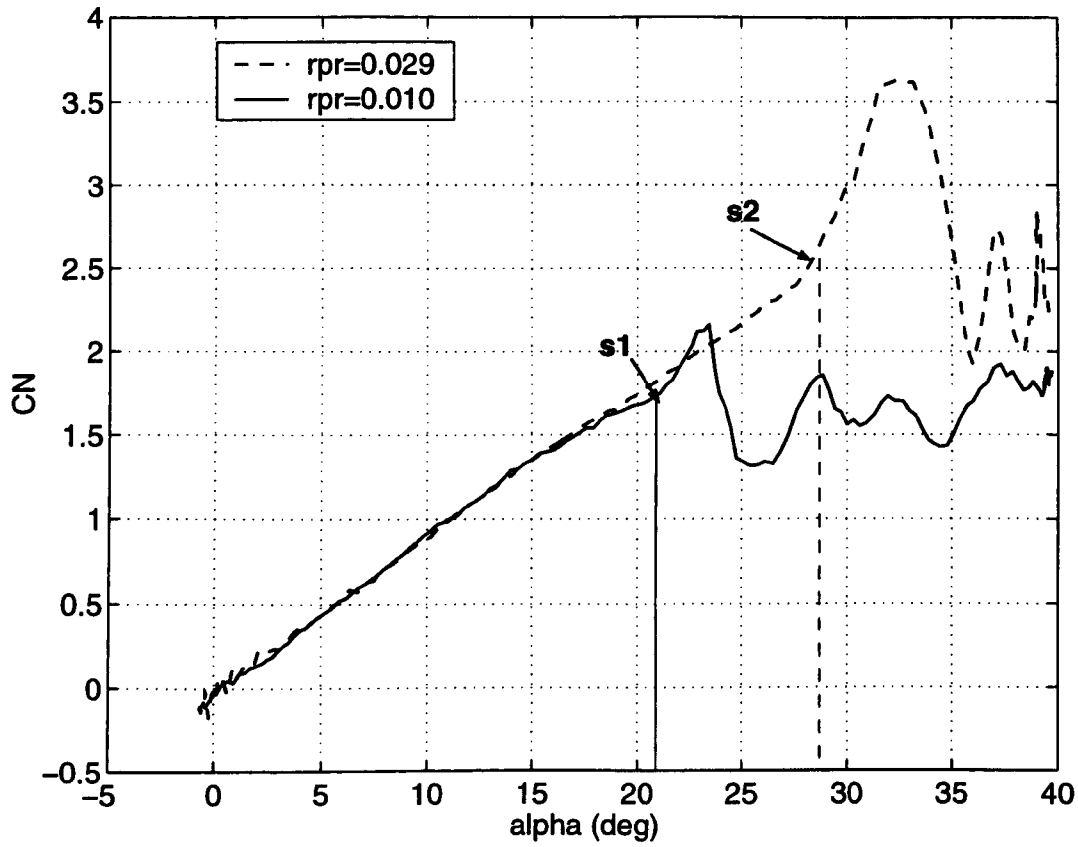

Figure 7.4: Correlation between normal lift coefficient and pitch incidence corresponding to the minimum peak value S^+. The data are relative to the nominally two-dimensional NACA 0015 aerofoil for two reduced pitch rates.

on the CN-alpha curve in the area indicated by Carr [10] as being where the dynamic stall vortex formation has started, (see Chapter 4, Figure 4.6). This is shown for two reduced pitch rates in Figure 7.4.

It is, therefore, clear that the formation of the dynamic stall vortex is closely related to the temporal evolution of the two local sources of vorticity flux located around the leading edge. On the basis of these observations and in view of the inaccuracy of the Equation (6.11) at the outboard station of the wing span where the three-

dimensional effects are not negligible, it may be assumed that determination of the incidence of the S^+ peak may provide a reliable method for identifying the onset of the dynamic stall vortex in the absence of strong three-dimensional effects.

7.3 Alternative Technique

Static stall has been widely studied by many authors who suggested a range of methods to predict the stall onset. Some of them are based on the collapse of suction at the leading edge after it was established that the pressure response near the leading edge is related to the extent of separated flow on an aerofoil. Static stall can be classified as either 'trailing edge stall' or 'nose stall'. The latter can be further subdivided into 'leading edge stall' and 'thin aerofoil stall', [42, 93, 94, 95, 96]. 'Trailing edge' stall is characterized by a gradual spreading forward of separation initiated at or near the trailing edge. 'Leading edge stall' is characterized by the sudden appearance of extensive separation from the vicinity of the leading edge, whereas 'thin-aerofoil stall' is distinguished by a gradual spreading rearward of separation that is initiated at or near the leading edge. The leading edge stall is the most abrupt and two mechanisms have been identified as the cause of this stall. These two mechanisms are commonly known as *'bubble-bursting'* and *'re-separation'*. The 'bubble-bursting mechanism' is the sudden failure of the detached boundary layer downstream of laminar separation to reattach to the surface. The 're-separation mechanism' consists of the sudden re-separation of the boundary layer a short distance downstream of the bubble. Tani [124] and later Owen and Klanfer [104] proposed a criterion for distinguishing between the two mechanisms. This criterion is based on the determination of the boundary layer Reynolds number at laminar separation (R_θ) and establishes that, for a given test condition, the leading edge stall is due to re-separation if R_θ is above a critical value otherwise the nose stall

may be due to bubble-bursting or either mechanism if R_θ is close to the critical value. Evans and Mort [26], studying the stall due to the re-separation mechanism on two-dimensional aerofoils, found a correlation at the critical value of R_θ for the behaviour of the velocity distribution over the aerofoil surface at stall. In detail, all the nominally two-dimensional aerofoils were tested in a flow field characterized by a Reynolds number of $O(10^6)$ and Mach number not greater than 0.2. For these test conditions the critical value R_θ was known to be 350. Evans and Mort assumed that the re-separation on the aerofoil surface occurs where the velocity falls 6% from its peak value and found that a correlation existed around the critical value R_θ of 350 between the maximum peak velocity U_p/U_∞ and a parameter ΔS, Figure 7.5. The parameter ΔS is related to the adverse pressure gradient between the peak velocity and the separation point and, in particular, is the distance along the aerofoil surface between the points where the velocity had dropped 1% and 6% respectively, from the peak value as illustrated in Figure 7.6.

Beddoes [7] illustrated theoretically that, for practical applications, the variations in both U_p and ΔS with pitch rate were small and, therefore, it was possible to assume that they were constant for a given aerofoil at a given Mach number. This result allows extension of the Evans and Mort correlation curve into the dynamic regime at Reynolds numbers of $O(10^6)$ and Mach numbers not greater than 0.2.

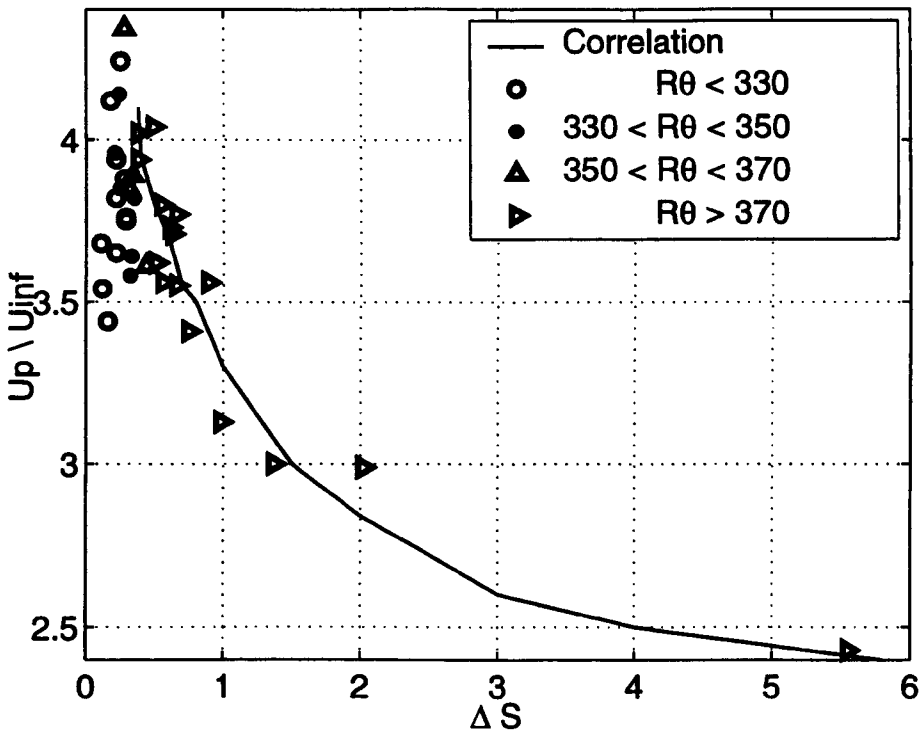

Figure 7.5: Evans & Mort correlation of peak velocity ratio at stall versus ΔS parameter correlated to the adverse velocity gradient. (Adapted from Evans & Mort [26]).

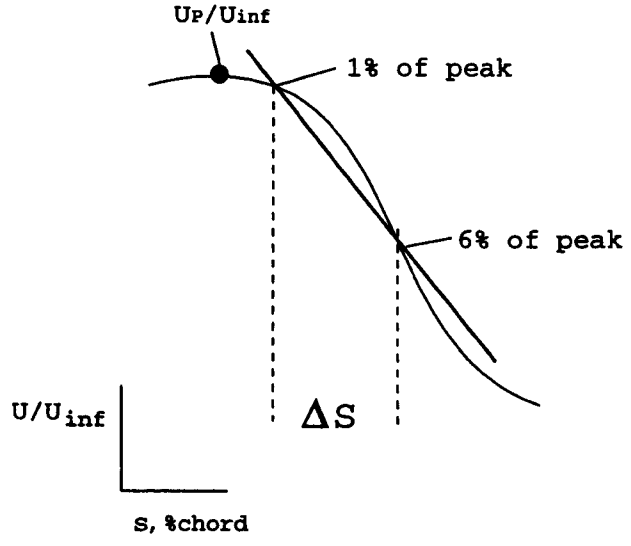

Figure 7.6: Sketch of Evans & Mort method. (Adapted from Evans and Mort [26]).

7.3.1 'Evans & Mort' and Cp-Deviation Methods

In order to apply the Evans and Mort method [26] to the experimental pressure data, the velocity distribution over the surface of the models had to be computed through the well known relation $Cp = 1 - (U/U_\infty)^2$ for steady flow on the basis of Beddoes conclusion [7]. For each ramp-up test, the set of parameters U_p/U_∞, $\triangle S$ that met the Evans and Mort correlation was calculated. Figure 7.7 illustrates, in terms of normal force coefficient, the incidences at which the Evans and Mort correlation indicates stall onset at two reduced pitch rates. The points are identified with the symbols e_1, e_2.

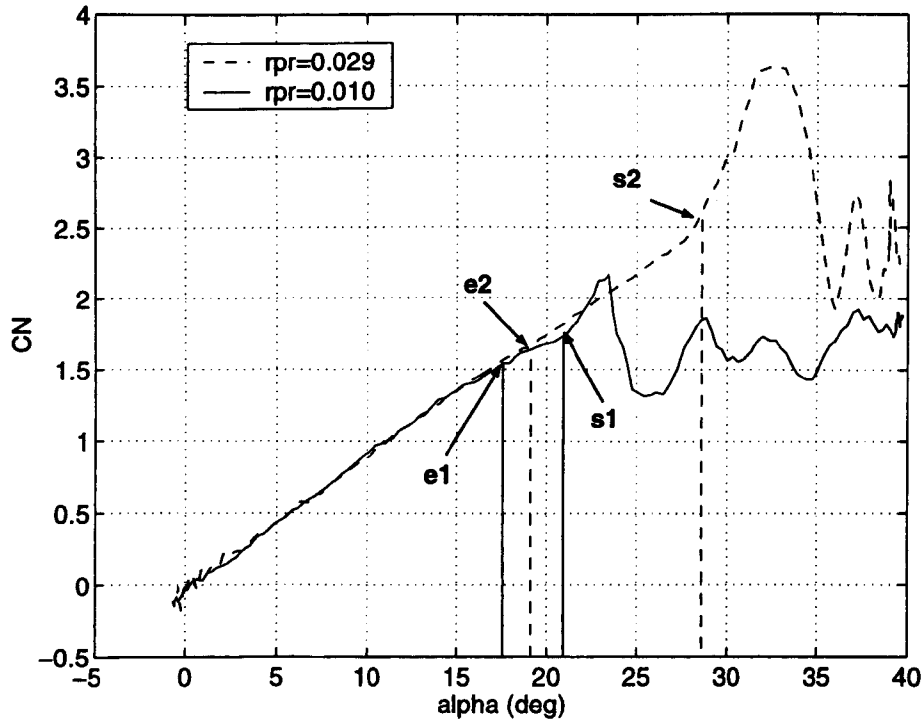

Figure 7.7: Normal force coefficient curves at two reduced pitch rates showing stall onset locations predicted by the Evans & Mort correlation and vorticity flux. The data are relative to the nominally two-dimensional NACA 0015 aerofoil.

Figure 7.7 also shows the corresponding values on the normal force coefficient curves

of the incidences at which the vorticity flux reaches the minimum peak S^+: s_1, s_2. The incidences predicted by the Evans and Mort criterion are lower than those corresponding to the occurrence of peak S^+. Their respective locations on the $CN - \alpha$ curves also suggest that they are related to two different temporal aspects of the same event. Specifically, the intersections e_1 and e_2 may identify the initial boundary layer breakdown on the upper surface near the leading edge whereas the points s_1 and s_2 indicate the initiation of dynamic stall vortex formation. If this is correct, it would be expected that, at each span location and at all reduced pitch rates, the incidences predicted by the Evans and Mort criterion would be earlier than the occurrence of peak S^+. Figure 7.8 confirms this speculation by presenting the calculated delay between the two events at a number of reduced pitch rates for the nominally two-dimensional NACA 0015 aerofoil test cases. In this figure the non-dimensional time at which each event is calculated is plotted against the reduced pitch rate. The time delay between the two events is small and interestingly, is approximately constant in the fully dynamic regime. The behaviour exhibited in Figure 7.8 suggests that the time that elapses between boundary layer breakdown and first onset of the dynamic stall vortex is small. Possibly more significantly, the reduced pitch rate does not affect the temporal sequence of events leading to vortex formation once they have been triggered. This observation seems to be confirmed by Figure 7.9, where at the first two inboard sections (57%- 68% span) of the rectangular wing, the non-dimensional time delay between the Evans and Mort condition and peak S^+ is almost constant. It also has approximately the same value at each span section suggesting that the aerofoil profile shape dominates this phenomenon which appears relatively insensitive to three-dimensional effects. At 80% of span the non-dimensional time delay is still constant but the magnitude of the delay is higher than the one at inboard sections. This suggests that the dynamic stall vortex formation it is not characterized by the only response of the leading edge

aerofoil because if it was true the time delay would be the same at all span-sections. The time delay is even larger at 90% span. This suggests that the 80% and 90% span are sensitive to three-dimensional effects caused by the adjacent spans. The onset prediction is inaccurate at cross-span sections closer to the wing tips, because of the two-dimensional assumption. In light of the analysis carried in this study, it would be expected that in three-dimensional flow S^+ peak occurs later and the time-delay curve would be quantitatively affected at these span locations. Only a three-dimensional flow analysis can properly estimate the time-delay of the events. It may be concluded that there is a clear change in the temporal sequence of the events leading the vortex formation along the span and only a three-dimensional flow analysis would take into account the vorticity flux contribution in the spanwise direction (see Chapter 6, section 6.3) and would provide more accurate results.

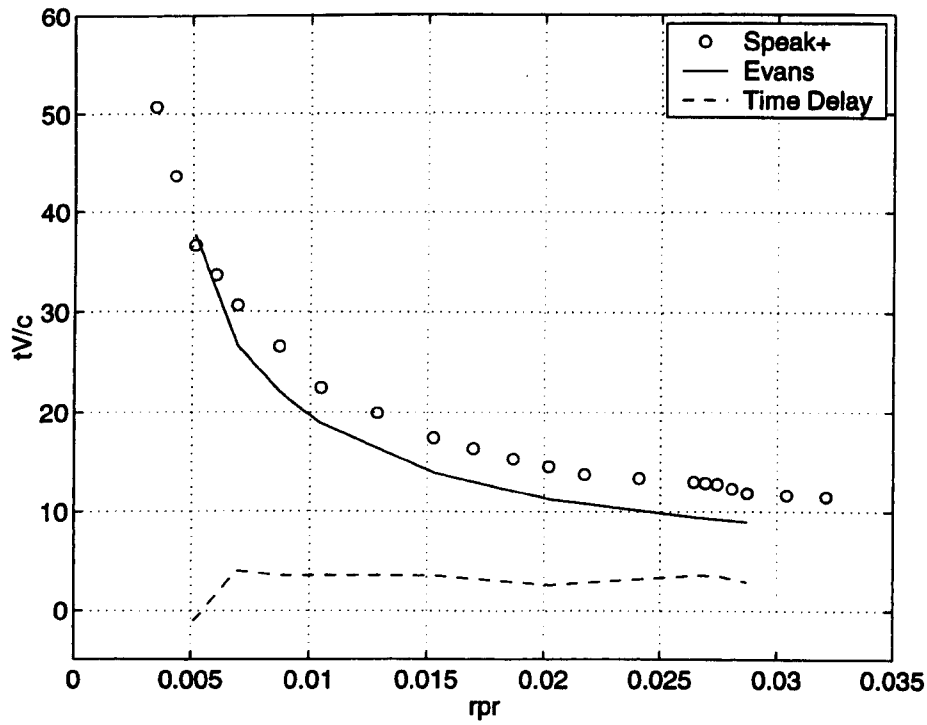

Figure 7.8: Vorticity flux peak S^+ occurrence on the nominally two-dimensional NACA 0015 aerofoil and Evans & Mort prediction for a range of reduced pitch rates.

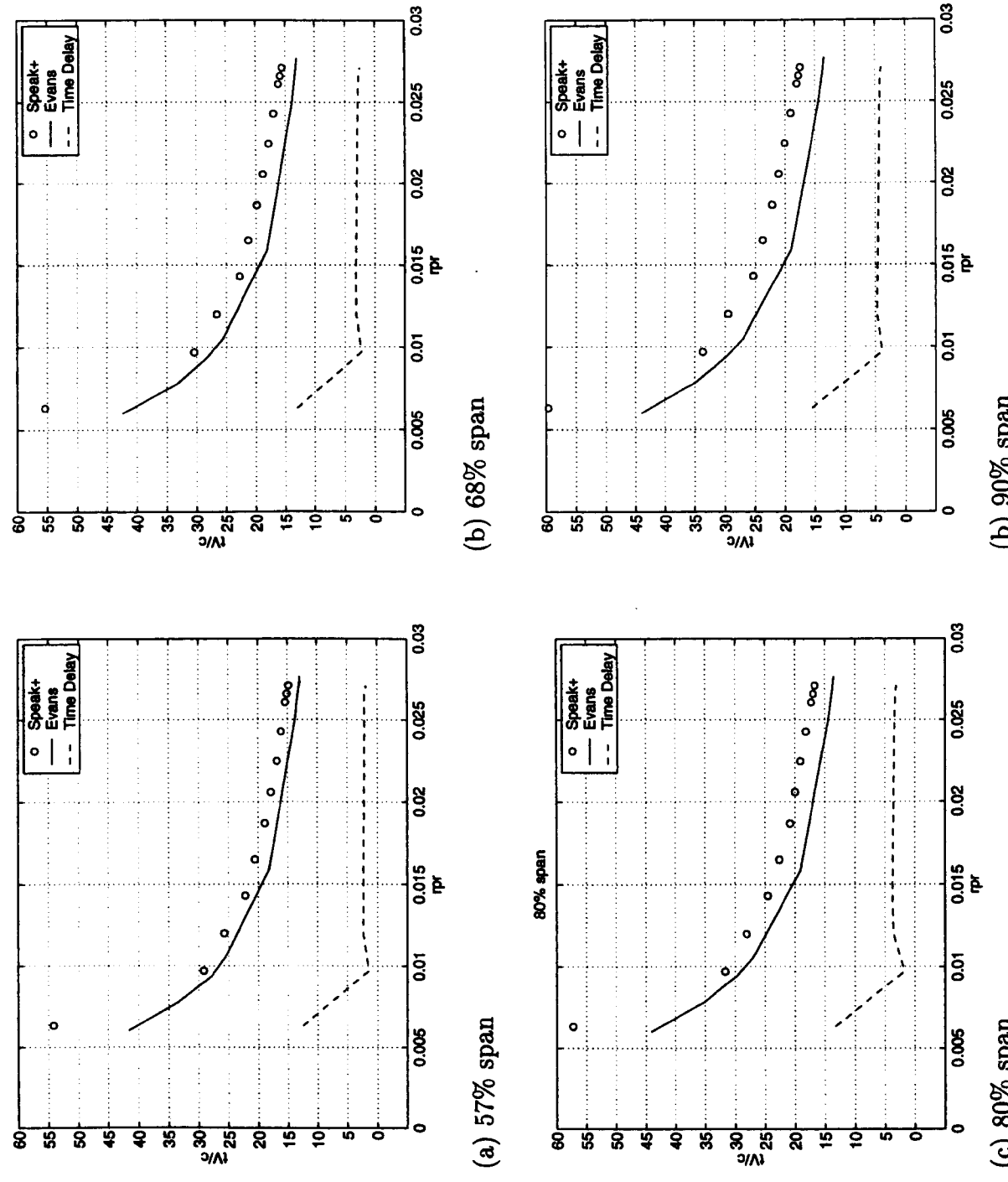

Figure 7.9: Vorticity flux peak S^+ occurrence at inboard sections of the rectangular wing and the Evans & Mort prediction.

7.4 Discussion on Three-Dimensional Effects

Figure 7.10 shows the peak S^+ prediction at inboard span sections of the rectangular wing and the two-dimensional NACA 0015 aerofoil for a range of reduced pitch rate. This figure clearly shows the effect of the downwash on the temporal events of the dynamic stall. In fact, on the finite rectangular wing, the evolution of the stall process generally appears later than on the nominally two-dimensional NACA 0015 aerofoil because of the downwash. This figure also suggests that the leading edge pressure response becomes critical at the mid-span before the more outboard sections. Thus, if S^+ is a reliable indicator of vortex formation, the implication is that the vortex forms first at the mid-span before propagating outboard.

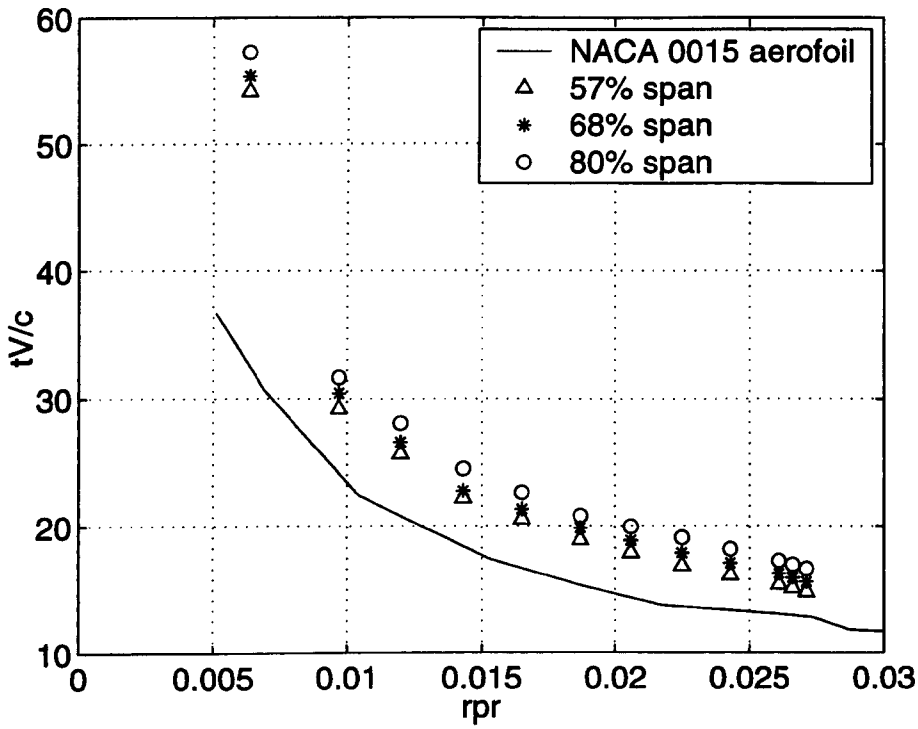

Figure 7.10: Occurrence of vorticity flux peak S^+ on three span locations of the rectangular wing and on the nominally two-dimensional NACA 0015 aerofoil for a range of reduced pitch rates.

The conclusions arising from Figure 7.10 and the relationship between the Evans and Mort correlation and the S^+ peak at 80% of span, Figure 7.9 c, bring the most significant result of this study. This result may be outlined step by step as follows. Figures 7.3a, b, c demonstrate that the S^+ peak corresponds well with the first tangible sign of the dynamic stall vortex depicted by Cp-deviation at the more inboard wing span sections and on the nominally two-dimensional NACA 0015 aerofoil. At 80% of span the Cp-deviation occurs before the S^+ peak is achieved. This result suggests two possible conclusions. One might be that the two-dimensional assumption adopted for the evaluation of the vorticity flux may be incorrect at this span section. This issue, however, is relevant to the suitability of the S^+ minimum as an indicator of vortex formation and does not change the fact that there is a clear change in the temporal sequence of the events leading to vortex formation at span sections closer to the wing tips. The second conclusion might be that a further mechanism plays an important role in the onset of the stall. On the basis of this, the key to understanding the onset mechanism lies in Figure 7.10 where it is shown that the vortex formation occurs first at mid-span and, then, outboard. This result has to be correlated to the leading edge pressure response. In fact, the consistent relationship at all span sections between the Evans and Mort correlation and the S^+ peak, that are representative of two different aspects of the leading edge response, suggests that the leading edge behaviour does not trigger vortex formation at 80% of span. It may be concluded that the onset of vortex formation begins at the mid-span and, once this happens, the local vorticity field is disturbed and this disturbance propagates rapidly towards the wing tips. If this is so, the formation of the vortex at the mid-span is the triggering mechanism for the vortex formation outboard. The significance of this is that all two-dimensional semi-empirical models that predict vortex onset via some form of leading edge pressure criterion that are extended to the three-dimensional field by taking simply into account the induced

flow field, will give an erroneous prediction of the vortex onset. They will predict vortex onset later than it actually occurs on outboard wing sections.

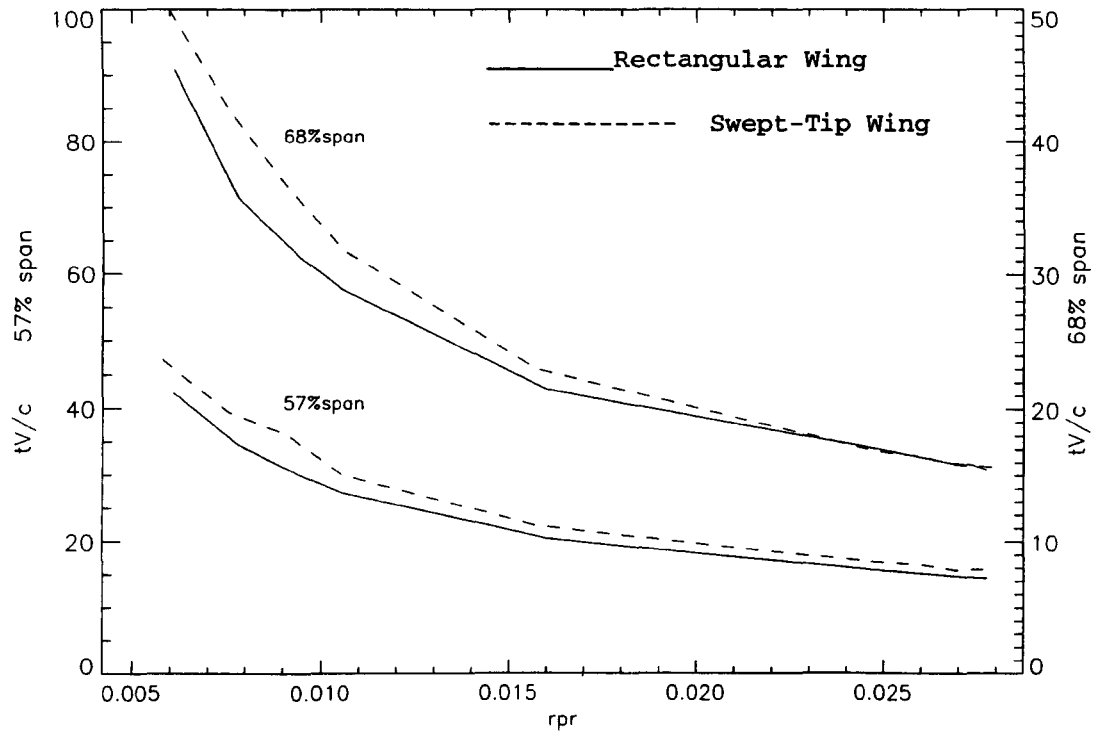

Figure 7.11: Occurrence of peak S^+ of vorticity flux at two span locations of rectangular wing and 60^0 swept-tip wing for a range of reduced pitch rates.

The flow visualization tests [100] and the analysis carried out in Chapter 5 highlighted the aerodynamic effects of the swept-tip geometry on the flow characteristics. It has been observed that the tip-vortices on that wing affect the flow features over a wide portion of the span than on the rectangular wing. Because of this, downwash affects a wider portion of swept-tip wing than the rectangular wing. It is, therefore, to be expected that the vorticity flux peak S^+ would occur later on the swept tip wing. This is confirmed by Figure 7.11 which shows the timing of the S^+ peak on both wings over a range of reduced pitch rate. Moreover, consistent with the observation that, at high reduced pitch rates the effect of the downwash is diminished

(see Chapter 5) the two curves at 57% and 68% of the span move closer together as the reduced pitch rates increases. In fact, at 68% of the span the S^+ peak occurs earlier on the rectangular wing at the highest pitch rates.

Chapter 8

Vortex Convection

It emerges so far that dynamic stall is characterized by the generation near the leading edge of a powerful vortex structure whose growth and subsequent convection is accompanied by a rise in the normal force coefficient CN and a break in the pitching moment coefficient Cm. The footprint of the vortex is clearly visible in the plots of the chordal Cp distribution versus time, for ramp-up cases, where it appears as a disturbance peak near the leading edge, Figures (4.1 - 4.4). In these plots the progression of this disturbance toward the trailing edge, which corresponds to the passage of the vortex over the aerofoil, is also visible. This, in turn, influences the normal force coefficient and the behaviour of the pitching moment coefficient which reaches its minimum value when the vortex passes over the trailing edge, Figure 8.1. The timing of these events, therefore, depends upon the convection speed of the stall vortex.

The phenomenon of vortex instability and, in particular, the reason why the dynamic stall vortex starts moving is a complex problem and clearly factors triggered by viscous effects play a key role. As yet, there is no entirely satisfactory theoretical description of this phenomenon. At best, the existing theories of waves on vortices

have provided useful insights into weakly non-linear motion but cannot be the basis of generalized theory, [25, 27, 69, 70, 87]. Consideration of 'bending waves' may however provide further insight into the evolution of vortex instabilities [70, 55, 86], and may provide a means of rationalizing the initiation of convection of the dynamic stall vortex.

The purpose of this section is not to investigate the causes of the convection process, but rather to examine the behaviour of the vortex motion over the aerodynamic surfaces of both the two-dimensional and three-dimensional models and then to consider the convection speed as a function of the reduced pitch rate. The result of this investigation will be compared with previous measurements of convection speed.

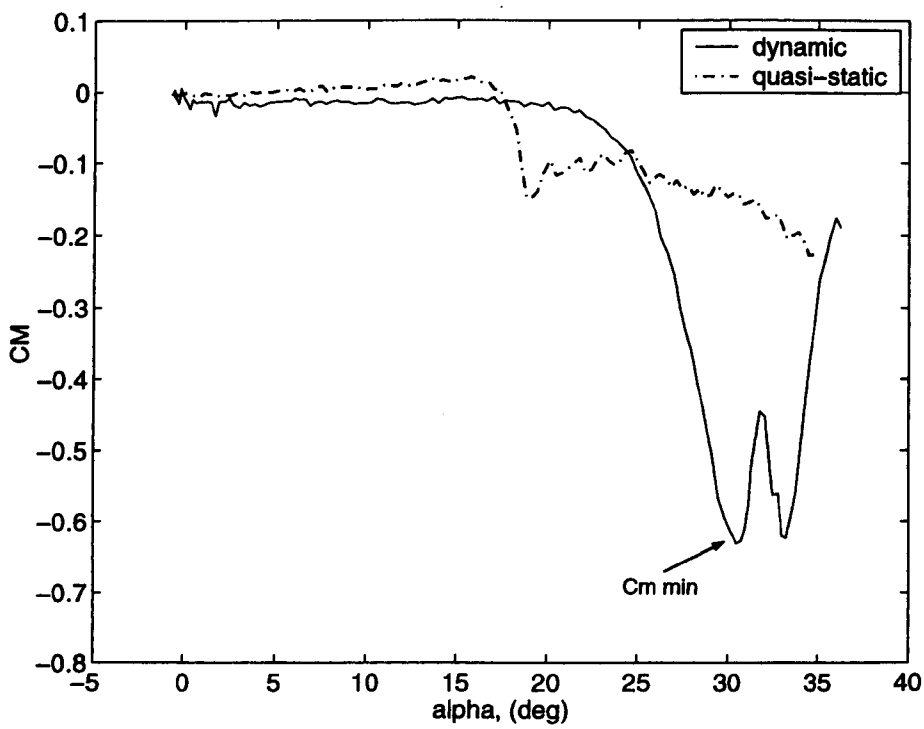

Figure 8.1: Pitching moment coefficient Cm around 25% of the aerofoil chord versus incidence.

8.1 Vortex Convection

Previous analysis of the influence of the reduced pitch rate on the timing of the formation of the dynamic stall vortex, has demonstrated that the onset of the vortex and its convection are progressively delayed to higher angles of incidence as the pitch rate increases (see Chapter4). Thus, for very high values of the pitch rate, convection starts at incidences close to 40 *deg*. Because of this, the ramp-up tests include a holding period at the maximum incidence. The pressure data recorded during this holding period show that the movement of the vortex along the chord is not influenced by the motion of the aerofoil.

There are several possible ways of identifying the passage of the vortex over the aerofoil chord and calculating its convection speed using pressure data. One of them is based on examination of contour plots of the unsteady chordal pressure distributions, [11]. This method is an effective way of determining the main qualitative features of vortex convection but does not give accurate quantitative estimates of convection speed. Figure 8.2 shows pressure contour plots for the 57%, 68% and 80% of span locations on the rectangular wing and for a reduced pitch rate of 0.0271. The movement of the vortex at 57% span is indicated by a well defined suction ridge which is marked in Figure 8.2 by a superimposed straight line. At 57%, 68% and 80% of span, the convection of the vortex is well defined and distinct over the second half of the chord, albeit there is a clear weakening of the ridge as the distance from the mid-span increases. The vortex system apparently leaves the wing's trailing edge at almost the same time regardless of span location. Moreover, examination of the pressure contours for several reduced pitch rates suggests that this behaviour is common to all pitch rates. Clearly, however, the gradients of the superimposed lines in the three plots are not the same. This suggests that the timing of the initiation of vortex convection is not the same at each span location if the convection speed

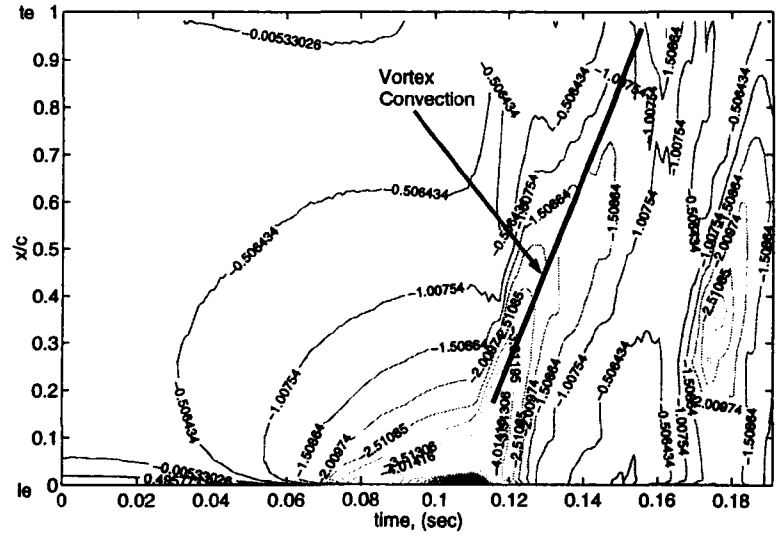

(a) 57% span

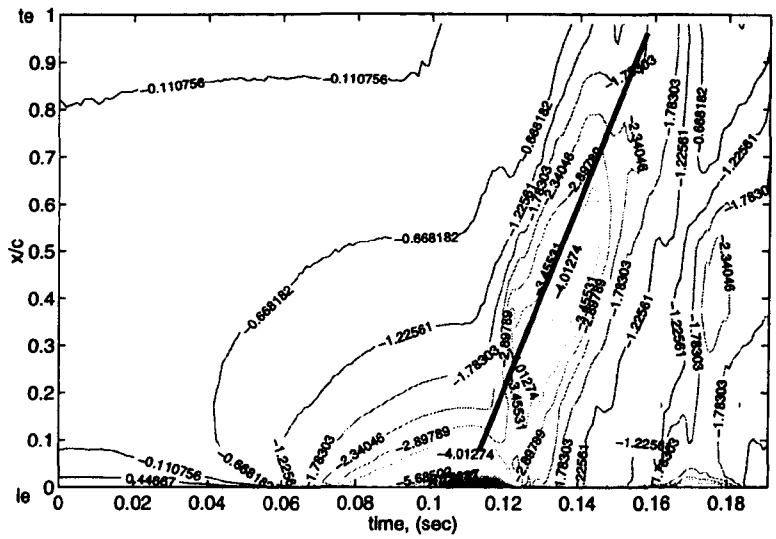

(b) 68% span

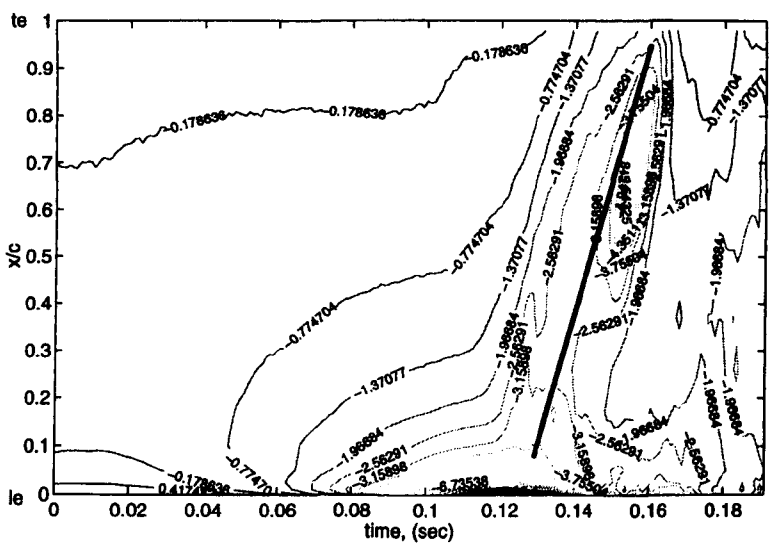

(b) 80% span

Figure 8.2: Pressure coefficient contours plotted in space and time at three span locations of the rectangular wing at reduced pitch rate 0.0271.

does not vary along the chord.

This method of analysis is not ideal since it is not easy to identify the chordal location at which the vortex develops or to obtain precise measurements of convection speed. As shown in Figure 8.2, a straight line can be drawn through the suction ridge associated with the vortex and can be used to determine the vortex speed. The difficulty in locating both the chordal location of vortex development near the leading edge and the last instant before it leaves the surface does, however, make it difficult to obtain accurate estimates of the vortex speed.

An alternative way of studying vortex convection is to pinpoint the timing of the maximum suction on the vortex ridge at each transducer along the chord. This approach was first described by Lorber and Carta [82] and has been adopted in this work because it is more accurate and provides more detailed information on the convection process. Figure 8.3 depicts the method schematically.

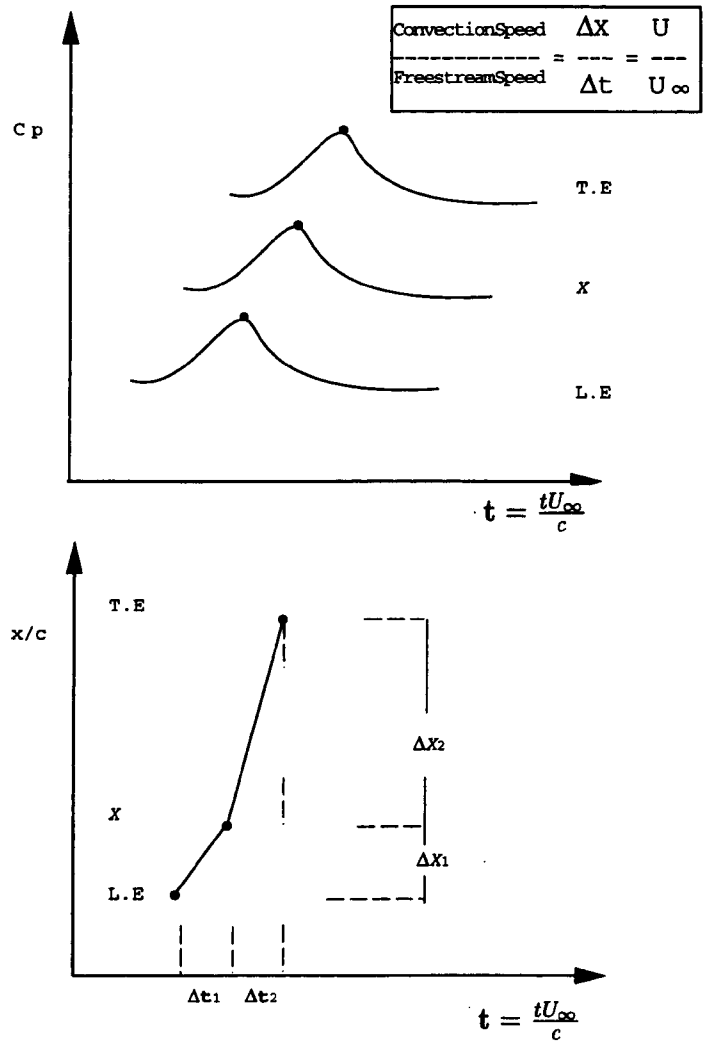

Figure 8.3: Chordwise propagation of a pressure wave.

The upper portion of Figure 8.3 is an idealized sketch of the pressure time history showing chordwise propagation of the ridge associated with the vortex. The event begins near the leading edge at time t_o and reaches a chordwise station X after an interval Δt. The lower portion of the figure shows two segments connecting the maximum peaks of the suction ridge. The intervals Δt_1 and Δt_2 represent the times required for the suction ridge to travel the distances ΔX_1 and ΔX_2. The gradient of each single segment is then the local convection speed of the ridge.

Assuming the chordwise station X normalized with respect to the chord of the model ($X = \frac{X}{c}$) and the time t normalized with respect the freestream speed and the chord model ($\mathbf{t} = \frac{tU_\infty}{c}$) the dimensionless convection speed is given by the following relation (8.1):

$$\frac{ConvectionSpeed}{FreestreamSpeed} = \frac{\Delta X}{\Delta \mathbf{t}} = \frac{U}{U_\infty} \tag{8.1}$$

The mathematical average of the local velocities gives the average convection velocity of the vortex.

It is necessary to identify the location at which the vortex forms before attempting to calculate its convection speed. In this respect, the temporal chordal Cp distribution plots presented earlier in Figures 4.1 - 4.4 provide some information about the vortex system on the wing. As previously discussed, the vortex is associated with a suction ridge which moves from around the quarter chord location to the trailing edge. This disturbance shows up earlier at 57% of span and is also closer to the leading edge there than at 68% and 80% of span. Nevertheless, for the calculation of convection speed it is reasonable to assume that the vortex system starts its rearward movement from the quarter chord location at all span positions on the wing.

It should be noted that the suction ridge produced by the vortex is not well defined at 80% of span, especially at low reduced pitch rates. This is a consequence of the vortex being weaker and increases the uncertainty in the calculated convection speed of the vortex of this location.

8.2 Convection Speed

Figures 8.4a, b and c show plots of the pressure coefficient versus time for transducers on the upper surface at 57%, 68% and 80% of span on the rectangular wing. In Figure 8.4 a dotted line connects the locations of the second peak located behind the leading edge suction peak that is associated with the presence of the vortex.

By measuring the timing of this peak at each transducer position, the passage of the stall vortex along the chord can be traced. In Figure 8.4c corresponding to 80% of the wing span, the peak associated with the dynamic stall vortex cannot be located without a wide margin of error. Thus, in the following study, the estimation of the convection speed at this span position is omitted. On the basis of the qualitative information from the contour analysis, it would appear that vortex convection at 80% of span is faster than at the other two more inboard sections.

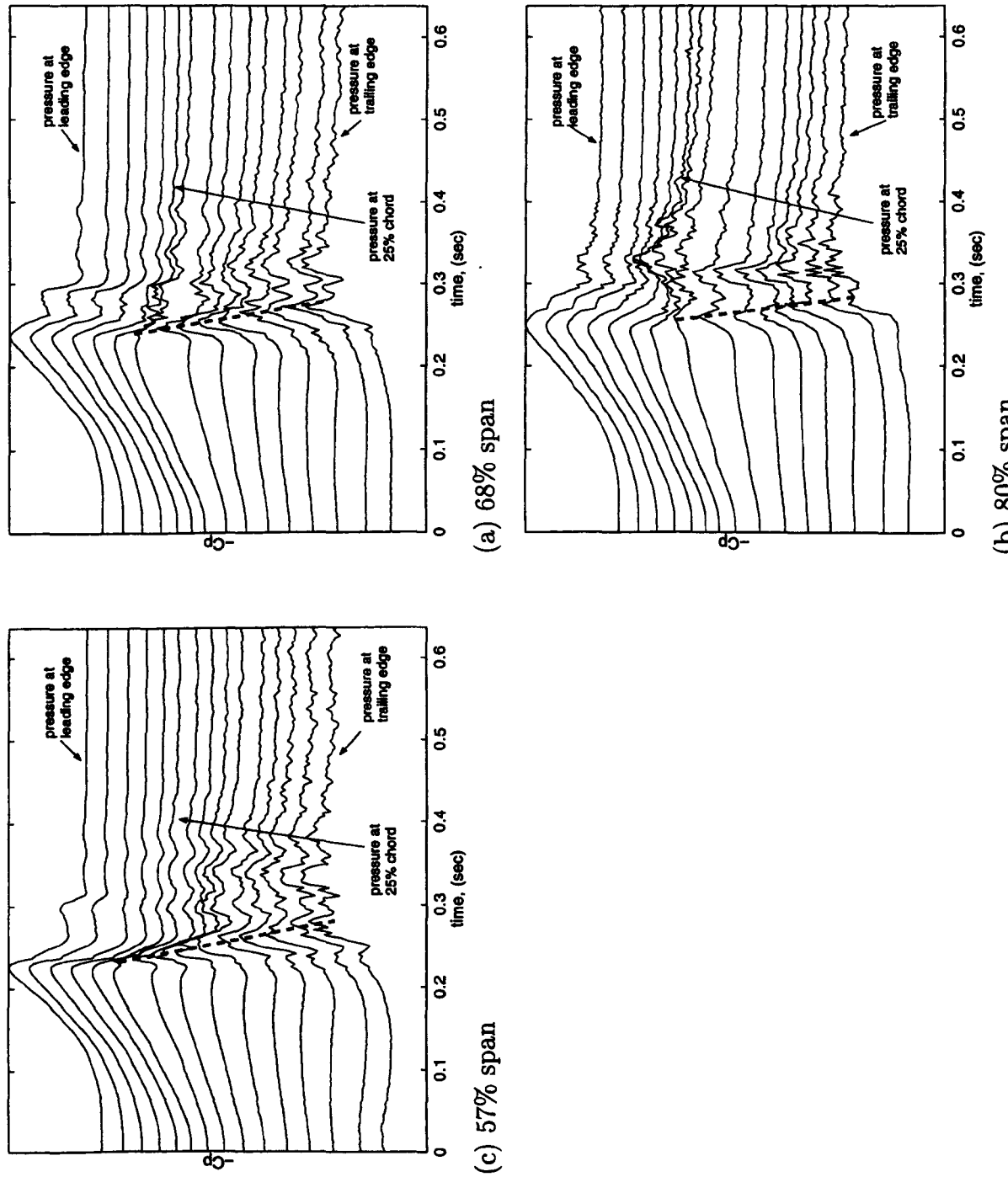

Figure 8.4: Suction peak associated with the convection of the dynamic stall vortex for the rectangular wing at a reduced pitch rate of 0.097.

Figure 8.5 shows the stall vortex movement along the chord of the nominally two-dimensional NACA 0015 aerofoil model and along the chord at two span positions of the rectangular wing at reduced pitch rate 0.023.

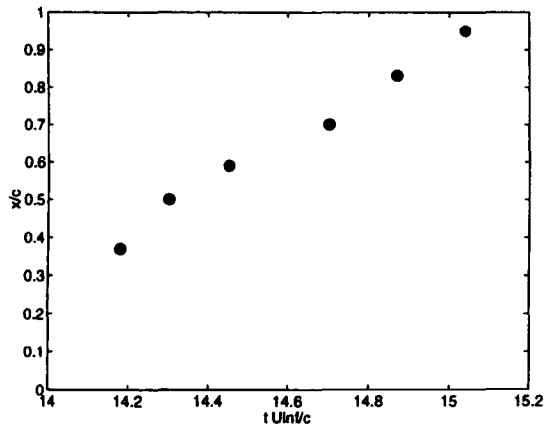

(a) NACA 0015 Aerofoil

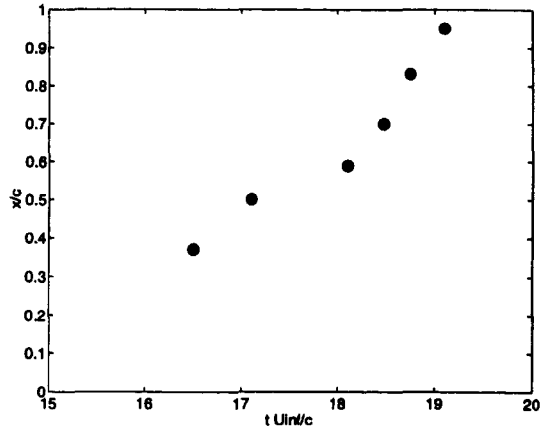

(b) 57% span

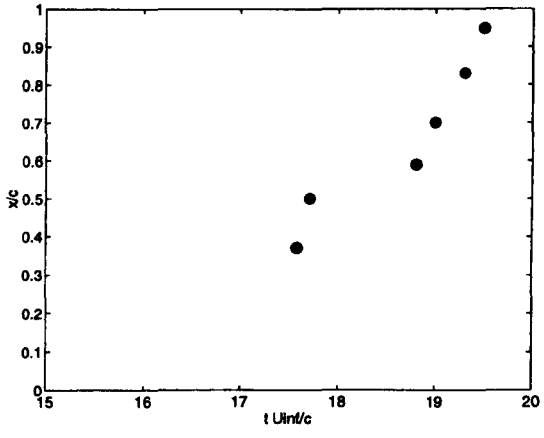

(c) 68% span

Figure 8.5: Stall vortex position versus time for the two-dimensional NACA 0015 aerofoil and two span locations on the rectangular wing at reduced pitch rate of 0.023.

The vortex apparently moves almost linearly across the chord of the nominally two-dimensional aerofoil but behaves differently in the three dimensional case by slowing

down near the midchord at both span locations. This was observed during the visualization tests and it occurs when the three-dimensional vortex structure changes its shape into the 'omega' profile. The last two graphs also show that the convection is not concurrent along the span and, in fact, is delayed at the more outboard section of the span. Therefore, since the contour analysis suggests the simultaneous passage of the vortex over the trailing edge, faster convection of the vortex at outboard locations may be expected.

On the basis of these measurements, it is possible to estimate the average convection speed of the vortex. The average convection speed is plotted in Figure 8.6 as a function of reduced pitch rate for the two span positions on the rectangular wing and for the nominally two-dimensional NACA 0015 aerofoil.

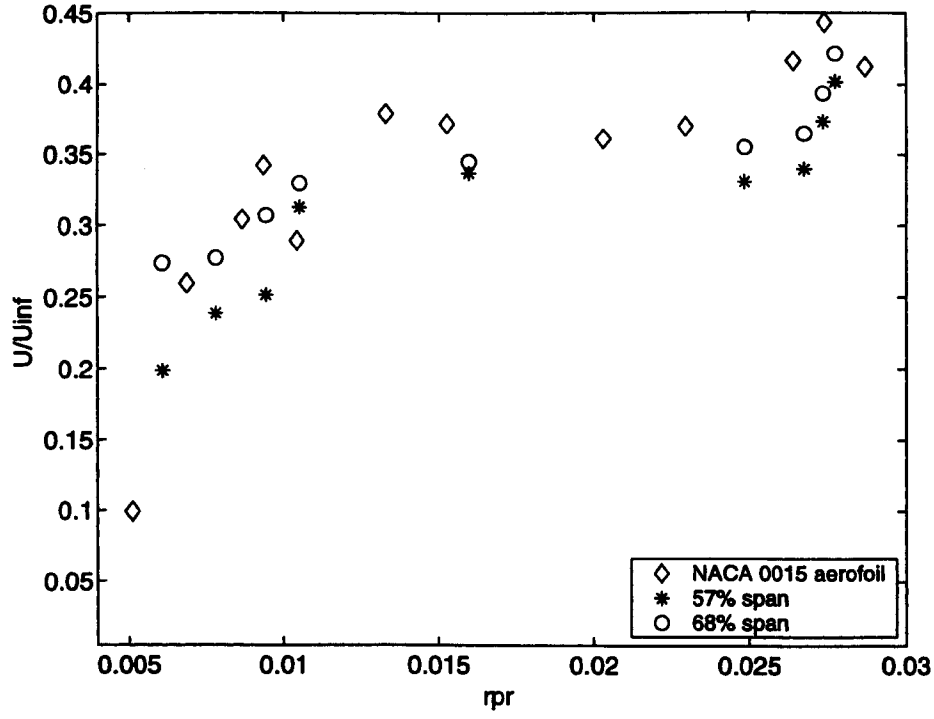

Figure 8.6: Vortex Convection speed versus reduced pitch rate for the rectangular wing and the two-dimensional NACA 0015 aerofoil.

The graph indicates that the convection speed for all test models analyzed in this work is dependent on the reduced pitch rate and its value is lower than the freestream velocity. In addition, on the rectangular wing, the higher value of the convection speed at 68% of span highlights the suggested variation in convection speed along the wing span. The slower passage of the vortex near the mid-span is associated with the 'Omega' shape (see Figure 3.1c) that the vortex forms above the wing. The sense of rotation of the vorticity in the vertical legs of the 'Omega' has a twofold effect. It induces a slow-down of the vortex convection at inner sections of the span and encourages convection of the outboard vortex sections. The net effect which the complex three-dimensional vortex structure has, is to produce local convection speeds that are lower than those in the two-dimensional case as illustrated by Figure 8.6.

The corresponding analysis at 57% and 68% of span of the swept tip wing shows that the vortex exhibits essentially the same convective behaviour as that on the rectangular wing, Figure 8.7. The local convection speed at 57% of span of the swept-tip wing appears to be slower than the speed at the corresponding span station of the rectangular wing. This behaviour finds explanation in the 'Omega' vortex structure whose shape is affected by the wing geometry and, then, by the wing tips. In fact, from the flow visualization [100] it emerged that the 'legs' of the 'Omega' shape are closer together around the mid-span of the swept-tip wing and characterized by a higher rotational speed, Figure 5.1. Consequently the twofold action due to the vertical legs is more effective on the swept-tip wing and causes a slower convection of the vortex at 57% of span and higher at 68% of span of the swept-tip wing.

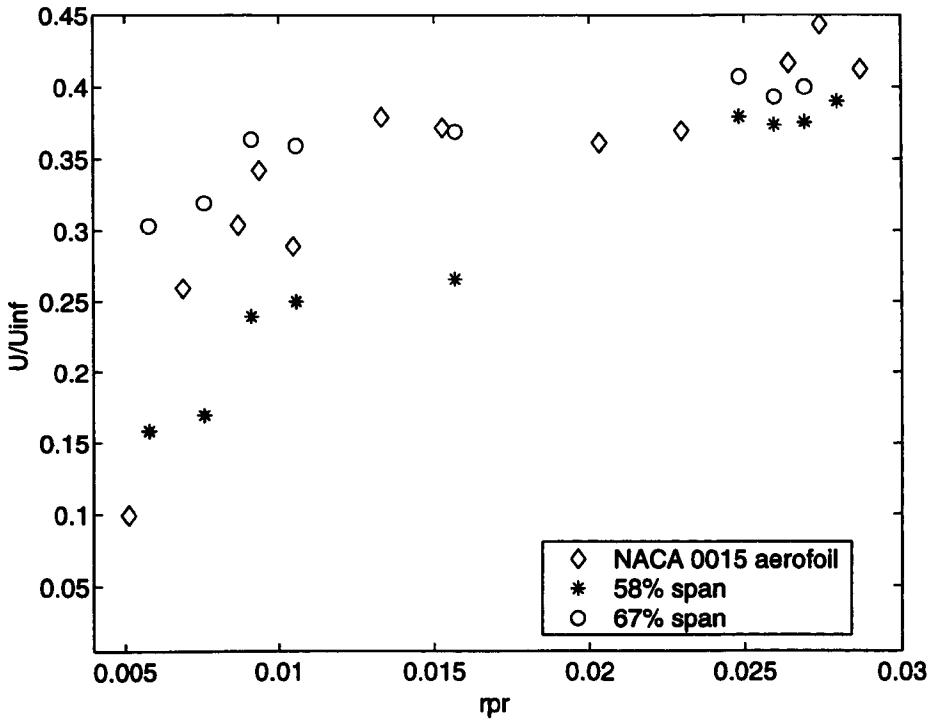

Figure 8.7: Convection speed versus reduced pitch rate for the 60^0 swept tips wing and the nominally two-dimensional NACA 0015 aerofoil.

8.3 Discussion of Vortex Convection

The analysis has shown that the stall vortex convection speed is dependent on aerofoil motion. This conclusion is apparently in disagreement with that of Green, [50] but is compatible with that of Lorber and Carta, [82]. Before examining this result, a brief resume of previous measurements will benefit the reader.

The convection speed has been measured by various researchers who have made alternative conclusions relative to the dependency of the convection speed upon the aerofoil motion. Some authors such as Carta, [11], St. Hilaire and Carta [122], Robinson and Luttges [110] reported a strong dependency of the dynamic stall duration on the reduced pitch rate. A conflicting verdict was concluded by Jumper, [64]

who found the convection speed constant at $0.4U_\infty$; Chandrasekhara and Carr [14] and Tuncer et al. [125] estimated the convection speed was constant at $0.3U_\infty$. In addition to the above authors, Galbraith et al. [40] concluded that the stall vortex convection speed is independent of the aerofoil motion to a first order and estimated it to be constant somewhere between $0.32U_\infty$ - $0.36U_\infty$. The achievement of a single overall conclusion is complicated because the results presented by these authors do not cover the same test conditions such as Mach and Reynolds numbers, aerofoil shapes, test motions and, moreover the techniques adopted for estimating the convection speed were not the same. Subsequently, Green at al. [50] carried out a comparison of their data with those of Lorber and Carta [82] because the test conditions in the two cases were well matched. Green at al. concluded that differences in the method of estimating the convection speed were not the cause of the anomaly between two data sets. Further they suggested that the different aerofoil types may experience different vortex development and convection behaviour.

The experimental data presented in this work were obtained for ramp-up tests in an aerodynamic environment similar to the tests of Lorber-Carta [82] and Green et al. [50]. Lorber and Carta performed their ramp-up tests on a SSC-A09 aerofoil at low reduced pitch rates ($0.001 < rpr < 0.02$) in compressible flow and at a Reynolds number of the order of 10^6. For these test conditions, they suggested that the tendency is for the convection speed to be motion dependent. This conclusion is in general agreement with the results of the current work for the nominally two-dimensional NACA 0015 aerofoil in similar test conditions. Further, the current analysis shows that the convection speed rises from 35% to 40% of the freestream velocity over the reduced pitch rate range 0.015 to 0.03, Figure 8.6. This is also in good agreement with the analysis conducted by Green [50] on the same aerofoil for the same range of reduced pitch rates.

Chapter 9

Conclusions and Final Remarks

From this study it has emerged that the origins of the dynamic stall vortex on a pitching aerofoil are associated with the presence of a 'dipole' of vorticity distributed around the nose on the upper and lower surfaces. The behaviour of the source of vorticity on the lower surface seems to be directly linked to the initial formation of the stall vortex whereas the sink of vorticity on the upper surface appears to be responsible for the vorticity channelled into the dynamic stall vortex during its growth. A detailed analysis of the vorticity flux in the vicinity of the leading edge has shown that the 'vorticity-source' reaches its greatest magnitude at the same time the vorticity cluster on the upper surface begins to form into the dynamic stall vortex. This result suggests that monitoring the vorticity flux may provide a method of detecting incipient stall. It may also provide an opportunity to develop an alternative stall onset criterion. This will not be straightforward and the approach will be limited to quasi two-dimensional flows since the present work has also established that dynamic stall vortex formation in a strong three-dimensional flow differs significantly from the nominally two-dimensional case.

Previous flow visualization results [100], [66] showed good correspondence between

the behaviour of the main three vortex structures (shear layer vortex, tip vortex and dynamic stall vortex) over the finite wings and a nominally two-dimensional NACA 0015 aerofoil. A detailed analysis of the chordwise pressure and normal force coefficients during pitching, however, demonstrated that there are significant differences between the two- and three-dimensional cases. In particular, the dynamic stall vortex structures on the finite wings evolve in a complex manner. The dynamic stall vortex initially develops at the leading edge region near the mid-span and rapidly extends to the outboard sections of the wing. Once the vortex structure has developed, it grows rapidly and begins to convect toward the trailing edge. As it does so, it evolves into a complex three-dimensional geometry. Moreover, the dynamic stall vortex on both wings first appears at a higher incidence than on the two dimensional aerofoil. This effect is predominantly due to the influence of the wing tip-vortices that induces the effect commonly known as downwash. The downwash effect is also responsible of the weaker and less abrupt stall on the finite wings than on the nominally two-dimensional NACA 0015 aerofoil as the curves of normal force coefficient versus angle of attack show.

The three main vortex structures that develop on the two finite wings are generally similar in form. Because of the different geometry, there are, however, some significant differences in the manner in which these vortex structures evolve on the two wings. In particular, on the swept-tip wing the tip-vortices are larger and wider such that they directly influence a greater portion of the wing span. Consequently, the effect of downwash across the swept-tip wing should be more pronounced than on the rectangular wing planform. A consequence of this is that the curve of the normal force coefficient versus angle of attack over the swept-tip wing exhibits smaller values, a smoother gradient and more rounded peaks than on the rectangular wing. Thus, it may be concluded that the dynamic stall process is less abrupt.

The vorticity flux analysis of the sectional response on the two finite wings and the nominally two-dimensional NACA 0015 aerofoil has identified the leading edge response as being an important factor in the mechanism that triggers the stall. A comparative study of the vorticity flux behaviour at the leading edge with an alternative leading edge stall criterion due to Evans and Mort [26], however, established that the onset of the dynamic stall vortex at more outboard sections of the finite wings is not triggered by the leading edge but rather is associated with the propagation of the disturbance to the local vorticity field by the formation of the vortex at the mid-span. So, it is concluded that the formation of the dynamic stall vortex at the mid-span is the triggering mechanism for vortex formation outboard. This conclusion implies that dynamic stall on three-dimensional wings cannot be accurately predicted using the conventional approach of a lifting line vortex wakes model coupled with a two-dimensional sectional solver [123] as such a technique would not capture the propagation mechanism. Whilst such a method will predict the response reasonably well in regimes where the flow is nominally two-dimensional, towards the wing tip it will provide inaccurate estimates of the onset of stall and the subsequent timing of vortex passage across the chord. This will result in poor estimates of blade loads during stall.

On the basis of the conclusions outlined above it is clear that further work is required to examine the vorticity flux behaviour in three-dimensions to establish and overcome the limitations of the two-dimensional assumption used in the present study. Once these limits are pointed out, further work is required to investigate the vortex disturbance propagation mechanism in order to develop alternative three-dimensional stall onset criteria that take into account the vorticity flux.

Appendix A

Ramp-Up Test List and Transducers Coordinates

NACA 0015 Aerofoil (2D)			Rectangular Wing			Swept-Tip Wing		
$\dot{\alpha}$	rpr	$10^6 Re_c$	$\dot{\alpha}$	rpr	$10^6 Re_c$	$\dot{\alpha}$	rpr	$10^6 Re_c$
29.701	0.0034	1.47	45.202	0.0029	1.49	44.902	0.0029	1.50
44.173	0.0051	1.47	67.567	0.0044	1.48	88.909	0.0058	1.52
59.461	0.0068	1.48	91.155	0.0059	1.48	116.322	0.0076	1.52
74.985	0.0087	1.47	117.472	0.0080	1.47	139.936	0.0091	1.51
90.423	0.0104	1.47	142.638	0.0096	1.49	157.540	0.0105	1.51
100.871	0.0116	1.47	160.243	0.0108	1.48	178.789	0.0120	1.52
115.182	0.0133	1.47	183.256	0.0120	1.48	190.356	0.0130	1.52
129.539	0.0153	1.48	198.245	0.0130	1.49	203.251	0.0130	1.51
146.172	0.0172	1.47	214.767	0.0140	1.49	234.355	0.0156	1.51
158.971	0.0187	1.47	248.981	0.0165	1.48	266.060	0.0169	1.53
173.022	0.0203	1.47	280.956	0.0190	1.48	302.694	0.0201	1.53
184.701	0.0217	1.47	311.856	0.0210	1.49	331.920	0.0217	1.52
195.441	0.0230	1.47	335.167	0.0220	1.48	336.802	0.0220	1.52
205.788	0.0242	1.46	353.155	0.0240	1.48	360.767	0.0230	1.52
225.111	0.0264	1.46	366.563	0.0245	1.48	387.356	0.0248	1.51
234.455	0.0274	1.47	404.442	0.0266	1.47	404.252	0.0259	1.50
245.874	0.0287	1.47	414.286	0.0273	1.48	419.047	0.0269	1.52
259.111	0.0302	1.47	416.944	0.0271	1.48	437.394	0.0279	1.51
Ramp:	-1.0^0	$\sim 41.0^0$	Ramp:	-5.0^0	$\sim 39.0^0$	Ramp:	-1.5^0	$\sim 43.5^0$

Table A.1: Complete list of ramp-up tests. Mach number around 0.12 and 0.16 correspond to two- and three-dimensional tests.

$TransducerNo$	x/c	y/c	z/c
1	0.9800	0.00504	-0.2143
2	0.9500	0.01008	-0.2143
3	0.8300	0.02856	-0.2143
4	0.7000	0.04580	-0.2143
5	0.5900	0.05806	-0.2143
6	0.5000	0.06618	-0.2143
7	0.3700	0.07376	-0.2143
8	0.2600	0.07454	-0.2143
9	0.1700	0.06911	-0.2143
10	0.1000	0.05854	-0.2143
11	0.0500	0.04443	-0.2143
12	0.0250	0.03268	-0.2143
13	0.0100	0.02129	-0.2143
14	0.0025	0.01089	-0.2143
15	0.00025	0.0035	-0.2143
16	0.00025	-0.0035	-0.2143
17	0.0025	-0.01089	-0.2143
18	0.0100	-0.02129	-0.2143
19	0.0250	-0.03268	-0.2143
20	0.0500	-0.04443	-0.2143
21	0.1000	-0.05854	-0.2143
22	0.1850	-0.07053	-0.2143
23	0.2600	-0.07454	-0.2143
24	0.3550	-0.07422	-0.2143
25	0.4900	-0.06695	-0.2143
26	0.5900	-0.05806	-0.2143
27	0.7000	-0.04580	-0.2143
28	0.8350	-0.02784	-0.2143
29	0.9500	-0.01008	-0.2143
30	0.9800	-0.00504	-0.2143

Table A.2: Coordinates of the transducers along the chord, NACA 0015 aerofoil

Transducer No			x/c	y/c	z/c		
57%	68%	80%			57%	68%	80%
01	31	61	0.9800	0.00504	-0.21428	-0.54524	-0.9
02	32	62	0.9500	0.01008	-0.21428	-0.54524	-0.9
03	33	63	0.8300	0.02856	-0.21428	-0.54524	-0.9
04	34	64	0.7000	0.04580	-0.21428	-0.54524	-0.9
05	35	65	0.5900	0.05806	-0.21428	-0.54524	-0.9
06	36	66	0.5000	0.06618	-0.21428	-0.54524	-0.9
07	37	67	0.3700	0.07376	-0.21428	-0.54524	-0.9
08	38	68	0.2600	0.07454	-0.21428	-0.54524	-1.9
09	39	69	0.1700	0.06911	-0.21428	-0.54524	-0.9
10	40	70	0.1000	0.05854	-0.21428	-0.54524	-0.9
11	41	71	0.0500	0.04443	-0.21428	-0.54524	-0.9
12	42	72	0.0250	0.03268	-0.21428	-0.54524	-0.9
13	43	73	0.0100	0.02129	-0.21428	-0.54524	-0.9
14	44	74	0.0025	0.01089	-0.21428	-0.54524	-0.9
15	45	75	0.00025	0.0035	-0.21428	-0.54524	-0.9
16	46	76	0.00020	-0.0035	-0.21428	-0.54524	-0.9
17	47	77	0.0025	-0.01089	-0.21428	-0.54524	-0.9
18	48	78	0.0100	-0.02129	-0.21428	-0.54524	-0.9
19	49	79	0.0250	-0.03268	-0.21428	-0.54524	-0.9
20	50	80	0.0500	-0.04443	-0.21428	-0.54524	-0.9
21	51	81	0.1000	-0.05854	-0.21428	-0.54524	-0.9
22	52	82	0.1850	-0.07053	-0.21428	-0.54524	-0.9
23	53	83	0.2600	-0.07454	-0.21428	-0.54524	-0.9
24	54	84	0.3550	-0.07422	-0.21428	-0.54524	-0.9
25	55	85	0.4900	-0.06695	-0.21428	-0.54524	-1.9
26	56	86	0.5900	-0.05806	-0.21428	-0.54524	-0.9
27	57	87	0.7000	-0.04580	-0.21428	-0.54524	-0.9
28	58	88	0.8350	-0.02784	-0.21428	-0.54524	-0.9
29	59	89	0.9500	-0.01008	-0.21428	-0.54524	-0.9
30	60	90	0.9800	-0.00504	-0.21428	-0.54524	-0.9

Table A.3: Coordinates of the transducers at 57%, 68%, 80% of the span on the rectangular wing. The x coordinate along the chord and y coordinate perpendicular to the chord are the same at all span-wise sections.

Transducer No			x/c	y/c	z/c		
90%	95%	97%			90%	95%	97%
91	121	151	0.9800	0.00504	-1.2	-1.3381	-1.4157
92	122	152	0.9500	0.01008	-1.2	-1.3381	-1.4157
93	123	153	0.8300	0.02856	-1.2	-1.3381	-1.4157
94	124	154	0.7000	0.04580	-1.2	-1.3381	-1.4157
95	125	155	0.5900	0.05806	-1.2	-1.3381	-1.4157
96	126	156	0.5000	0.06618	-1.2	-1.3381	-1.4157
97	127	157	0.3700	0.07376	-1.2	-1.3381	-1.4157
98	128	158	0.2600	0.07454	-1.2	-1.3381	-1.4157
99	129	159	0.1700	0.06911	-1.2	-1.3381	-1.4157
100	130	160	0.1000	0.05854	-1.2	-1.3381	-1.4157
101	131	161	0.0500	0.04443	-1.2	-1.3381	-1.4157
102	132	162	0.0250	0.03268	-1.2	-1.3381	-1.4157
103	133	163	0.0100	0.02129	-1.2	-1.3381	-1.4157
104	134	164	0.0025	0.01089	-1.2	-1.3381	-1.4157
105	135	165	0.00025	0.0035	-1.2	-1.3381	-1.4157
106	136	166	0.00025	-0.0035	-1.2	-1.3381	-1.4157
107	137	167	0.0025	-0.01089	-1.2	-1.3381	-1.4157
108	138	168	0.0100	-0.02129	-1.2	-1.3381	-1.4157
109	139	169	0.0250	-0.03268	-1.2	-1.3381	-1.4157
110	140	170	0.0500	-0.04443	-1.2	-1.3381	-1.4157
111	141	171	0.1000	-0.05854	-1.2	-1.3381	-1.4157
112	142	172	0.1850	-0.07051	-1.2	-1.3381	-1.4157
113	143	173	0.2600	-0.07454	-1.2	-1.3381	-1.4157
114	144	174	0.3550	-0.07422	-1.2	-1.3381	-1.4157
115	145	175	0.4900	-0.06695	-1.2	-1.3381	-1.4157
116	146	176	0.5900	-0.05806	-1.2	-1.3381	-1.4157
117	147	177	0.7000	-0.04580	-1.2	-1.3381	-1.4157
118	148	178	0.8350	-0.02784	-1.2	-1.3381	-1.4157
119	149	179	0.9500	-0.01008	-1.2	-1.3381	-1.4157
120	150	180	0.9800	-0.00504	-1.2	-1.3381	-1.4157

Table A.4: Coordinates of the transducers at 57%, 68%, 80% on the span of the rectangular wing. The x coordinate along the chord and y coordinate perpendicular to the chord are the same at all span-wise sections.

Transducer No	x/c	y/c	z/c
181	0.1700	0.06911	-1.2690
182	0.3700	0.07376	-1.2690
183	0.5900	0.05806	-1.2690
184	0.8300	0.02856	-1.2690
185	0.3700	0.07376	-1.1000
186	0.5900	0.05806	-1.1000
187	0.8300	0.02856	-1.1000
188	0.5900	0.05806	-1.0000
189	0.8300	0.02856	-1.0000
190	0.8300	0.02856	-0.8286
191	0.5000	0.06618	0.4500
192	0.1000	0.05854	1.2000

Table A.5: Coordinates of the transducers in the region of the wing tip of the rectangular wing.

Transducer No				x/c	y/c	z/c			
58%	67%	75%	80%			58%	67%	75%	80%
01	30	59	-	0.00025	0.0035	-0.21428	-0.45238	-0.66429	-0.85121
02	31	60	-	0.0025	0.01089	-0.21428	-0.45238	-0.66429	-0.85121
03	32	61	-	0.0100	0.02129	-0.21428	-0.45238	-0.66429	-0.85121
04	33	62	-	0.0250	0.03268	-0.21428	-0.45238	-0.66429	-0.85121
05	34	63	88	0.0500	0.04443	-0.21428	-0.45238	-0.66429	-0.85121
06	35	64	89	0.1000	0.05854	-0.21428	-0.45238	-0.66429	-0.85121
07	36	65	90	0.1700	0.06911	-0.21428	-0.45238	-0.66429	-0.85121
08	37	66	91	0.2600	0.07454	-0.21428	-0.45238	-0.66429	-0.85121
09	38	67	92	0.3700	0.07376	-0.21428	-0.45238	-0.66429	-0.85121
10	39	68	93	0.5000	0.06618	-0.21428	-0.45238	-0.66429	-0.85121
11	40	69	94	0.5900	0.05806	-0.21428	-0.45238	-0.66429	-0.85121
12	41	70	95	0.7000	0.04580	-0.21428	-0.45238	-0.66429	-0.85121
13	21	71	96	0.8300	0.02856	-0.21428	-0.45238	-0.66429	-0.85121
14	43	72	97	0.9286	0.01424	-0.21428	-0.45238	-0.66429	-0.85121
15	44	73	98	0.9800	0.00504	-0.21428	-0.45238	-0.66429	-0.85121
16	45	74	99	0.9800	-0.00504	-0.21428	-0.45238	-0.66429	-0.85121
17	46	75	100	0.9286	-0.01423	-0.21428	-0.45238	-0.66429	-0.85121
18	47	76	101	0.8350	-0.02784	-0.21428	-0.45238	-0.66429	-0.85121
19	48	77	102	0.7000	-0.04580	-0.21428	-0.45238	-0.66429	-0.85121
20	49	78	103	0.5900	-0.05806	-0.21428	-0.45238	-0.66429	-0.85121
21	50	79	104	0.4900	-0.06695	-0.21428	-0.45238	-0.66429	-0.85121
22	51	80	105	0.3550	-0.07422	-0.21428	-0.45238	-0.66429	-0.85121
23	52	81	106	0.2600	-0.07454	-0.21428	-0.45238	-0.66429	-0.85121
24	53	82	107	0.1850	-0.07053	-0.21428	-0.45238	-0.66429	-0.85121
25	54	83	108	0.1000	-0.05854	-0.21428	-0.45238	-0.66429	-0.85121
26	55	84	109	0.0500	-0.04443	-0.21428	-0.45238	-0.66429	-0.85121
27	56	85	-	0.0250	-0.03268	-0.21428	-0.45238	-0.66429	-0.85121
28	57	86	-	0.0100	-0.02129	-0.21428	-0.45238	-0.66429	-0.85121
29	58	87	-	0.0025	-0.01089	-0.21428	-0.45238	-0.66429	-0.85121

Table A.6: Coordinates of the transducers at 57%, 68%, 80% on the span of the swept-tip wing. The x coordinate along the chord and y coordinate perpendicular to the chord are the same at all span-wise sections.

Transducer No	x/c	y/c	z/c
110	0.9800	0.00504	-0.96431
111	0.9286	0.01423	-0.95836
112	0.8300	0.02856	-0.94764
113	0.7000	0.04580	-0.93514
114	0.5900	0.05806	-0.92383
115	0.5000	0.06464	-0.91490
116	0.3700	0.06700	-0.90121
117	0.2600	0.06188	-0.88871
118	0.9800	-0.00519	-0.96550
119	0.9286	-0.01410	-0.95955
120	0.8350	-0.02840	-0.94943
121	0.7000	-0.04686	-0.93514
122	0.5900	-0.05888	-0.92264
123	0.1850	-0.05267	-0.89169
124	0.9800	0.00504	-1.04883
125	0.9286	0.01423	-1.03931
126	0.7000	0.04593	-0.99764
127	0.5900	0.05676	-0.97562
128	0.5000	0.06179	-0.95895
129	0.3700	0.06226	-0.93514
130	0.1700	0.04524	-0.89169
131	0.9800	-0.00519	-1.11967
132	0.9286	-0.01410	-1.10612
133	0.8350	-0.02781	-1.08098
134	0.7000	-0.04576	-1.04467
135	0.5900	-0.05340	-1.04587
136	0.4900	-0.06426	-0.95419
137	0.3550	-0.06057	-0.94883
138	0.2600	-0.05740	-0.91788
139	0.1000	-0.02981	-0.88038

Table A.7: Coordinates of the transducers in the region of the tip of the swept tip wing, (1^{st} part).

Transducer No	x/c	y/c	z/c
140	0.9800	0.00504	-1.12026
141	0.9286	0.01423	-1.10717
142	0.8300	0.02838	-1.05062
143	0.7000	0.04431	-1.04764
144	0.5900	0.05367	-1.01907
145	0.5000	0.05807	-0.99526
146	0.3700	0.05460	-0.97324
147	0.2600	0.05131	-0.92979
148	0.1700	0.03440	-0.91550
149	0.1000	0.02667	-0.88219
150	0.9800	-0.00471	-1.24764
151	0.9286	-0.01267	-1.22740
152	0.8350	-0.02538	-1.19169
153	0.7000	-0.03514	-1.13812
154	0.4900	-0.05324	-1.03276
155	0.2600	-0.03657	-0.96729
156	0.1850	-0.03605	-0.92621
157	0.9800	0.00504	-1.21907
158	0.9286	0.01423	-1.17443
159	0.8300	0.02838	-1.13336
160	0.7000	0.04169	-1.09883
161	0.5900	0.04945	-1.06074
162	0.5000	0.05167	-1.03633
163	0.9800	-0.00310	-1.36074
164	0.9286	-0.00900	-1.33455
165	0.8350	-0.01745	-1.28693
166	0.7000	-0.02510	-1.21788
167	0.5900	-0.02738	-1.15836
168	0.4900	-0.02729	-1.12978
169	0.3550	-0.02550	-1.03455

Table A.8: Coordinates of the transducers in the region of the tip of the swept tip wing, (2^{nd} part).

Transducer No	x/c	y/c	z/c
170	0.9286	0.01436	-1.22621
171	0.8300	0.02633	-1.18812
172	0.7000	0.03638	-1.15717
173	0.5900	0.04479	-1.09252
174	0.3700	0.04483	-1.00538
175	0.2600	0.03814	-0.96074
176	0.9800	0.00517	-1.30657
177	0.9286	0.01369	-1.28217
178	0.8300	0.02376	-1.23752
179	0.5900	0.03776	-1.12800
180	0.5000	0.04193	-1.07624
181	0.1700	0.02240	-0.93157
182	0.1000	0.01478	-0.89645
183	0.9800	0.00486	-1.36312
184	0.9286	0.01143	-1.33693
185	0.8300	0.01845	-1.28574
186	0.7000	0.02160	-1.21788
187	0.5900	0.02574	-1.16014
188	0.5000	0.02636	-1.11371
189	0.3700	0.02329	-1.04586
190	0.2600	0.01938	-0.98752
191	0.1000	0.05854	0.21428
192	0.1000	0.03988	0.85121
193	0.8300	0.02633	1.18812

Table A.9: Coordinates of the transducers in the region of the tip of the swept tip wing, (3^{th} part).

Appendix B

Flow Visualization Set Images, Rectangular Wing

To provide a comprehensive description of the inherent three-dimensionality of the flow, it is necessary to look at the flow structure at different cross sections and from several viewing angles. Therefore, a number of images are presented which highlight the dominant features of the unsteady flow field around the pitching rectangular wing with rounded tips. The incidence profile against time is shown in Figure B.1. The flow visualization images and the corresponding analysis appeared in the internal Glasgow report [100]. The following discussion is reproduced directly with kind permission of the authors Moir and Coton.

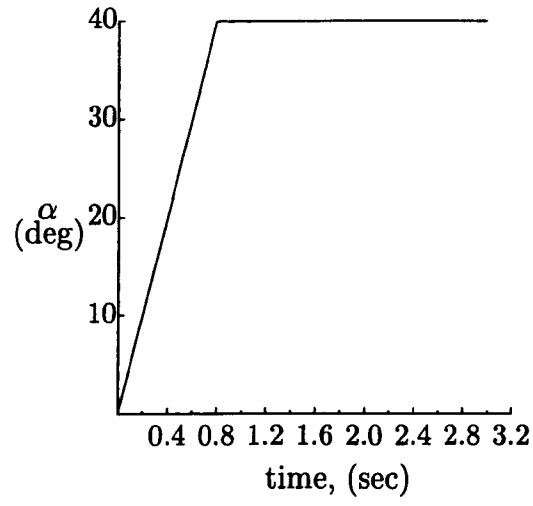

Figure B.1: Pitch incidence variation against the time for reduced pitch rate 0.08.

The Figure B.2 presents the flow field at the 57% of span location. As the model starts pitching, flow separation appears at the trailing edge. The separated flow moves forward slowly and by $t = 0.52\,s$ ($\alpha = 26^0$) *has apparently only progressed to around 60% of chord. In this frame a thin layer of reversed flow has developed over most of the upper surface and has terminated at a small disturbance near the leading edge. This disturbance grows quite rapidly and by* $t = 0.76\,s$ ($\alpha = 38^0$) *has formed into a coherent vortex structure, the dynamic stall vortex. In the meantime, behind the dynamic stall vortex the fluid within the separation zone is amalgamating into a secondary vortex system, known as the shear layer vortex. The flow field continues to develop even when the wing has stopped pitching. At* $t = 0.92\,s$ *the dynamic stall vortex, is still increasing its size, but starts to convect. By* $t = 1.0\,s$ *it has moved further towards the trailing edge and into closer proximity with the shear layer vortex. Clearly, the dynamic stall vortex is the more dominant system and, at* $t = 1.12\,s$ *it has absorbed the smaller vortex. In this frame it is also evident that the dynamic stall vortex has lifted from the wing surface and, as the images at* $t = 1.20\,s$ *and*

$t = 1.36\,s$ illustrate, this progression continues until the vortex leaves the domain of wing at around $t = 1.76\,s$.

A similar series of images corresponding to the 75% of span location is presented in Figure B.3. At very low incidences, e.g. $t = 0.76\,s$, the flow has the same basic features as that observed at 57% of span. At $t = 0.92\,s$ the general appearance of the flow is similar to its counterpart at the mid-span but there is something that is not immediately obvious. In fact, in this frame the vortex has slightly rotated out of the plane. This rotation becomes more apparent in the next image where the vortex moves closer to the shear layer vortex which has little coherence. The continued rotation is quite clear at $t = 1.12\,s$ where the vortex is tornado like in appearance but is still, apparently, tethered to its point of origin. Nevertheless, there is a clear rearwards progression of the main body of the vortex system and at $t = 1.36\,s$ it has almost reached the trailing edge. Thereafter the vortex convects toward the trailing edge, dissipating until it can no longer be identified at $t = 1.84\,s$.

Further outboard, at the 90% of span location the three dimensional effects are quite significant, Figure B.4. The initial formation of a dynamic stall vortex and disturbances in the shear layer are discernible at $t = 0.72\,s$. The dynamic stall vortex quickly loses definition as a strong spanwise motion inboard predominates over the 30% of chord. The flow, however, remains highly arched over the front portion of the chord and there is some evidence of a shear layer vortex near the trailing edge. As the flow develops, this shear layer vortex becomes less distinct and is replaced by an increasingly strong vortex.

A different perspective of the flow development is shown in Figure B.5 where the wing is viewed from above and behind. At $t = 0.64\,s$ the dynamic stall vortex is visible as a disturbance in the smoke lines at approximately the quarter chord position.

It appears to be less well defined in the region of the tip vortex; at this stage the flow field is still predominantly two dimensional. The images recorded at $t = 0.96\,s$ *and* $t = 1.04\,s$ *are consistent and with those taken from the side which indicate that subsequent development of the dynamic stall vortex is dependent on spanwise location. In the mid-span region the vortex grows and convects two dimensionally until it reaches the mid chord. Further outboard, growth and convection are inhibited and, at the very tips the vortex appears to remain attached to the leading edge. Simultaneously, the smoke in the shear layer begins to coalesce until it forms a thick white band across the entire span close to the trailing edge. With reference to the side views presented earlier, this amalgamation of smoke most likely corresponds to the strengthening of the shear layer vortex. At* $t = 1.04\,s$ *this band of smoke becomes subtly distorted indicating that the shear layer is now interacting with the dynamic stall vortex whilst maintaining some connection with the tip vortex.*

The sequence of events that follow appear to involved complex vortical interactions in what can be described as a strongly three dimensional flow field. There is apparently no further chordwise convection of the dynamic stall vortex at this stage but, from the information presented in the side views, the section of the vortex at the mid-span is lifting away from the surface whilst continually drawing in the shear layer. The displacement of the shear layer can be seen in the frames corresponding to $t = 1.04\,s$ *and* $t = 1.36\,s$ *as the thick band of smoke becomes significantly altered near the mid-span. At* $t = 1.36\,s$ *the change in orientation of outboard sections of the dynamic stall vortex, to accommodate the lifting of the mid-span segment, becomes more apparent. The most significant changes occur at around 75% of span where the side view pictures indicate that the axis of rotation of the vortex becomes almost normal to the wing surface between* $t = 0.92\,s$ *and* $t = 1.28\,s$ *and at* $t = 1.36\,s$ *two counter rotating swirls appear clearly. By* $t = 1.52\,s$*, the swirls are noticeably stronger but still appear to retain connectivity with the leading edges of the wing tips through the*

furthest outboard sections of the dynamic stall vortex.

Further evidence of the behaviour and connectivity of the flow structures identified above is provided by Figure B.6. It is the flow field view taken from in front of the wing. In particular, the mid-span buckling of the dynamic stall vortex is clearly evident at $t = 1.04\,s$ *and* $t = 1.20\,s$. *Furthermore, these pictures suggest that the dynamic stall vortex is still a continuous flow structure, maintaining spanwise connectivity with the less well developed outboard sections. This is still the case as the central portion of the vortex continues to lift* ($t = 1.36\,s$) *forming an arch like structure with the counter rotating segments identified in other views. The area of the smoke in the centre below this arch is evidence of the shear layer being drawn into the dynamic stall vortex.*

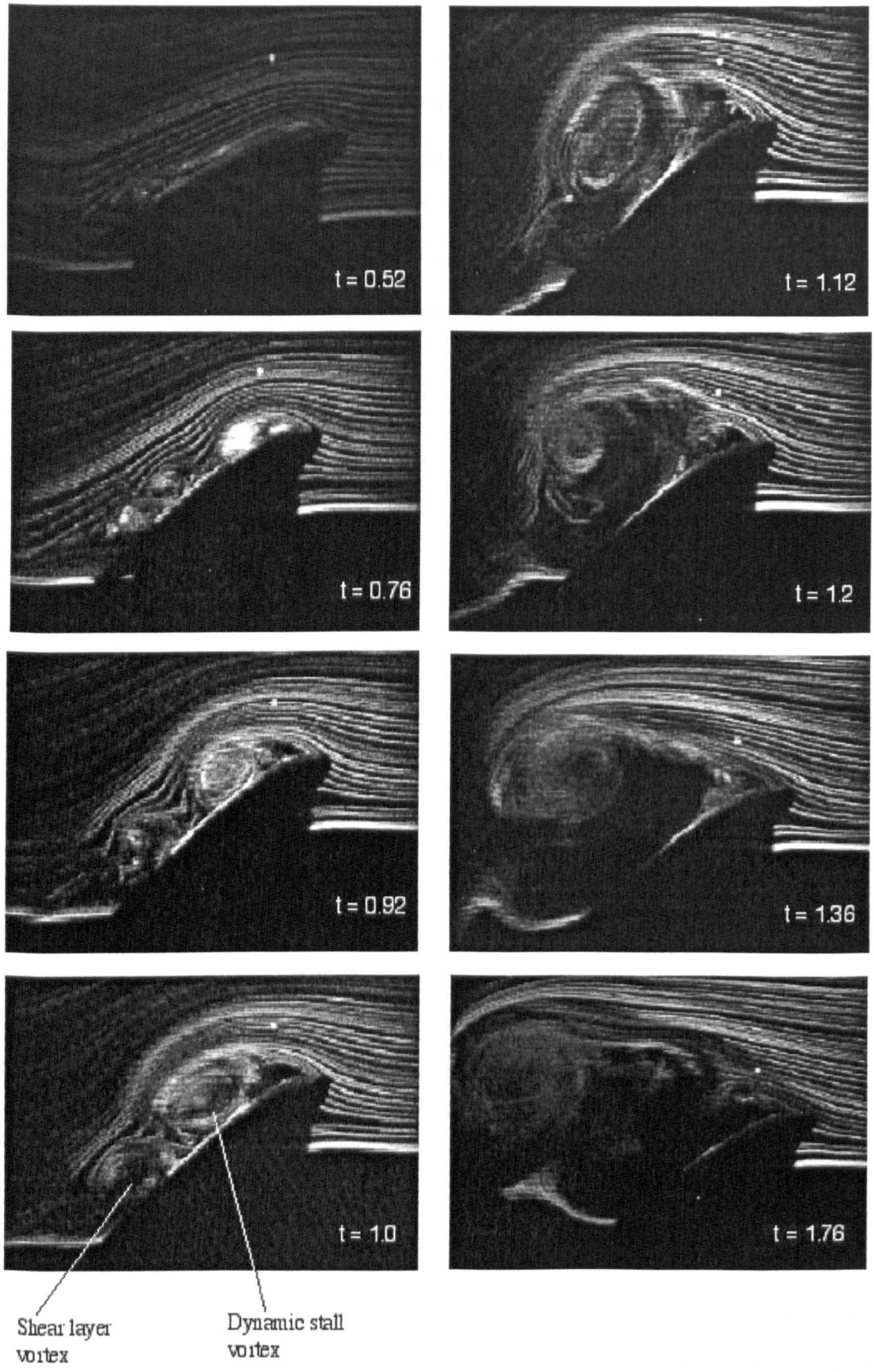

Figure B.2: Images of flow field at 57% of span of the rectangular wing for reduced pitch rate 0.08. (From Moir [100]).

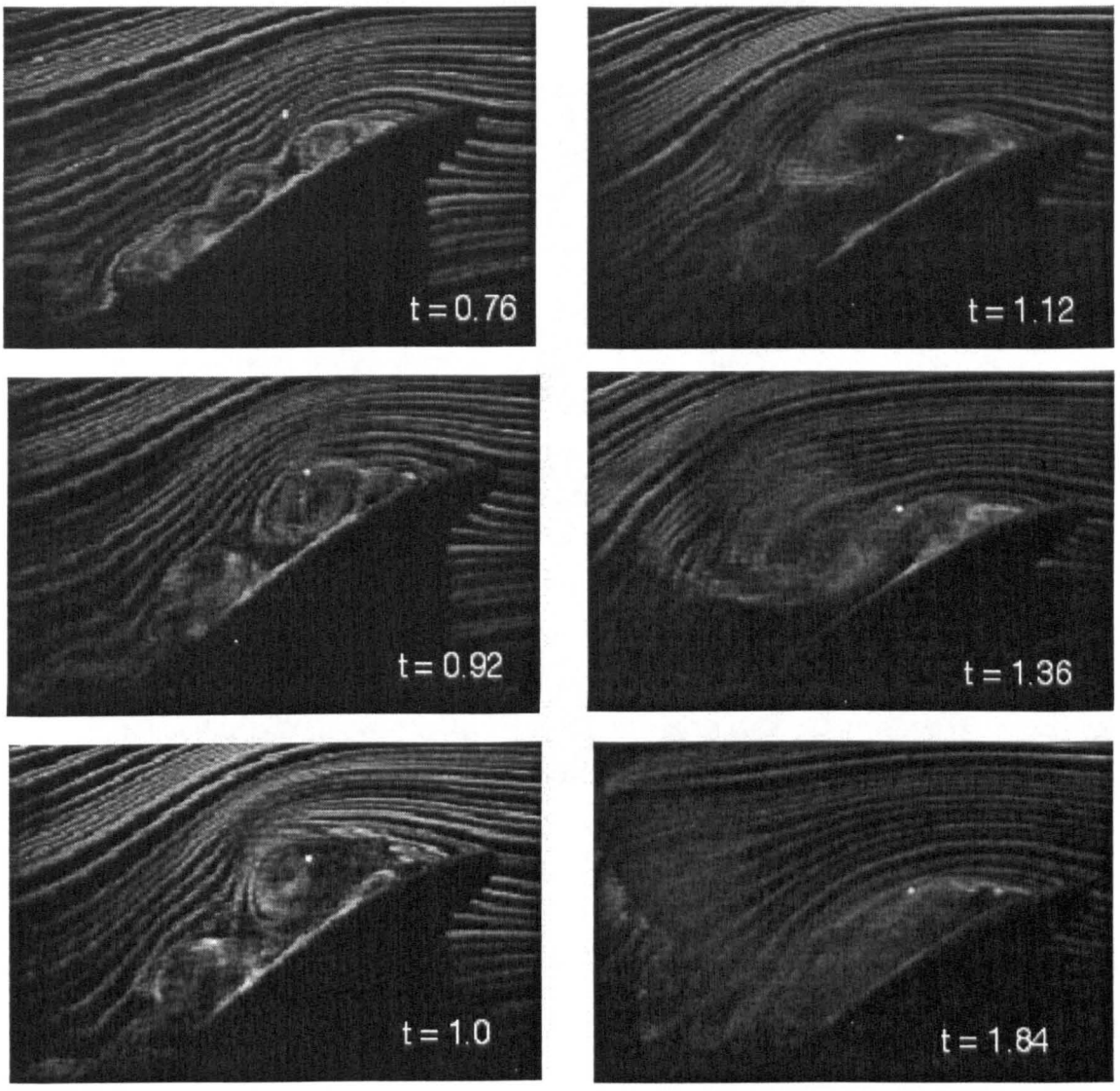

Figure B.3: Images of flow field at 75% of span of the rectangular wing for reduced pitch rate 0.08. (From Moir [100]).

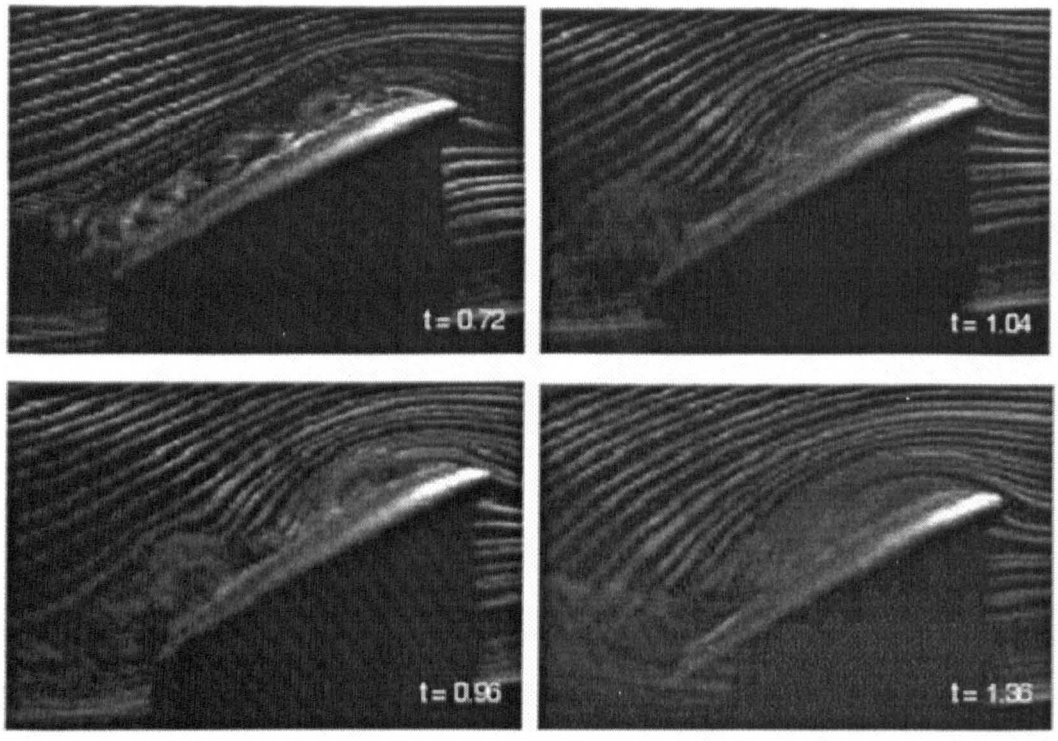

Figure B.4: Images of flow field at 90% of span of the rectangular wing for reduced pitch rate 0.08. (From Moir [100]).

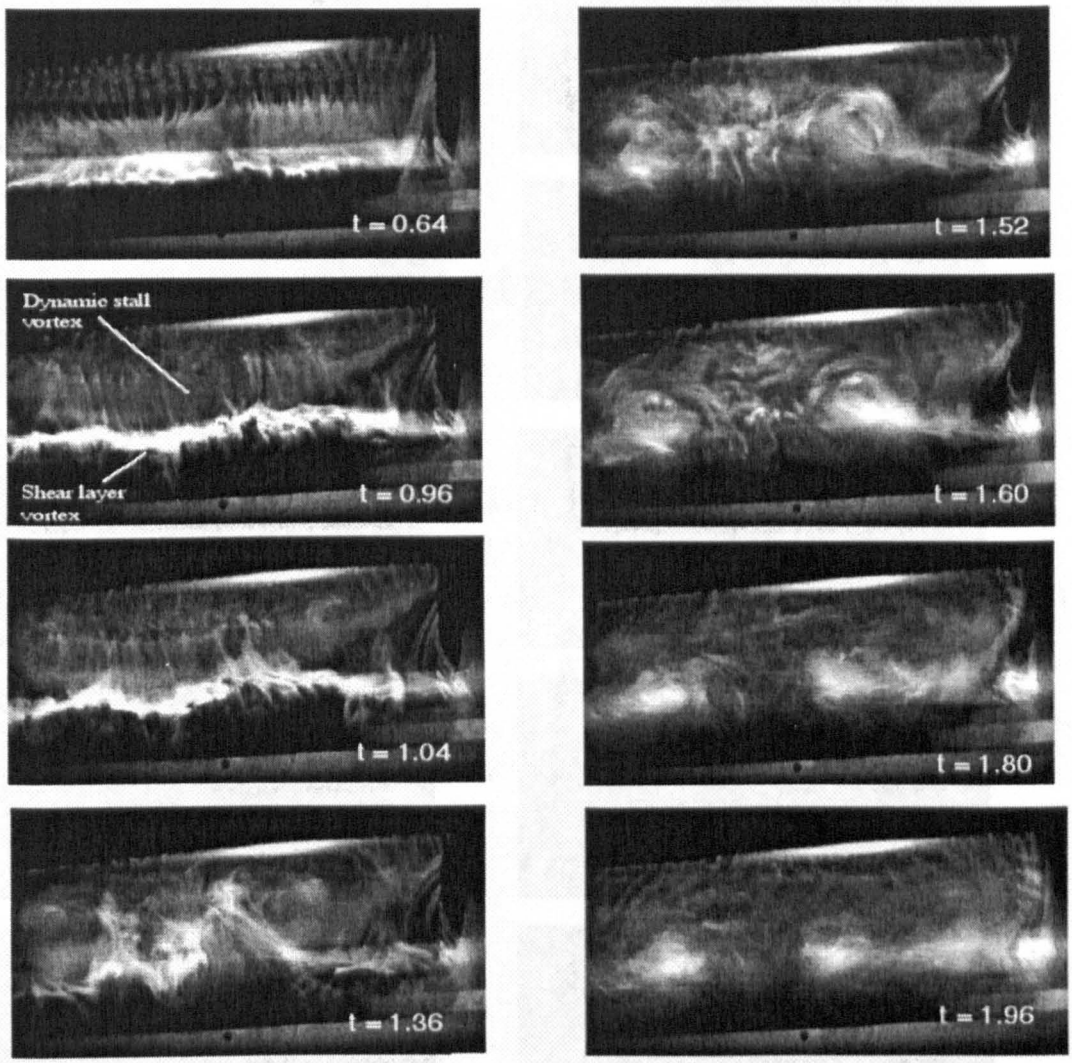

Figure B.5: Images of flow field on rectangular wing, view from above and behind for reduced pitch rate 0.08. (From Moir [100]).

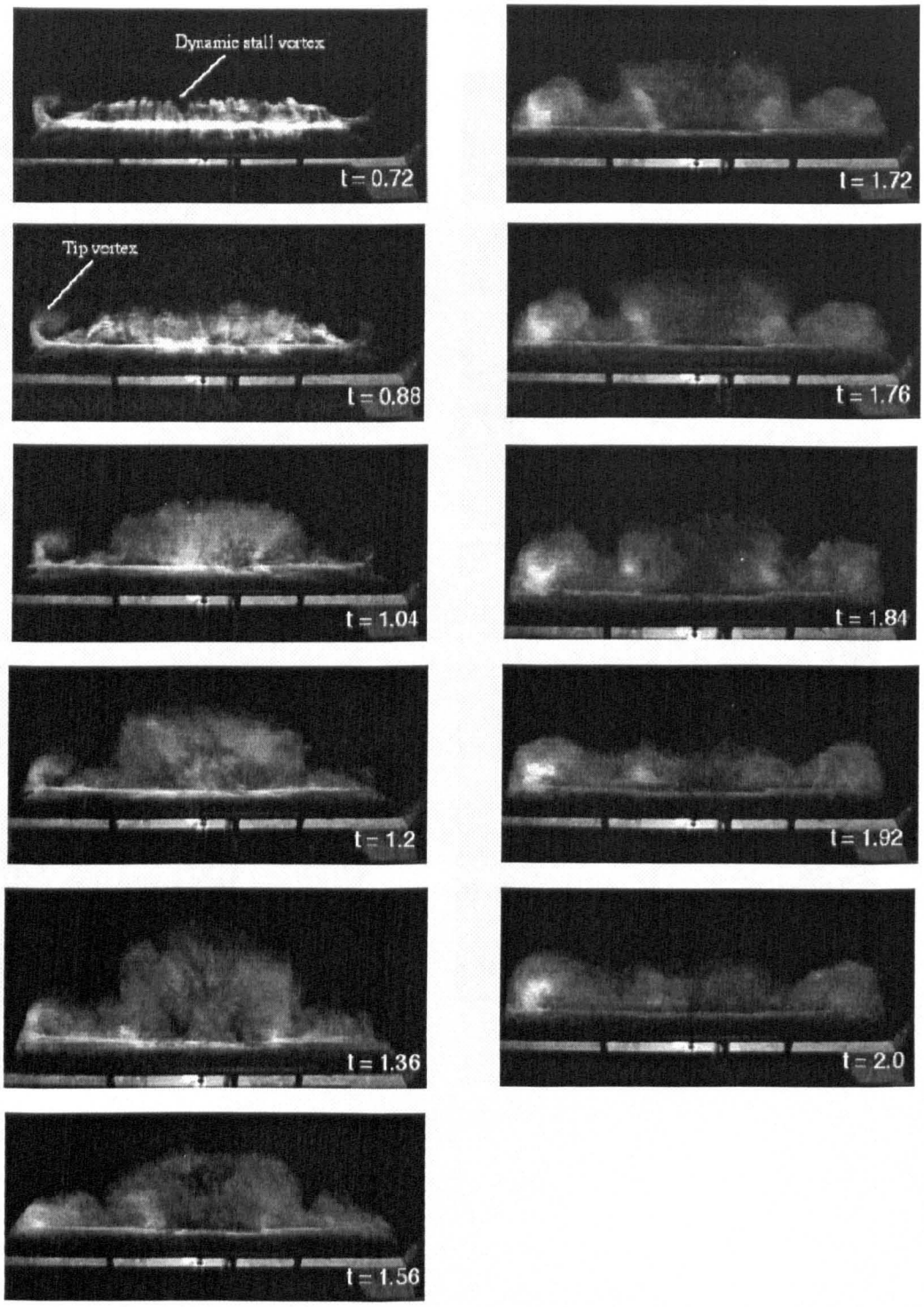

Figure B.6: Images of flow field on rectangular wing, view from upstream for reduced pitch rate 0.08. (From Moir [100]).

Appendix C

Equations of Motion

C.1 Navier-Stokes Equation

The flow field equations of motion were obtained by Navier (1823), Poisson (1831), Saint- Venant (1843) and Stokes (1845) and are usually known as the *Navier-Stokes equations.* The Navier-Stokes equations in rectangular coordinates are transcribed below.

$$\begin{aligned}
\frac{\partial v_x}{\partial t} + v_x\frac{\partial v_x}{\partial x} + v_y\frac{\partial v_x}{\partial y} + v_z\frac{\partial v_x}{\partial z} &= -\frac{1}{\rho}\frac{\partial p}{\partial x} + F_x + \nu\nabla^2 v_x \\
\frac{\partial v_y}{\partial t} + v_x\frac{\partial v_y}{\partial x} + v_y\frac{\partial v_y}{\partial y} + v_z\frac{\partial v_y}{\partial z} &= -\frac{1}{\rho}\frac{\partial p}{\partial y} + F_y + \nu\nabla^2 v_y \qquad \text{(C.1)} \\
\frac{\partial v_z}{\partial t} + v_x\frac{\partial v_z}{\partial x} + v_y\frac{\partial v_z}{\partial y} + v_z\frac{\partial v_z}{\partial z} &= -\frac{1}{\rho}\frac{\partial p}{\partial y} + F_z + \nu\nabla^2 v_z
\end{aligned}$$

where $\nu = \frac{\mu}{\rho}$ is the kinematic viscosity, $\boldsymbol{F}$ is the vector of the body forces (such as gravity) acting on the volume of the fluid particle. The explicit expression of $\nabla^2 v_x$ is

$$\nabla^2 v_x = div\ grad\ v_x = \frac{\partial^2 v_x}{\partial x^2} + \frac{\partial^2 v_x}{\partial y^2} + \frac{\partial^2 v_x}{\partial z^2}\ ,\ \text{etc.}$$

In vector form, equation (C.1) may be written as

$$\frac{\partial \boldsymbol{v}}{\partial t} + grad\left(\frac{1}{2}\boldsymbol{v}^2\right) - \boldsymbol{v} \times \boldsymbol{\omega} \;=\; -\frac{1}{\rho}\, grad\, p + \boldsymbol{F} + \nu\nabla^2\boldsymbol{v} \tag{C.2}$$

since $\nabla^2\boldsymbol{v} = grad(div\, \boldsymbol{v}) - curl\, curl\boldsymbol{v}$ and $div\boldsymbol{v} = 0$ whilst $curl\, \boldsymbol{v} = \boldsymbol{\omega}$, and the term $\nabla^2\boldsymbol{v}$ may be replaced by $curl\, \boldsymbol{\omega}$. In addition, the body forces may be considered negligible because the reaction of the fluid particle to a body force is remote. Moreover, it can be shown that gravitational body forces are always balanced by a vertical pressure gradient which does not interact with any flow. On this basis, equation (C.2) may be rewritten as:

$$\frac{\partial \boldsymbol{v}}{\partial t} - \boldsymbol{v} \times \boldsymbol{\omega} \;=\; -grad\left(\frac{p}{\rho} + \frac{1}{2}\boldsymbol{v}^2\right) - \nu curl\, \boldsymbol{\omega} \tag{C.3}$$

C.2 Vorticity Equation

The vorticity field is described by the vorticity equation which is derived by taking the curl of the Navier-Stokes equations (C.1):

$$\frac{D\boldsymbol{\omega}}{Dt} = \frac{\partial \boldsymbol{\omega}}{\partial t} + (\boldsymbol{v} \cdot \nabla)\boldsymbol{\omega} = (\boldsymbol{\omega} \cdot \nabla)\boldsymbol{v} + \nu\nabla^2\boldsymbol{\omega} = \boldsymbol{\omega} \cdot \mathcal{T} + \nu\nabla^2\boldsymbol{\omega} \tag{C.4}$$

where $\mathcal{T}$ is the strain rate tensor, and $\frac{D}{Dt}$ is the Lagrangian derivative that indicates the rate of change of particle vorticity. The vorticity field evolves under three dynamical actions, convection $(\boldsymbol{v} \cdot \nabla)\boldsymbol{\omega}$, stretching and/or turning of a vortex-line $\boldsymbol{\omega} \cdot \mathcal{T}$ and viscous dissipation $\nu\nabla^2\boldsymbol{\omega}$. One of the most important things about the vorticity equation is that pressure and gravity forces do not play a direct role in the vorticity equation and so will not directly change the vorticity. The physical reason has to do with the fact that vorticity is an indicator of solid-body rotation. Pressure forces and gravity forces act through the center of mass of a particle and

cannot produce a rotation. On the other hand, shear stresses act tangentially at the surface of a particle and, if they are unbalanced, will generate vorticity.

Appendix D

Flow Visualization Set Images, 60^0 Swept-Tip Wing

The following images are taken from the internal Glasgow report [100] whos authors are Moir and Coton. They are relative to the flow visualization test on a rectangular wing with 60^0 swept-tip. The model was pitched around its quarter chord from 0^0 to 40^0, Figure D.1, in laminar flow conditions at a chord Reynolds number of approximately 13,000.

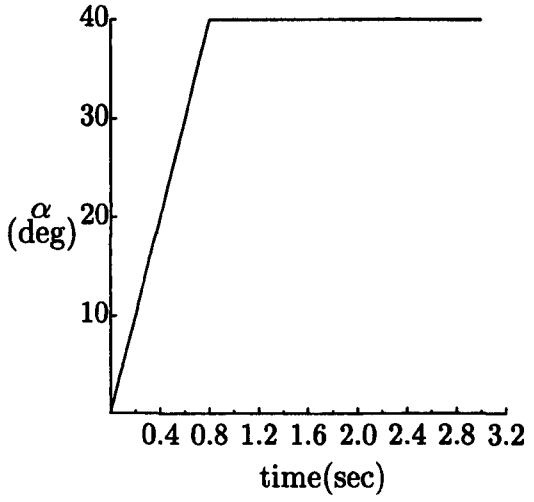

Figure D.1: Pitch incidence variation versus time for reduced pitch rate 0.08.

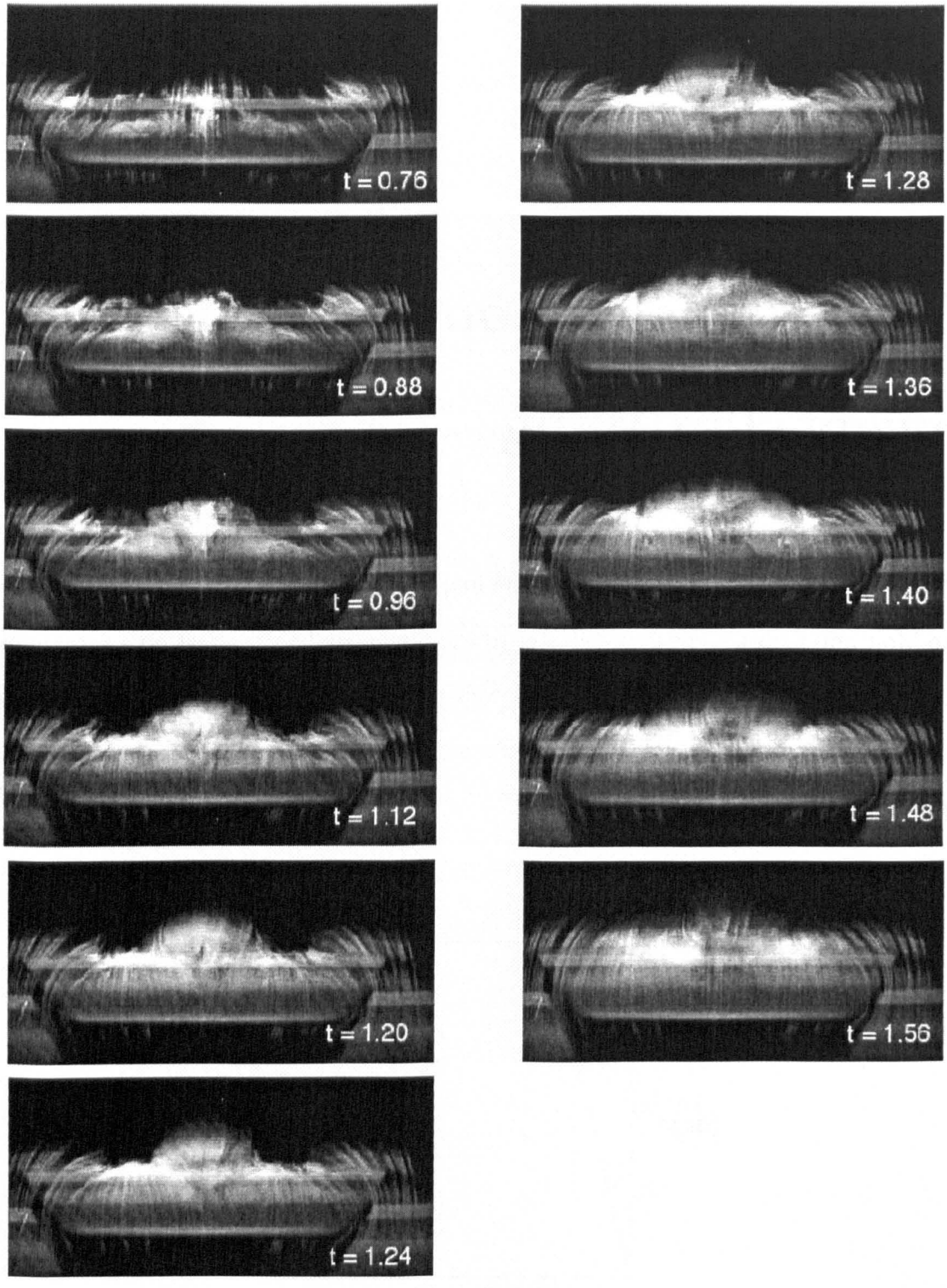

Figure D.2: Images of flow field on 60^0 swept-tip wing for reduced pitch rate 0.08; view from upstream. (From Moir [100]).

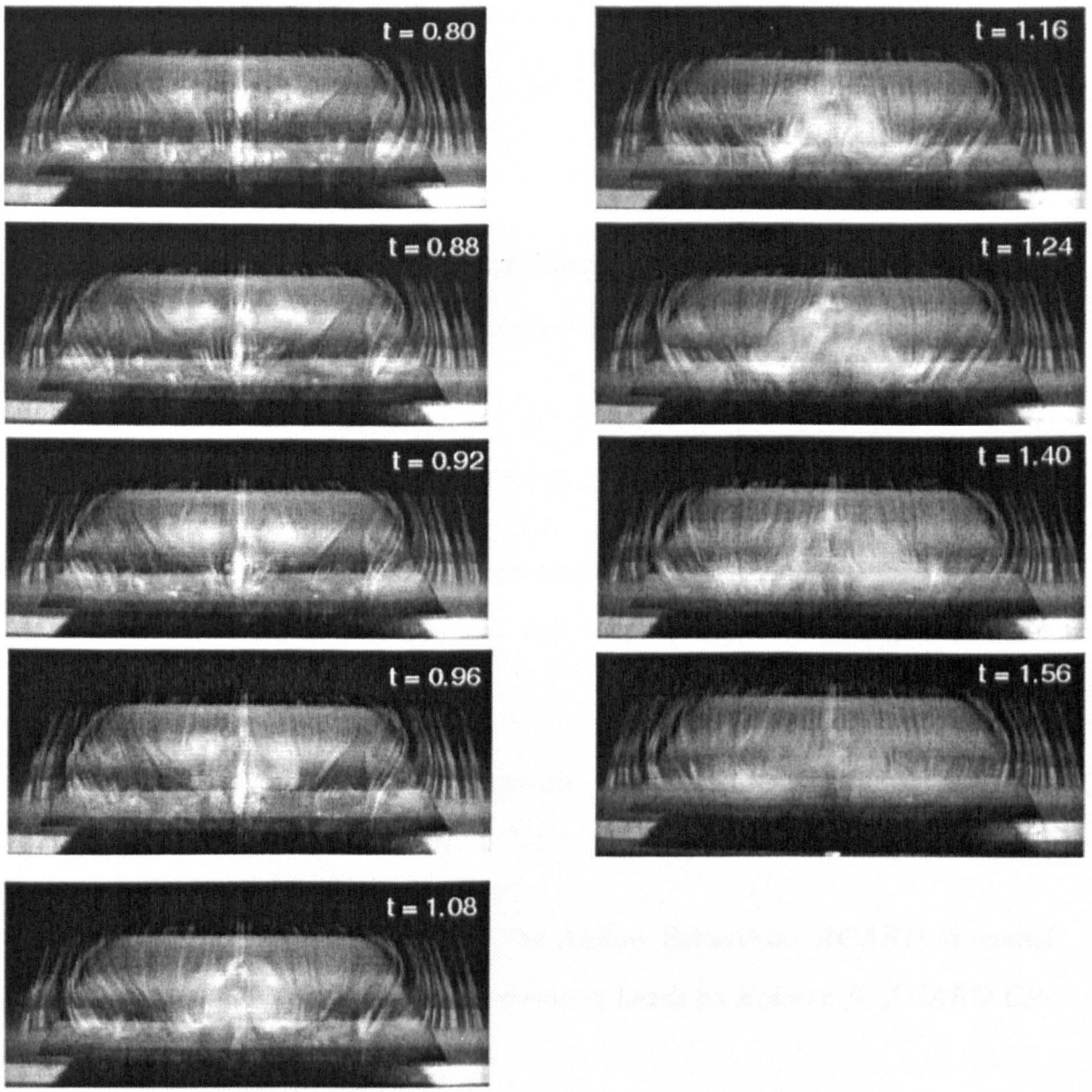

Figure D.3: Images of flow field on 60^0 swept-tip wing and reduced pitch rate 0.08; view from above and behind. (From Moir [100]).

Bibliography

[1] Adler J. and Luttges M. Three Dimensionality in Unsteady Flow about a Wing. *AIAA Paper 85-0132*, January 1985.

[2] Anderson D. A., Tannehill J. C. and Pletcher R. H. *Computational Fluid Mechanics and Heat Transfer.* McGraw-Hill, New York, 1984.

[3] Ashworth J. and Luttes M. Comparison in Three Dimensionality in the Unsteady Flows Elicited by Straight and Swept Wings. *AIAA Paper 86-2280*, August 1986.

[4] Beddoes T. S. A Synthesis of Unsteady Aerodynamic Effects Including Stall Hysteresis. *Vertica, Vol. 1, pp. 113-123*, 1976.

[5] Beddoes T. S. Representation of the Airflow Behaviour. *AGARD Specialist Meeting on the Prediction of Aerodynamic Loads on Rotorcraft, AGARD CP-334*, 1982.

[6] Beddoes T. S. A Near-Wake Dynamic Model. *Proceedings of the AHS National Specialists Meeting on Aerodynamic and Acoustics*, February 1987.

[7] Beddoes T. S. Onset of Leading Edge Separation Effects under Dynamic Conditions and Low Mach Number. *Paper presented at American Helicopter Society 34th. Annual Forum, Washington*, May 1978.

[8] Beddoes T. S. Two and Three Dimensional Indicial Methods for Rotor Dynamic Airloads. *American Helicopter Society National Specialists Meeting, Arlington, Texas*, November 1989.

[9] Carr L. W. An Assessment of the Impact of Compressibility on Dynamic Stall. *AIAA Paper 95-0779*, January 1995.

[10] Carr L. W., McAlister K. W. and McCroskey W. J. Analysis of the Development of Dynamic Stall Based on Oscillating Airfoil Experiment. *NASA TN D-8382*, January 1977.

[11] Carta F. O. Analysis of Oscillatory pressure Data Including Dynamic Stall Effects. *NASA CR-2394*, 1974.

[12] Carta F. O. A Comparison of the Pitching and Plunging Response of an Oscillating Airfoil. *NASA CR-3172*, 1979.

[13] Carta F. O. Experimental Investigation of the Unsteady Aerodynamic Characteristics of an NACA 0012 Aerofoil. *United Aircraft Research Laboratories Report M-1281-1*, August 1960.

[14] Chandrasekhara M. and Carr L. W. Flow visualization studies of the Mach number effects on the dynamic stall of an aerofoil. *AIAA Paper 89-0023*, 1989.

[15] Chung J. and Parikh P. A Computational Study of the Abrupt Wing Stall (AWS) Characteristics for Various Fighter Jets: Part II, AV8B and F/A-18C. *AIAA Paper 2003-747*, 2003.

[16] Costes J. Unsteady Three-Dimensional Stall on a Rectangular Wing. *Twelfth European Rotorcraft Forum, Garmisc-Partenkirchen, Germany*, September 22-25, 1986.

[17] Coton F. N., Galbraith R. A. McD, Jiang D. and Gilmour R. Preliminary Results from a Three Dimensional Stall Experiment on a Finite Wing. *Presented at 21st European Rotorcraft Forum, St. Petersburg Russia, Paper II-3*, 1995.

[18] Coton F. N., Galbraith R. A. McD, Jiang D., Gilmour R. The comparison between the dynamic stall of a finite wing with straight and swept tips. *Presented at International Congress of the Aerospace and Sciences, Sorrento, Italy*, 1996.

[19] Cowely S. J., Van Dommelen L. L. and Lam S. T. On the Use of Lagrangian Variables in Descriptions of Unsteady Boundary-Layer Separation. *Phil. Trans. R. Soc. London Ser. A333, pp 343-378*, 1991.

[20] Ekaterinaris J.A. Application of High-Order Accurate Implicit Method to Rotor Aerodynamics. *Nielsen Engineering and Research, Mountain View, CA, NEAR TR 556*, June 2000.

[21] Ekaterinaris J.A. and Platzer M.F. Computational Prediction of Dynamic Stall. *Progress of Aerospace Sciences, Vol. 33, No 11-12, pp.759-846*, 1998.

[22] Elliot J. W., Cowley S. J. and Smith F. T. Breakdown of Boundary Layers: (i) on Moving Surface, (ii) in Self-Similar Unsteady Flows, (iii) in Fully Unsteady Flow. *Geophys. Astrophys. Fluid Dyn. 25, pp. 77-138*, 1983.

[23] Ericsson L. E. and Reding J. P. Fluid Mechanics of Dynamic Stall. Part I. unsteady flow concepts. *Journal of Fluids and Structures*, 2:1–33, 1988.

[24] Ericsson L. E. and Reding J. P. Fluid Mechanics of Dynamic Stall. Part I. unsteady flow concepts, Vol. 2, pp. 1-33. *Journal of Fluids and Structures*, 1988.

[25] Escudier M. P., Burnstein J. and Maxworthy T. The Dynamics of Concentrated Vortices. *Proc. Roy, Soc, A382, 335-360*, 1982.

[26] Evans W. T. and Mort K. W. Analysis of Computed Flow Separation Parameters for a Set of Sudden Stalls in Low Speed Two-Dimensional Flow. *NASA TND-85*, 1959.

[27] Faler J. H. and Leibovich S. Disrupted States of Vortex Flow and Vortex Breakdown. *Phys. Fluids, 20, 1385 - 1400*, 1977.

[28] Ferrecchia A., Coton F. N., Galbraith R. A. McD. An Examination of Dynamic Stall Vortex Inception on a Finite Wing and on a NACA 0015 Aerofoil. *AIAA Paper 99-3112*, 1999.

[29] Feszty D. and Vezza M. Alleviation of Rotor Blade Dynamic Stall Via Trailing Edge Flap Flow Control. *AIAA Paper 2003-0050*, 2003.

[30] Fletcher C. A. J. *Computational Techniques for Fluid Dynamics.* Springer, Berlin, 1991.

[31] Freymuth P. Visualizing the Connectivity of the Vortex System for Pitching Wings. *Journal of Fluids Engineering, Vol.111, pp. 217-220*, June, 1989.

[32] Freymuth P., Finaish F. and Bank W. Three Dimensional Vortex Systems of Finite Wings. *Journal of Aircraft, Vol. 25, No. 10, pp.971-972*, 1988.

[33] Fulushima T. and Dadone L. U. Comparison of Dynamic Stall Phenomena for Pitching and Vertical Translation Motions. *NASA CR-2793*, December, 1976.

[34] Fung, K. Y and Carr L. W. Effects of Compressibility on Dynamic Stall. *AIAA Journal*, 1991.

[35] Gad-el-Hak M. and Ho C. M. Three Dimensional Effects on a Pitching Lift Surface Elicited by Straight and Swept Wings. *AIAA Paper 85-0041*, January 1985.

[36] Galbraith R. A. McD. A Data Acquisition System for the Investigation of Dynamic Stall. *Proceedings of the 2nd International Conference on Computational Methods and Experimental Measurements*, 1984.

[37] Galbraith R. A. McD and Leishman, J. G. A Micro-Computer Based Test Facility for the Investigation of the Dynamic Stall. *International Conference on the 'Use of Micros in Fluid Engineering, Paper E3'*, June 1983.

[38] Galbraith R. A. McD, Gracey M. W. and Leitch E. Summary of Pressure Data for Thirteen Aerofoils on the University of Glasgow's Database. *G.U. Aero Report: 9221, University of Glasgow*, 1992.

[39] Galbraith R. A. McD, Jiang D., Green R. B., Gracey M. W. and Gilmour R. Collected Data for Tests on a NACA 0015 Aerofoil with Chord length 0.275m. *G.U. Aero Report: 9209, University of Glasgow*, 1992.

[40] Galbraith R. A. McD, Niven A. J. and Seto L. Y. On the Duration of Low Speed Dynamic Stall. *Proceedings of the 15th ICAS Conference*, 1986.

[41] Gangwani S. T. Prediction of Dynamic Stall and Unsteady Airloads for Rotors Blades. *Journal American Helicopter Society, pp.57-64*, 1982.

[42] Gault D. E. Boundary Layer and Stalling Characteristics of the NACA 64−009 Airfoil Section. *NACA TN 1894*, 1949.

[43] Ghia K. N., Yang J., Osswald G. A. and Ghia U. Physiscs of Forced Unsteady Flow for a NACA 0015 Airfoil Undergoing Constant-Rate Pitch-Up Motion. *Fluid. Dyn. Res. Journal*, 1992.

[44] Ghia K. N., Yang J., Osswald G. A. and Ghia U. Study of the Role of Unsteady Separation in the Formation of Dynamic Stall Vortex. *AIAA paper 92-0196*, 1992.

[45] Gracey M. W., Niven A. J. and Galbraith R. A. McD. A Consideration of Low-Speed Dynamic Stall Onset. *Fifteenth European rotorcraft Forum, Paper No. 11.*, September, 1989.

[46] Gracey M. W., Niven A. J., Coton F. N., Galbraith R. A. McD and Jiang G. A Correlation Indicating Incipient Dynamic Stall. *Journal of the Royal Aeronautical Society*, August/September 1996.

[47] Green R. B. and Galbraith R. A. McD. Dynamic Recovery to Fully Attached Aerofoil Flow from Deep Stall. *AIAA Journal*, 1992.

[48] Green R. B. and Galbraith R. A. McD. Phenomena observed During Aerofoil Ramp-Down Motions from the Fully Separated State. *Aeronautical Journal Vol.98, No. 979, pp. 349-356* , 1994.

[49] Green R. B. and Galbraith R. A. McD. Dynamic Stall Vortex Convection: Thoughts on Compressibility Effects. *The Aeronautical Journal of the Royal Society*, 1996.

[50] Green R. B., Galbraith R. A. McD and Niven A. J. Measurements of the Dynamic Stall Vortex Convection Speed. *7th European Rotorcraft Forum, Paper 1864*, 1992.

[51] Ham N. D. and Garelick M. S. Dynamic Stall Considerations in Helicopter Rotors. *Journal of the American Helicopter Society, Vol. 13, No. 2, pp. 49-55*, April 1968.

[52] Ham N. D. and Young M. I. Torsional Oscillation of Helicopter Blades due to Stall. *AIAA Journal of Aircraft, Vol. 3, No. 3, pp. 219-224*, May-June 1966.

[53] Hirsch C. *Numerical Computation of Internal and External Flows. Vol.1 Vol. II.* Wiley, New York, 1991.

[54] Honkan A. and Andreopoulos J. Investigation Three-Dimensional Vorticity Measurements in Vortical Flow over a Delta Wing. *AIAA Journal*, 1997.

[55] Hopfinger E. J., Browand F. K. and Gagne Y. Turbulence and Waves in a Rotating Tank. *J. Fluid Mech., 125, 505 - 534*, 1982.

[56] Isogai K. An Experimental Study of the Unsteady Behavior of a Short Bubble of an Airfoil During Dynamic Stall with Special Reference to the Mechanism of the Stall Overshoot Effect. *MIT Aeroelastic and Structures Research Laboratory, ASRL TR 130-2*, June 1970.

[57] Jacobs E. N. The Aerodynamic Characteristics of Eight very Thick Airfoils from Tests in the Variable Density Wind Tunnel. *NACA Rep. 391*, 1931.

[58] Jacobs E. N. and Sherman A. Aerofoil Section Characteristics as Affected by Variations of the Reynolds Number. *NACA Rep. 586*, 1937.

[59] Jenson V. J. Viscous Flow Round a Sphere at Low Reynolds Number (< 40). *Proc. Roy. Sco. Lond. Ser.A249, pp. 346-361*, 1959.

[60] Jiang D., Coton F. N., Galbraith R. A. McD and Gilmour R. Collected Data for Tests on a NACA 0015 Section Rectangular Wing (Aspect Ratio 3). *G.U. Aero Report: 9515, Vol1, University of Glasgow*, 1995.

[61] Jiang D., Coton F. N., Galbraith R. A. McD and Gilmour R. Collected Data for Tests on a NACA 0015 Section Rectangular Wing (Aspect Ratio 3). *G.U. Aero Report: 9515, Vol2, University of Glasgow*, 1995.

[62] Jiang D., Coton F. N., Galbraith R. A. McD and Gilmour R. Collected Data for Tests on a NACA 0015 Section Rectangular Wing with 60^0 Swept Tips. *G.U. Aero Report: 9527, University of Glasgow*, 1995.

[63] Johnson W. Comparison of Three Methods for Calculation of Helicopter Rotor Blade Loading and Stresses Due to Stall. *NASA-TN D-7833*, November,1974.

[64] Jumper E. J., Shredk S. J. and Dimmick R. L. Lift Curve Characteristics for an Aerofoil Pitching at Constant Rate. *AIAA-86-0117*, 1986.

[65] Knight D. R. and Ghosh C. P. Two-Dimensional Unsteady Leading Edge Separation on a Pitching Airfoil. *AIAA Paper 93-2977*, 1993.

[66] Laghezza M. Studio in Galleria del Vento ai Fumi degli Effetti di Tridimensionalitá sullo Stato Dinamico. (Smoke Tunnel Investigation of Three-Dimensional Dynamic Stall.). *Tesi di Laurea, Politecnico di Torino, Facoltá di Ingegneria Aeronautica*, December 1994.

[67] Laneville A. and Vittecoq P. Effect of Turbulence on Dynamic Stall. *Paper presented at the wind turbine aerodynamics seminar, Sandia National Laboratories, Albuquerque, NM*, March 1985.

[68] Lee G., Buell D. A. and Licursi J. P. Laser Holography Interferometry for an Unsteady Airfoil Undergoing Dynamic Stall. *AIAA Journal, Vol. 22, pp. 504-511*, April 1984.

[69] Leibovich S. *Vortex Stability and Breakdown.* ed. A. D. Young, AGARD CP 342, 23.1-23.22, 1983.

[70] Leibovich S. Vortex Stability and Breakdown: Survey and extension. *AIAA J., 1192 - 1206*, 1984.

[71] Leishman, J. G. A Two-Dimensional Model for Airfoil Unsteady Drag below Stall. *AIAA Journal Aircraft, Vol. 25, No. 7, pp. 665-666*, July 1988.

[72] Leishman, J. G. *Contributions to the Experimental Investigations and Analysis of Aerofoil Dynamic Stall.* Ph.D. Dissertation, University of Glasgow, United Kingdom, March 1984.

[73] Leishman, J. G. Indicial Lift Approximation for Two-Dimensional Subsonic Flow Obtained from Oscillatory Measurements. *Journal Aircraft, Vol. 30, No. 3, pp.340-351*, May-June 1993.

[74] Leishman, J. G. and Beddoes T. S. A Semi-Empirical Model for dynamic Stall. *Journal American Helicopter Society, Vol. 34, No. 3, pp. 3-17*, July 1989.

[75] Leishman, J. G. and Nguyen, K. Q. State-Space Representation of Unsteady Airfoil Behaviour. *AIAA Journal, Vol. 28, No. 5, pp. 836-844*, May 1990.

[76] Lighthill M. J. *Laminar Boundary Layers. Chapter II, pp. 46-95.* L. Rosenhead, 1963.

[77] Liiva J. Unsteady Aerodynamics and Stall Effects on Helicopter Rotor Blade Sections. *Journal Aircraft, Vol. 6, No 1, pp.46-51.*, 1969.

[78] Liiva J., Davenport F. J. and Gray L. Wind Tunnels Tests of Thin Airfoils Oscillating near Stall, Vol. I, summary and evaluation of results. *USAAVLABS TR 68-89A, U. S. Army Aviation Material Laboratories, Fort Eustis, Virginia.*, January 1969.

[79] Liiva J., Davenport F. J., Gray L. and Walton I. C. Two Dimensional Tests of Airfoils Oscillating near Stall, Vol. I, summary and evaluation of results. *USAAVLABS TR 68-13A, U. S. Army Aviation Material Laboratories, Fort Eustis, Virginia. AD 670957*, April 1968.

[80] Loftin Laurence K. and Bursnall William J. The Effect of Variations in Reynolds Number Between $3 * 10^6$ and $25 * 10^6$ upon the Aerodynamic Char-

acteristics of a Number of NACA 6-Series Airfoil Sections. *NACA TN 1773*, September 1948.

[81] Lorber P. F. Tip Vortex, Stall Vortex and Separation Observations on Pitching Three Dimensional Wings. *AIAA Paper 93-2972*, July 1993.

[82] Lorber P. F. and Carta F. O. Unsteady Stall Penetration Experiments at High Reynolds Number. *UTRC R87-956939-3*, 1987.

[83] Lorber P. F. and Covert E. E. Unsteady Airfoil Boundary Layers Experiment and Computation. *Third Symposium on 'Numerical and Physical Aspects of Aerodynamic Flow', Long Beach, CA*, January, 1985.

[84] Lyman F. A. Vorticity Production at Solid Boundary. *Appl. Mech. Rev. 46, 157*, 1990.

[85] Maresca C., Favier D. and Rebont J. Unsteady Aerodynamics of an Airfoil at High Angle of Incidence Performing Various Linear Oscillations in a Uniform Stream. *Paper no. 12, Fifth European rotorcraft and powered Lift aircraft forum, Amsterdam, Netherlands*, 1979.

[86] Maxworthy T., Hopfinger E. J. and Redekopp L. G. Wave motions on vortex cores. *J. Fluid Mech., 151, 141 - 165*, 1985.

[87] Maxworthy T., Mory M. and Hopfinger E. J. *Waves on Vortex Cores and their Relation to Vortex Breakdown*. ed. A. D. Young, AGARD CP 342, 29.1-29.13, 1983.

[88] McCroskey W. J. The Phenomenon of Dynamic Stall. *NASA TM-81264*, 1981.

[89] McCroskey W. J. Unsteady Airfoils. *Ann. Rev. Fluid Mech., vol 14, pp. 285-311*, March, 1982.

[90] McCroskey, W. J. and Pucci, S. L. Viscous-Inviscid Interaction on Oscillating Airfoils in Subsonic Flow. *AIAA J. 20, 167*, 1980.

[91] McCroskey W. J., McAlister K. W. and Carr L. W. Dynamic Stall Experiments on Oscillating Airfoils. *AIAA Journal, Vol. 14, No. 1, pp. 57-63*, January, 1976.

[92] McCroskey W. J., McAlister K. W., Carr L. W. and Pucci S. L. Dynamic Stall on Advanced Airfoil Sections. *American Helicopter Society, Preprint 80-01*, May, 1980.

[93] McCullough G. B. and Gault D. E. An Experimental Investigation of the NACA $63_1 - 012$ Airfoil Section with Leading Edge Suction Slots. *NACA TN 1683*, 1948.

[94] McCullough G. B. and Gault D. E. Boundary Layer and Stalling Characteristics of the NACA 64A006 Airfoil Section. *NACA TN 1849*, 1949.

[95] McCullough G. B. and Gault D. E. An Experimental Investigation of the NACA $63_1 - 012$ Airfoil Section with Leading Edge and Midchord Suction Slots. *NACA TN 2041*, 1950.

[96] McCullough G. B. and Gault D. E. Examples of Three Representative Types of Aerofoil-Section Stall at Low Speed. *NACA TN 2502*, 1951.

[97] Melvill J. B. An Experimental Study of the Stalling of Wings. *British A.R.C., R. and M. No. 1588*, 1933.

[98] Melvill J. B. Stalling. *Journal Royal Aero. Soc., Vol. 38, No. 285, pp. 753-770 (2nd Wilbur Wright Memorial Lecture.)*, September 1934.

[99] Millikan C. B. and Klein A. L. The effect of turbulence. *Aircraft Engineering, Vol.5, No. 8, pp. 169-174*, August 1933.